Multi-dimensional Numerical Study of Molten Corium-Concrete Interaction (MCCI) Mechanism by MPS Method

MPS法による溶融コリウム-コンクリート相互作用（MCCI）メカニズムの多次元数値解析研究

July 2016

Xin LI

李 昕

Multi-dimensional Numerical Study of Molten Corium-Concrete Interaction (MCCI) Mechanism by MPS Method

MPS法による溶融コリウム-コンクリート相互作用（MCCI）メカニズムの多次元数値解析研究

July 2016

Waseda University Graduate School of Advanced Science and Engineering

and Tokyo City University Graduate School of Engineering,

Cooperative Major in Nuclear Energy, Research on Reactor Theory

Xin LI

李 昕

Abstract

This thesis presents a multi-dimensional numerical study on Molten Corium-Concrete Interaction (MCCI) with Moving Particle Semi-implicit (MPS) method and additional originally developed models. The thesis includes validation of the developed MPS method against one-dimensional (1-D), two-dimensional (2-D) and three-dimensional (3-D) MCCI experiments. The complex interactions of influential factors of MCCI have been understood through mechanistic modeling. Discussions on discrepancies of calculated results with experimental results with respect to fundamental physical phenomena have been developed comprehensively for the first time in the history of MCCI research. The developed MPS simulations have shown the mechanism that distinguishes isotropic ablation of limestone concrete and anisotropic ablation of siliceous concrete by oxidic corium.

Chapter 1 states the background, necessity, and objectives of current study. In a hypothetical nuclear reactor severe accident, late containment failure could be caused by long-term melt-through of concrete basemat by core melt or corium discharged from the failed reactor pressure vessel. This scenario is called MCCI. The consequences can be catastrophic since the containment integrity can be threatened and lead to fission products release. Thus, deep understanding of the progression of MCCI is essential to enhance safety and reliability of nuclear power.

Several MCCI experiments have been carried out since 1980s. The early large scale experiments are mostly 1-D MCCI experiments, aiming at studying 1-D ablation behavior of various concrete by oxides or metal, the effect of Zr oxidation, the effect of an overlying water pool, and the aerosol release from the melt. More recent experiments focused more on the 2-D concrete ablation pattern regarding the axial versus lateral ablation ratio and melt coolability of late water injection. In a series of 2-D tests, one of the major findings was that in the tests with siliceous concrete, an anisotropic pattern (lateral ablation more significant than axial ablation) has been observed, while in the

tests with limestone concrete, a more isotropic ablation pattern has been observed. However, the mechanism of the isotropic/anisotropic pattern has not yet been well understood.

Several computer codes have been developed, aiming at modeling the physical and chemical phenomena during MCCI and validated against numerous MCCI tests. The difficulty in understanding and predicting MCCI with these past computer codes arises from not only the difficulty in accurate modeling of thermal-hydraulics (heat transfer and convection) and phase change which governs MCCI, but also the difficulty in accurately modeling complex interactions of various influential factors (e.g., chemical reaction heat, formation of slag-film at boundaries, crust formation, dissolution and remelting, relocation of thermally stable aggregates, etc). As the results, the past studies had the following issues:

- Difficulties in understanding discrepancies among simulations or among simulation and experimental results in terms of physical phenomena.
- Good agreement of calculation results with experimental results does not necessarily assure appropriate modeling, because of adjustments of various parameters in the empirical correlations.

Moreover, in these codes, only 1-D or simplified 2-D geometry with average axial and radial ablation depths can be evaluated. Different choices of empirical correlations such as heat transfer correlations at concrete/melt pool side/ bottom have led to discrepancies among predictions of axial/lateral ablation depths among these codes validated against MCCI experiments. These discrepancies indicate the limitations of specific correlations and simplified models based on current knowledge of MCCI, which suggest a necessity to understand MCCI mechanistically and to develop a less empirical correlation dependent method capable of more accurate and multi-dimensional predictions to further improve the reliability of numerical analysis of MCCI.

Considering the importance and necessity mentioned above, a multi-dimensional

MCCI code (2-D and 3-D) has been developed based on MPS method. MPS method is a particle method for analyzing incompressible media. As a Lagrangian method, MPS method discretizes the computation domain with particles instead of meshes or grids. The governing equations are also discretized by weight function and particle interaction models. As a result, the advantages of MPS are that it can easily and accurately capture free surface, interface and fluid thermophysical properties, which provide superiority to other methods when simulating important phenomena involving dynamic evolution of solid-liquid boundary such as crust formation/remelting observed in MCCI. Moreover, different geometries of 2-D or 3-D can be established accurately, which facilitate more accurate simulation of ablation profile of MCCI. The above featured advantages of MPS method have been validated against phenomena such as fluid splashing and melt stratification and solidification/melting. There have also been successful validations of MPS method against MCCI tests by other researchers previously. However, the validations were either on only 1-D test or a very small scale MCCI tests with simulant materials. MPS method has never been validated against multi-dimensional MCCI experiments in a comprehensive manner to investigate the mechanism of important phenomenology in MCCI. Hence, this study aims to reveal MCCI mechanism from a more mechanistic and fundamental perspective by multi-dimensional MPS method.

Chapter 2 describes the fundamentals and improvements of MPS method. The additional and originally developed models that are incorporated into MPS code "MPS-SW-MAIN-Ver.2.0" are presented, which include chemical reaction heat, corium viscosity, slag film, crust dissolution models, heat conduction and phase change model. These models have been specially developed for MCCI simulations, especially the former four original ones. Chemical reaction heat model is to consider the chemical heat introduced in melt pool by metal oxidation. Corium viscosity model is to consider temperature dependence of corium viscosity. Slag film model is to consider the heat transfer influence of gas generation from concrete decomposition on corium/concrete interface. Crust dissolution model is to consider the effect of crust dissolution by molten

concrete.

Chapter 3 is dedicated to simulations of 1-D MCCI experiments SURC-2 and SURC-4 in order to validate heat conduction, chemical reaction heat and phase change models. 2-D geometry was built to simulate the test sections of SURC-2 and 4 with MPS method. The calculated concrete ablation rate was compared with the experimental measures and the simulation results of CORCON code. The simulation results by MPS agreed well with the experiments, which proved the validity of heat conduction, chemical reaction heat and phase change models. The experimental and MPS results both indicated that Zr oxidation could increase the ablation rate. It also suggested that crust formation/remelting play an important part in MCCI progression, because the crust layer acts a thermal insulation layer between the melt and concrete.

Chapter 4 presents the simulation of 2-D MCCI experiments CCI-2 and CCI-3 in order to validate slag film and crust dissolution models and investigate the isotropic/anisotropic ablation mechanism. MPS simulation successfully distinguished the two different experiments with mechanistic simulation. Moreover, the isotropic/anisotropic ablation mechanism has been indicated through study on different simulation cases based on CCI-2 and 3 with different assumptions. The simulations have indicated that the isotropy/anisotropy mainly depends on the crust formation and natural convection in the melt pool. Aggregates with higher density and thermal conductivity can favor crust formation and consume more power from the melt pool, thus can slightly promote anisotropy. Besides, there exists inherent anisotropy of natural convection in an internally heated pool. On the other hand, gas generation can increase the heat transfer at corium/concrete interface on both basemat and sidewall, thus can facilitate isotropy.

Chapter 5 presents the simulation of 3-D MCCI experiments VULCANO-VB U7 and COMET-L3 in order to further investigate influences of the factors, which are spatially dependent. Simulations of both experiments were carried out with 3-D geometry. Besides the important roles of crust formation, gas generation, and aggregates

that play in MCCI progression, MPS simulation results also showed the post-test profiles of both experiments which cannot be obtained accurately by other codes.

Finally, from the simulations carried out by MPS method for 1-D, 2-D and 3-D MCCI experiments, the following isotropic/anisotropic ablation mechanisms have been shown:

- Isotropic ablation mechanism of limestone concrete: The sidewall and basemat crusts lead to isotropy in the boundary heat resistance. Formation of the slag-film at the crust-concrete boundary due to rich gas content of the concrete promotes the boundary heat transfer at the basemat while reduces it at the sidewall. The resultant anisotropy acts in the opposite direction to the anisotropy developed by the temperature stratification of the melt pool, caused by natural convection. As the result, the overall concrete ablation proceeds more or less isotropic
- Anisotropic ablation mechanism of siliceous concrete: Sidewall crust may not be formed due to continuous release of aggregates by concrete ablation. On the other hand, thermally stable aggregates near the corium-basemat boundary act as heat sink and stabilize the basemat crust, leading to substantial anisotropy in the boundary heat resistance, which is the main cause of the anisotropic ablation. The corium pool temperature stratification, developed by natural convection also contributes to the anisotropy.

Chapter 6 summarizes the whole thesis. The MPS method used in this study is able to model the basic thermal-hydraulics and phase change mechanistically. Furthermore, in this study, the MPS method for MCCI simulation has been developed and applied to multi-dimensional MCCI experiments systematically (from 1-D through 3-D) and this approach has succeeded in attaining the following achievements:

- The complex interactions of influential factors in MCCI has been understood through mechanistic modeling and succeeded in discussing discrepancies of calculated results with experimental results with respect to fundamental physical phenomena.
- By limiting use of empirical models to some of the influential factors and modeling interactions of these influential factors mechanistically, discussions have been

successfully developed regarding the mechanism that distinguishes isotropic ablation of limestone concrete and anisotropic ablation of siliceous concrete by oxidic corium.

Acknowledgement

I would like to express my special appreciation and sincere gratitude to my supervisor Assistant Professor Akifumi Yamaji for being a great mentor in my Ph.D. study and life. Without his guidance and help in my research in every possible way, I would not have been able to achieve my Ph.D. study successfully. His rigorous and hardworking attitude towards research will continue to inspire me as a researcher in my future career.

I would also like to express my thanks to Dr. Yoshiaki Oka, Emeritus Professor of the University of Tokyo, for his excellent guidance during the first and half years of my Ph.D. study and kind support afterwards. I am also thankful for the excellent example he has set as a successful professor and research scientist.

My sincere thanks are also expressed to Professor Shinichi Morooka, Professor Masakazu Washio and Professor Seiichi Yokobori, for their valuable comments and suggestions on completing this thesis.

My heartfelt thanks also go to every previous and current member of previous Oka Laboratory and current Yamaji Laboratory during the past three years of my Ph.D. study. Without their help, my study and life in Japan would not have been so colorful and interesting.

My sincere gratitude is also expressed to Dr. Seiichi Koshizuka, Professor in the University of Tokyo and Dr. Kazuya Shibata, Assistant Professor in the University of Tokyo, for providing the basic MPS code, MPS-SW-MAIN-Ver 2.0 and allowing me to attend their laboratory meeting every week, which has facilitated my study carried out with MPS method.

I would also like to thank Dr. Journeau Christophe of CEA Cadarache for providing the experimental report of VULCANO VB-U7 experiment, which has been important to my study.

The financial support from China Scholarship Council (CSC) for my Ph.D. study is

also greatly appreciated.

Finally I would like to thank my family, especially my parents, and my dear friend David Evans for all their constant love and encouragement.

Contents

List of Figures

List of tables

Chapter 1 Introduction

1.1 Introduction

Nuclear safety has always been a major concern since there has been a strong awareness of the potential hazard of radioactive material release from nuclear power plants. It is acknowledged that the potential major release of radioactive materials to the environment could only occur when a severe accident involving a meltdown of the nuclear reactor core happens. In a typical nuclear power plant, for instance, for water reactors at power operation, there are four physical barriers to confine fission products: the fuel matrix, the fuel cladding, the boundary of the reactor coolant system, and the containment system (IAEA, 1996) (see Fig. 1-1). In a severe accident, the fuel rods could melt due to lack of coolant to remove decay heat, thus leading to the first and second barrier to fail. The high temperature molten fuels then will relocate to the lower plenum and threatens the third barrier, RPV. If the cooling of the high temperature molten fuels is not ensured, it is likely the RPV will be breached, causing the third barrier to fail. In this case, to ensure the integrity of the containment building is of crucial importance for severe accident management to prevent substantial release of radioactive materials to the environment (IAEA, 1996).

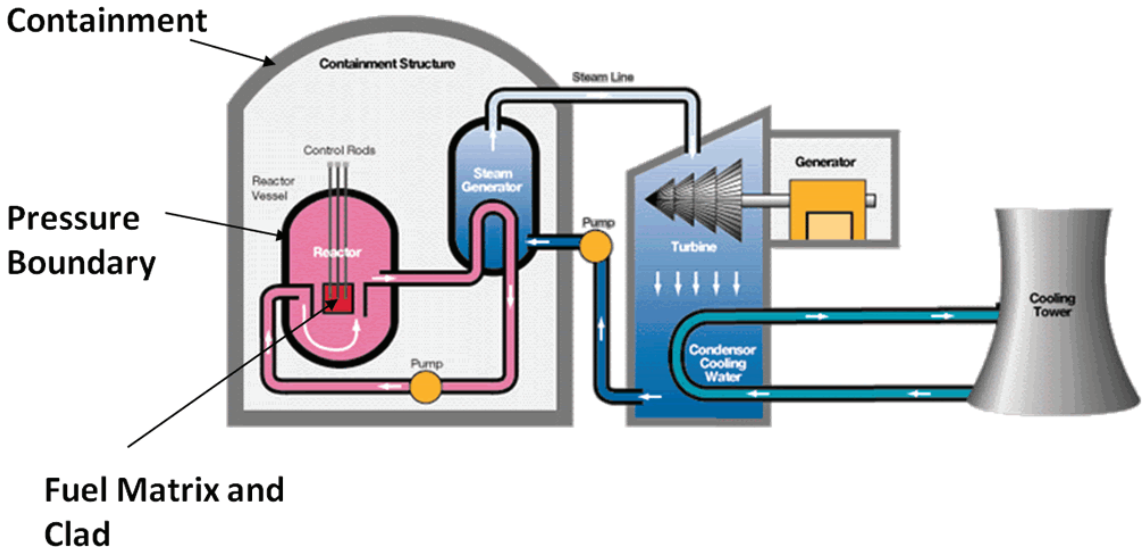

Fig. 1-1 Four physical barriers in a typical nuclear power plant

(http://www.barc.gov.in/pubaware/snr_dls.html)

In a hypothetical severe accident scenario in a light water reactor (LWR), the late containment failure could be caused by melt-through of the reactor pit by core melt or molten corium which is discharged from the failed RPV. This scenario is called Molten Corium-Concrete Interaction (MCCI) and could lead to long-term ablation of the reactor pit in both axial and lateral directions due to the considerable decay heat in the corium (Sehgal, 2011) (see Fig. 1-2). If sufficient cooling is not provided to ensure the corium is cooled down to the solidification temperature, the consequences can be catastrophic since the integrity of containment could be threatened by possible containment basemat melt-through. Consequently, a large amount of fission products would be released to the environment and cause possible severe radiological, environmental and health consequences (IAEA, 1997). In the light of these consequences, the progression of MCCI should be investigated intensively to understand its process and prevent its consequences.

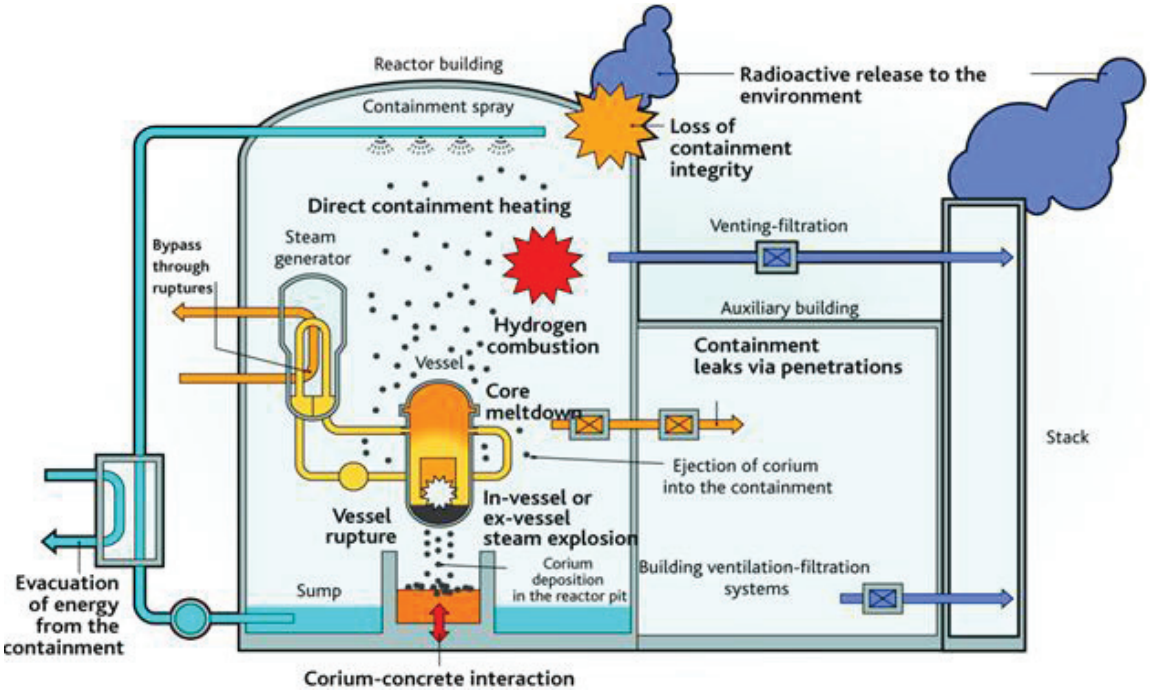

Fig. 1-2 Illustration of MCCI and its possible consequences in a typical LWR (Haste, 2015)

There are three major severe accidents during the past six-decade history of

commercial nuclear power generation (Hirschberg et al., 1998; Dyer et al., 2013):

- Three Mile Island-2 (USA, 28 March 1979) where the reactor was severely damaged but radiation was contained and there were no adverse health or environmental consequences.
- Chernobyl-4 (former Soviet Union, 26 April 1986) where the destruction of the reactor by steam explosion and fire killed 31 people and had significant health and environmental consequences. The death toll has since increased to about 56.
- Fukushima Daiichi Nuclear Power Plant (Japan, 11 March 2011) where three of the six reactors (Units 1, 2, and 3) were damaged, followed by loss of cooling to the reactor cores due to a huge tsunami triggered by the Tōhoku earthquake. There were nuclear meltdowns and containment vessel breaches in Unit 1-3. Radionuclides were released from the plant to the atmosphere and deposited on land and ocean (Amano, 2015).

Among the three major severe accidents, it was only in Three Mile Island-2 accident that the partially molten core was able to be constrained with the RPV. For Chernobyl-4 accident, some researchers believed that MCCI scenario occurred in Chernobyl-4 (Rohde, et al., 1992). As regard to Fukushima accident, based on the analytical results by MAAP code by TEPCO (TEPCO, 2013; TEPCO, 2015) and MELCOR code by Sandia National Lab (Gauntt et al., 2012), it is very likely that MCCI must have occurred in Units 1-3, but was suppressed and the molten corium remained in the pedestal floor. From the lessons that can be learnt from the past study on Chernobyl-4 and Fukushima, it is necessary to carry out an intensive study on MCCI in order to further ensure the safety and reliability of nuclear power.

1.2 Phenomenology of MCCI

1.2.1 Important phenomena in corium pool

The phenomenology of MCCI involves a number of complex physical and chemical phenomena as shown in Fig. 1-3. First, the molten corium from reactor core leads to the

buildup of a corium pool in the concrete cavity. The corium pool is usually comprised of melting or partial melting oxides such as UO_2 and ZrO_2, and metals such as stainless steel, Cr, and Zr. The typical initial temperature of the corium pool could reach as high as 2200℃, which is much higher than the onset melting temperature of common concrete with a melting temperature range from 1100℃ to 1500 ℃(Sevón, 2008). Thus, heat from the corium pool is imposed on the concrete surround it and triggers the decomposition and melting of concrete walls of the reactor pit. The decomposition and melting process, which is the so-called ablation process, could last for several hours or days due to the considerable amount of decay heat from the large amount of corium. Thus, although the thermal conductivity of concrete and oxidic corium is low, still a significant amount of concrete could be ablated in an MCCI scenario.

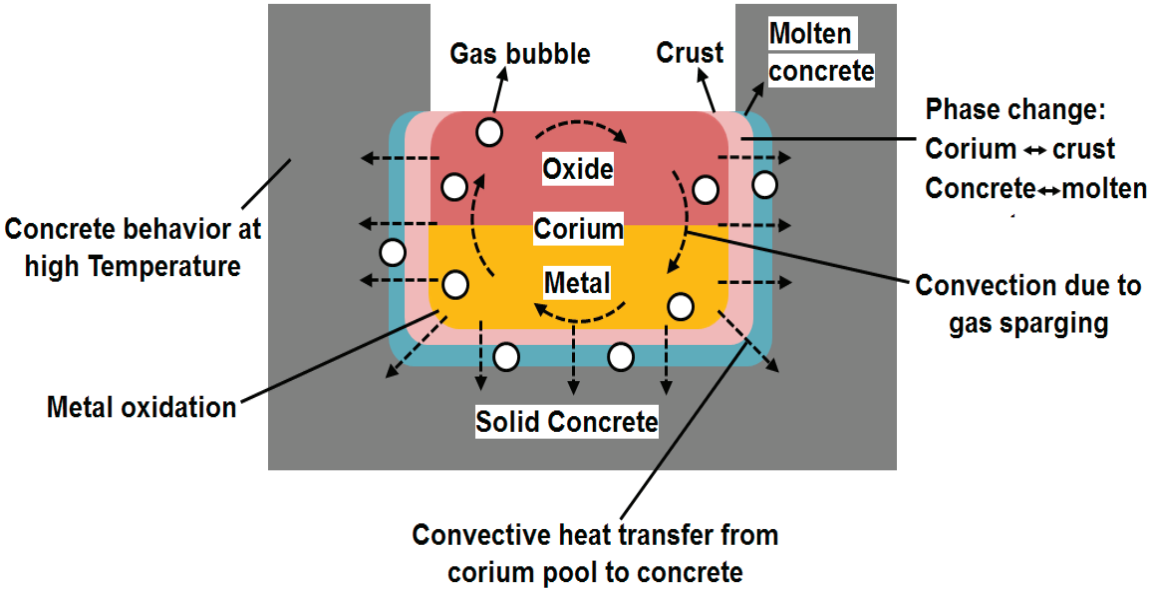

Fig. 1-3 Important phenomena in MCCI

The ablation rate of concrete depends on the heat transfer from the corium to concrete. The heat transfer from corium to concrete then depends on the corium pool behavior which tends to be dynamic during the progression of MCCI. The corium pool behavior of interest is the convection within the corium pool and the continually changing boundaries at corium/concrete interface. The molten concrete as a result of concrete ablation by corium continually forms at the corium/concrete interface and can rise up

and mix into the corium pool. This could lead to the change of compositions of corium pool, which can cause changes of transport and thermophysical properties of the corium pool, such as viscosity, solidus and liquidus temperature, density, and so on. Gas generation, namely H_2O and CO_2, also accompanies the ablation process, leading to bubbling or gas sparging, which can enhance the convective heat transfer in the corium pool.

On the other hand, solidified corium, which is so-called crust, could possibly form at the corium/concrete interface. If water injection is rendered on the top of corium pool as a mitigation measure during MCCI, namely top water flooding, crust can also form on the top of corium pool. Since the thermal conductivity of crust is low, it can serve as an insulation layer between corium pool boundary and concrete or between the upper boundary of the corium pool and water pool. Thus, crust can on one hand slow down the concrete ablation process in MCCI, while on the other hand, reduce the effectiveness of top water flooding. However, crust usually cannot stay stable for a long period since it is constantly subjected to both thermal attacks from the corium and mechanical attack from the decomposition gas of concrete. Melt eruptions could also occur when decomposition gas creates defects in the upper crust and carries melt through these defects to the overlying water pool. Some MCCI experiments involving top water flooding have shown that it is very likely that the crust might attach to the sidewalls of concrete cavity and be separated from the corium pool as the MCCI progression continues downward, causing a void region to be observed in the final concrete cavity of the experiments such as MACE, CCI and COMET (Farmer et al., 2000; Farmer et al., 2005; Alsmeyer et al., 2007). However, the mechanical strength study of the corium crust has shown that the anchored crust is not likely to appear in a real nuclear plant case (Farmer, 2011). Instead, it is most likely for the anchored crust to fail and re-establish contact with the corium pool. As a result, the crust formation and break at the corium pool boundaries can be a continuous renewal process, which can add complication to the analysis of conditions at corium pool boundaries.

Besides the decay heat from the fission productions in the oxidic corium, the chemical reaction heat from the oxidation of metal corium can also generate a large amount of heat if the composition of metal corium is high, serving as another heat source in the corium pool. The common metals that might appear in the corium are Zr, Fe, and Cr. These metals will mainly be oxidized by the decomposition gases like water and CO_2 from the concrete. Important chemical reaction equations are as follows (Sevón, 2005):

$$Zr + 2H_2O \rightarrow ZrO_2 + 2H_2 + 6.3\ MJ/kg\ Zr \quad (1\text{-}1)$$

$$Zr + 2CO_2 \rightarrow ZrO_2 + 2\ CO + 5.7\ MJ/kg\ Zr \quad (1\text{-}2)$$

$$2\ Cr + 3\ H_2O \rightarrow Cr_2O_3 + 3H_2 + 3.6\ MJ/kg\ Cr \quad (1\text{-}3)$$

$$2\ Cr + 3\ CO_2 \rightarrow Cr_2O_3 + 3\ CO + 2.8\ MJ/kgCr \quad (1\text{-}4)$$

$$Fe + H_2O + 3.0\ kJ/kgFe \rightarrow FeO + H_2 \quad (1\text{-}5)$$

$$Fe + CO_2 + 480\ kJ/kgFe \rightarrow FeO + CO \quad (1\text{-}6)$$

Particularly for Zr, there is also a dominant effect of the Zr and SiO_2 condensed phase chemistry, namely Zr can react with the SiO_2 which is a common composition of concrete. At the same time, Zr can also be reduced by Fe_2O_3. The chemical reactions can be expressed as flows:

$$Zr + SiO_2 \rightarrow ZrO_2 + Si + 2.1\ MJ/kg\ Zr \quad (1\text{-}7)$$

$$3Zr + 2\ Fe_2O_3 \rightarrow 3ZrO_2 + 4\ Fe + 5.8\ MJ/kg\ Zr \quad (1\text{-}8)$$

After the oxidation of Zr by SiO_2 is completed, the Si as a reaction product from Zr oxidation will also be oxidized by the decomposition gases from concrete:

$$Si + 2H_2O \rightarrow SiO_2 + 2H_2 + 15\ MJ/kg\ Si \quad (1\text{-}9)$$

$$Si + 2\ CO_2 \rightarrow SiO_2 + 2CO + 14\ MJ/kg\ Si \quad (1\text{-}10)$$

It should be noted that the above oxidation reactions are almost all exothermic, except the oxidation of Fe by water and CO_2 is a slightly endothermic process.

1.2.2 Concrete behavior during MCCI

Concrete is a composite material that consists essentially of a binding medium within

which are embedded particles or fragments of aggregate. In hydraulic-cement concrete, the binder is formed from a mixture of hydraulic cement and water (Mehta et al., 2006). To put it simply, concrete is a common construction material comprised of cement, aggregates, and water. Cement, or most commonly used Portland cement, is the basic ingredient of concrete. Cement is a mixture produced from heating raw materials like lime, iron, silica, and alumina, of which the mass percentages and composition are the main determinants of the exact chemical composition of cement. Cement, together with water, acts as a binder of aggregates to form concrete. Aggregates are the main constituents of concrete. They generally make up 65-70% of the total volume of concrete. Therefore, the quality and characteristics of aggregates can determine the overall quality, characteristics and performance of concrete. Aggregates are divided into coarse aggregates and fine aggregates according to size. The coarse aggregates are generally gravels, with aggregate size dominantly higher than 5mm, ranging from 9.5-37.5mm. The fine aggregates are generally natural sand or fine crushed stones, with aggregate size less than 5mm, ranging from 1-4 mm. A common proportioning of each constituent in concrete is shown in Fig. 1-4. In general, concrete is a heterogeneous multiphase material in which aggregates are bonded together with hydrated cement paste (Naus, 2005; Mehta et al., 2006).

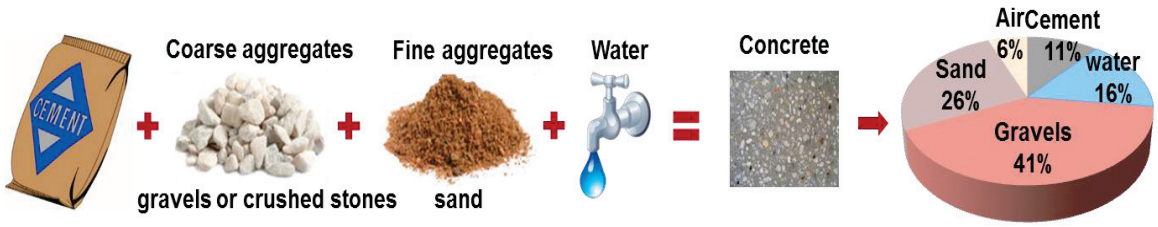

Fig. 1-4 Common composition of concrete

For normal-weight concrete, concrete can be divided into two major types according to the main composition of aggregates, namely siliceous concrete and limestone concrete. The main composition of the aggregates in siliceous concrete is quartz or silica, of which the weight percentage can reach 70%. The commonly used basaltic

concrete is also one type of siliceous concrete, but with approximately 20 wt% lower content of SiO_2 and a higher content of Al_2O_3, MgO and Fe_2O_3. The main composition of the aggregates in limestone concrete is carbonates like $CaCO_3$ or $MgCO_3$. The commonly used Limestone/Common Sand concrete can be classified into limestone concrete, but with approximately 20 wt% higher content of silica and 10 wt% lower content of carbonates. Additionally, serpentine concrete which contains a high amount of mineral water in the serpentine mineral ($Mg_3Si_2O_7 \cdot 2H_2O$) has been used in the Soviet RBMK and VVER types of reactor power plants. The high content of chemically bound water in serpentine mineral leads to gas release in the form of steam when serpentine concrete is heated to decompose. Typical compositions of different types of concrete are shown in Table 1-1 (Strizhov et al., 1996). Different types of aggregates can have different characteristics when subjected to high temperature and thus influence the behavior of concrete under high temperature. For instance, the melting temperature of silica aggregates can reach as high as 2000K, which makes it hard to decompose and might remain intact when subjected to high temperature. On the other hand, the limestone aggregates can easily decompose and generate more gas (CO_2) when subjected to temperature beyond 600℃. Moreover, different types of concrete can have different solidus and liquidus temperature and decomposition enthalpy (the enthalpy needed when heat concrete from room temperature to melting) as shown in Table 1-2 (Strizhov et al., 1996). Limestone concrete generally has higher melting range and decomposition enthalpy than siliceous concrete. These different characteristics can influence the conditions in corium pool as well as at corium/concrete boundaries, which can correspondingly influence the progression of MCCI.

Table 1-1 Typical chemical compositions of different concrete (wt%) (Strizhov et al., 1996)

Composition	Siliceous	Basaltic	Limestone	Limestone/Common Sand	Serpentine
SiO_2	69.00	54.84	3.60	35.80	33.50
CaO	13.5	8.82	45.40	31.30	7.00
MgO	0.70	6.16	5.67	0.48	29.30
Al_2O_3	4.00	8.32	1.60	3.60	N/A
Fe_2O_3	1.00	6.26	1.20	1.44	N/A
Na_2O	0.70	1.80	0.0078	0.082	N/A
K_2O	1.40	5.39	0.68	1.22	N/A
Cr_2O_3	N/A	N/A	0.004	0.014	N/A
MnO	N/A	N/A	0.01	0.03	N/A
TiO_2	0.80	1.05	0.12	0.18	N/A
CO_2	4.23	1.50	35.698	21.154	1.20-1.50
H_2Oevap	3.10	3.86	3.94	2.70	5.00
H_2Ochem	3.68	2.00	2.00	2.00	13.80

Table 1-2 Solidus and liquidus temperature and decomposition enthalpy of different concrete (Strizhov et al., 1996)

Concrete	Solidus temperature (K)	Liquidus temperature (K)	Decomposition enthalpy (MJ/kg)
Siliceous	1403	1523	1.6-2.7
Basaltic	1350	1650	1.5-2.3
Limestone	1690	1875	2.9-5.1
Limestone/Common Sand	1420	1670	2.3-3.2

During MCCI, it is expected that concrete will be exposed to high temperature imposed by molten corium materials. Thus, the behavior of concrete when subjected to elevated temperature is of primary interest. The behavior of concrete and important chemical reactions that can occur when heating concrete to different temperatures until melting are listed in Table 1-3 (Sevon, 2005).

Table 1-3 Behavior of concrete and chemical reactions at different temperatures (Sevon, 2005)

Temperature (℃)	Concrete behavior and chemical reactions
100.0	Evaporation of physically bound water, $H_2O(l) + 2258\ kJ/kg\ H_2O \rightarrow H_2O(g)$
100.0-850.0	Dehydration of hydrates, $3CaO \cdot 2SiO_2 \cdot 3H_2O \rightarrow 2CaO \cdot SiO_2 + CaO \cdot SiO_2 + 3\ H_2O(g)$, (Similar reactions for other hydrates; the reaction heat of these endothermic reactions is about 250-500 kJ/kg hydrate)
400.0-600	Dehydration of calcium hydroxide, $Ca(OH)_2 + 1340\ kJ/kg\ Ca(OH)_2 \rightarrow CaO + H_2O(g)$
574.0	Crystalline transformation from α- to β-quartz; $SiO_2(\alpha) + 12\ kJ/kg\ SiO_2 \rightarrow SiO_2(\beta)$
600.0-900.0	Decomposition of calcium carbonate, $CaCO_3 + 1637\ kJ/kg\ CaCO_3 \rightarrow CaO + CO_2(g)$
1100.0-1500.0	Melting of Portland cement
1462.0	Decomposition of hematite into magnetite $6\ Fe_2O_3 + 480\ kJ/kg\ Fe_2O_3 \rightarrow 4\ Fe_3O_4 + O_2(g)$
1597.0	Melting of magnetite $Fe_3O_4(s) + 600\ kJ/kg\ Fe_3O_4 \rightarrow Fe_3O_4(l)$
1700.0-1800.0	Melting of β-quartz; $SiO_2(s) + 130\ kJ/kg\ SiO_2 \rightarrow SiO_2(l)$

1.3 Past experimental study on MCCI

1.3.1 Early MCCI experiments

A number of MCCI experiments have been carried out since 1980s to investigate the concrete ablation behavior under high temperature with oxidic and metal melt. The purposes and objectives of MCCI experiments are mainly: 1) to identify the important physical and chemical processes in order to understand and assess the most important phenomena during MCCI; 2) to provide quantitative and detailed experimental data to

validate specific models and codes on MCCI analysis (Alsmeyer et al., 1995). The early large-scale experiments, such as TURC (Gronager et al., 1986), SURC (Copus et al., 1989; Copus et al., 1992), SWISS (Blose et al., 1987), ACE (Thompson et al., 1992), and MACE (Spencer et al., 1992), are mostly one-dimensional (1-D) MCCI experiments, aiming at studying 1-D ablation behavior of various concrete by simulant oxidic materials, prototypic oxidic corium or metal, the effect of Zr oxidation on MCCI, the effect of an overlying water pool and the aerosol release from the melt. 1-D MCCI tests were generally carried out with a cylindrical or rectangular concrete block surrounded by insulation materials such as MgO. Only downward/axial ablation of concrete was measured by thermocouples embedded in the concrete block. The corium material was heated until melting within the test crucible or poured into a concrete crucible. Induction heating (when there was metallic component in the corium) or direct electrical heating were used to simulate the decay heat of the corium. A typical experimental apparatus of 1-D test section is shown in Fig.1-5. A summary of the early MCCI experiments is presented in Table 1-4.

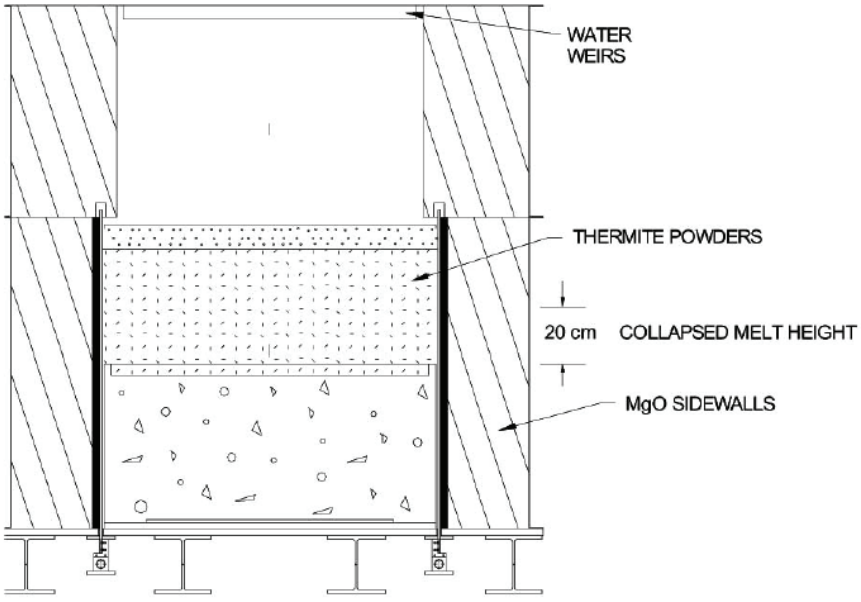

Fig. 1-5 Test section of 1-D MACE 3b Test (Farmer et al., 2000)

Table 1-4 Summary of early MCCI tests

Program	Geometry	Corium	Concrete	Crucible dimension	Parameters
MACE	1-D	UO_2, ZrO_2, Zr, Cr	SIL, LIM	0.3×0.3 m to 1.2×1.2 m	Coolability issue, crust anchoring
ACE	1-D	UO_2, ZrO_2	SIL, LIM, LCS	0.5×0.5 m	Decay power level; Initial Zr oxidation of fission products
TURC	1-D	Fe/ Al_2O_3, Fe, or UO_2, ZrO_2, Zr	LCS	0.416m D	Transient test; Corium composition
SURC	1-D	Steel with Zr; UO_2, ZrO_2 and Zr	SIL, LIM, BAS	0.4m D	Zr-SiO2 condensed phase reactions; Decay power level
WECTOR	1-D	Al_2O_3, CaO	LCS	0.32m D	Overlying Water pool
SWISS	1-D	Stainless steel	LCS	0.216m D	Overlying Water pool
BETA	2-D	Fe, Zr, Cr, Ni, Al_2O_3, CaO	SIL, LCS	0.38m D	Decay power level

The results of 1-D MCCI tests can be concluded as the following aspects (Alsmeyer et al., 1995):

(1) Gas release during 1-D MCCI from concrete ablation is strongly dependent on concrete types, as expected. For limestone or limestone/common sand concrete, there is a large amount of CO_2 release, especially for pure limestone of concrete, the amount of CO_2 release can be 3 times higher than steam release. On the other hand, siliceous or basaltic concrete (and to a considerably higher amount serpentine concrete) release mainly steam/water vapor and much less CO_2 compared to limestone-rich concrete. If there is metal in the original corium, H_2O and CO_2 can be reduced to H_2 and CO by metal oxidation.

(2) The oxidation of Zr by water and condensed phase reaction with SiO_2 in concrete can considerably accelerate concrete ablation by introducing chemical heat into corium pool and thus increase the corium pool temperature. Additionally, as per Eqs. 1-9 and 1-10, elemental Si can be formed and participate in the later oxidation reactions with H_2O and CO_2 for temperature above 1900 °C.

(3) The ablation rate of concrete during 1-D MCCI tests can range from several to tens of centimeters per hour, controlled by the melt superheat and chemical oxidation of Zr. Typical concrete ablation rate shown in stable phase of MCCI is several centimeters per hour. Tests with only metallic corium such as stainless steel show relatively higher ablation rates than that of tests with oxidic corium, owing to the higher thermal conductivity of metals.

(4) Melt coolability seems to be weak in small-scale MCCI quenching tests, e.g. SWISS and WECTOR, since a solid crust was observed to form and isolate the corium pool from the top water pool. However, this might not apply to prototypical due to the rather small-scale of the test sections and simulant corium used in the tests.

(5) Aerosol and fission product release during MCCI mainly depends on the temperature and chemical composition of the corium. If I, Cs, and Te are still present in the melt, these are released to a high degree. The other low volatile fission products, e.g. Sr, Ce, La, Ba, and Mo are only released in small quantities, generally below 1 % (e.g. ACE experiments). It was observed that silica rich melts have a higher retention capability for some of the fission products than limestone-rich corium (Alsmeyer et al., 1995).

1.3.2 Recent MCCI experiments

As described above, the early 1-D MCCI tests had identified several important aspects about MCCI. However, there were still remaining issues regarding corium composition and more importantly two-dimensional (2-D) concrete ablation, namely basemat and sidewall ablation as in a real reactor pit. Although BETA test series (Alsmeyer, 1987) and M0 test in MACE test series (Farmer et al., 2000) showed some light upon the 2-D concrete ablation pattern, BETA tests were carried out with only metal and simulant oxidic materials, while M0 test was performed in a small limestone/common sand concrete crucible (0.3×0.3 m) with 70% oxidized PWR corium in a relatively short test duration (about 1 hour). Apparently, more experimental study was necessary to investigate MCCI with prototypic corium and different types of concrete in 2-D geometry.

Another important issue that requires further study is melt coolability with larger-scale concrete cavity and prototypic corium materials. Thus, more recent MCCI experiments focused on mainly two subjects: 1) the 2-D concrete ablation pattern with respect to axial and radial ablation rates and 2) melt coolability issue with prototypic materials in a 2-D concrete cavity geometry and late water injection. Table 1-5 presents a brief summary of more recent MCCI experiments. As can be seen, most 2-D experiments studied 2-D concrete ablation pattern with prototypic corium materials. 2-D MCCI experiments are generally carried out in a cylindrical or rectangular concrete cavity. The molten corium materials are generated with thermite reactions on site or in a furnace and then poured into the concrete cavity. Induction or direct electrical heating is used to simulate decay heat. Especially in MOCKA experiments, decay heat is provided from chemical reaction heating through continuously adding thermite into the corium pool.

In a series of CCI experiments performed by OECD/NEA (Farmer et al., 2006), VULCANO VB test series (Journeau et al., 2009) and COTELS tests (Maruyama et al., 2006), one of the major findings was that the two-dimensional dry ablation pattern of concrete with prototypic oxidic corium melt seems to correlate with the composition of concrete. In the tests carried out with siliceous (silica-rich) concrete, an anisotropic pattern, in which the lateral ablation was more significant than the axial ablation has

been observed. On the other hand, in the tests carried with limestone concrete, a more isotropic ablation pattern, in which the lateral and axial ablations tended to be similar, has been observed (see Fig. 1-6).

As to the reason for isotropic and anisotropic ablation patterns in limestone-rich and silica-rich concretes, one explanation is that these two types of concrete use different aggregates as constituent materials. As previously mentioned, limestone-rich concrete is comprised of limestone aggregates ($CaCO_3$) which will decompose into CaO and CO_2 at a temperature of 973-1173K. On the other hand, the siliceous concrete is composed of silica aggregates (SiO_2), which could stay thermally stable even at a temperature as high as 2000K. Due to the apparently different behavior of aggregates at high temperature, the anisotropic ablation in siliceous concrete could be explained that this phenomenon is caused by the existence of relatively stable aggregates (silica), which still remain solid and stable at concrete melt or decomposition temperature and act as cold sources in the corium pool, thus contributing local crust on the basemat surface preventing downward/axial ablation and leading to a tendency of much easier and pronounced lateral sidewall ablation. The isotropic ablation in limestone concrete, on the other hand, indicates a more homogeneous distribution of heat flux in the axial and lateral directions, which can be justified by a more homogenous melt pool under the effects of gas sparging and less stable crust due to relatively large amount of gas generation from limestone concrete. However, additional experiments and analysis are needed to support these theories.

Since there is limited margin between the sidewall and the containment liner in some of the containment designs such as BWR Mark-I, ablation of sidewall may require more careful evaluation. Therefore, it is important to investigate the mechanism of isotropic and anisotropic ablation patterns in order to stress the issue of quantifying basemat and sidewall ablation depths. However, current experimental study is not adequate to reveal the mechanism of isotropic and anisotropic ablation. Thus, it is necessary to develop numerical mechanistic methods based on fundamental principles of fluid dynamic and hear transfer to investigate and clarify the mechanism.

Fig. 1-6 Final cavities showing isotropic and anisotropic ablation patterns in CCI-2 and CCI-3 tests (Farmer et al. 2005)

Table 1-5 Summary of recent MCCI tests

Program	Geometry	Corium	Concrete	Parameters
CCI	2-D	Prototypic PWR corium with concrete	LCS, SIL	Concrete composition, top water flooding
VULCANO	2-D	UO_2, ZrO_2, SiO_2	LCS, SIL	Concrete composition, corium composition
COMET-L	2-D	Fe, Ni, Al_2O_3, CaO	SIL	Top flooding; stratified melt pool
COTELS	2-D	UO_2, ZrO_2, Zr; Fe	SIL	Concrete/mortar Flooding
MEK-T1A	1-D	Alumina-thermite	BAS	Transient test
MOCKA	2-D	Fe, Ni, Al_2O_3, CaO	LCS, SIL	Concrete composition; stratified melt pool
HECLA	2-D	Stainless steel	SIL	Transient test

1.4 Past numerical study on MCCI

Besides the experimental efforts on MCCI, several computer codes have also been developed in the aim of modeling the physical and chemical phenomena during MCCI, such as WECHSL/WEX (Foit et al., 1995; Langhans et al., 2001), CORCON/CORQUENCH (Strizhov et al., 1996; Farmer, 2001), COSACO (Nie et al., 2002), MELCOR (Gauntt et al., 2005), TOLBIAC-ICB (Spindler et al., 2006), and ASTEC/MEDICIS (Cranga et al., 2007). The main characteristics of the heat transfer models and assumptions used in these codes are listed in Table 1-6. Here only several important models and criteria of the codes have been included. A brief introduction of these codes can be found in the COMET-L2 and 3 benchmark study (Spindler, et al., 2007). In general, these codes are highly dependent on empirical heat transfer correlations and various models of the corium pool such as the pool stratification models and the pool/concrete interface models. At the same time, only 1-D or simplified cylindrical or rectilinear 2-D geometry with average axial and radial ablation depths can be evaluated. Although previous code validations against experiments and benchmark calculations such as CCI-2 experiment and COMET-L2 experiment have been carried out, it can be seen from Figs. 1-7 to 1-10 that large discrepancies on the predictions of axial and lateral ablation fronts can be found among these codes. The discrepancies were mainly caused by different choices of empirical correlations such as heat transfer correlations at concrete/melt pool side/ bottom/upper surface and different corium pool boundary temperatures. It can be inferred that there will also exist large discrepancies and uncertainties when it comes to the prediction of the shape of the ablated cavity. In fact, in the reactor benchmark study, in which a simple cylindrical reactor pit of 3m in radius and 6m in basemat axial thickness, the discrepancies on the prediction of reactor cavity shape evolution have also been observed (as shown in Fig. 1-10).

Besides code development and validations, the heat transfer analysis of CCI experiments 1-3 carried out by Sevón (Sevón, 2008) presented an attempt to evaluate the heat transfer coefficients between corium pool and concrete. The heat transfer correlations developed from the experimental value indicate that the heat transfer coefficients between corium pool and concrete are linearly correlated with superficial gas velocity from the corium/concrete interface. The deviations of these correlations range from 19-27%.

From the discussions above, it is obvious that the limitations of empirical correlations and models that are currently used in the codes as well as the lack of understanding of the isotropic/anisotropic mechanism have constrained their capability for accurate predictions of cavity ablation depths and profile. This suggests a necessity to develop a multi-dimensional code based on fundamental governing equations to further improve the accuracy and reliability of numerical analysis of MCCI.

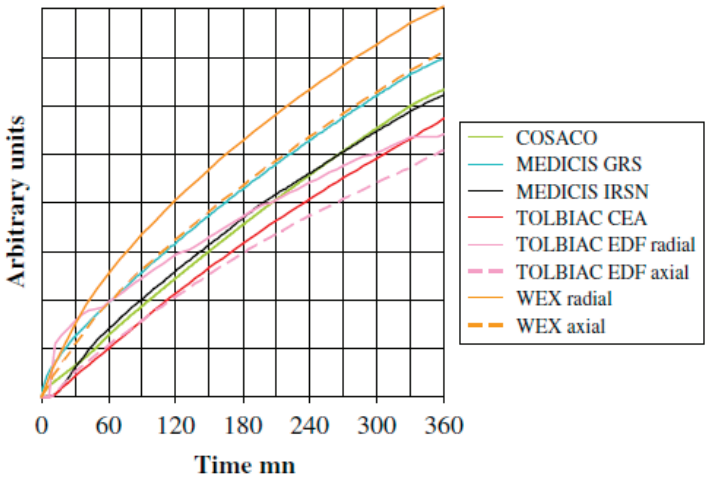

ablation depth versus time.

Fig. 1-7 Predictions of ablation depth in CCI-2 experiment by different codes (Cranga et al., 2010)

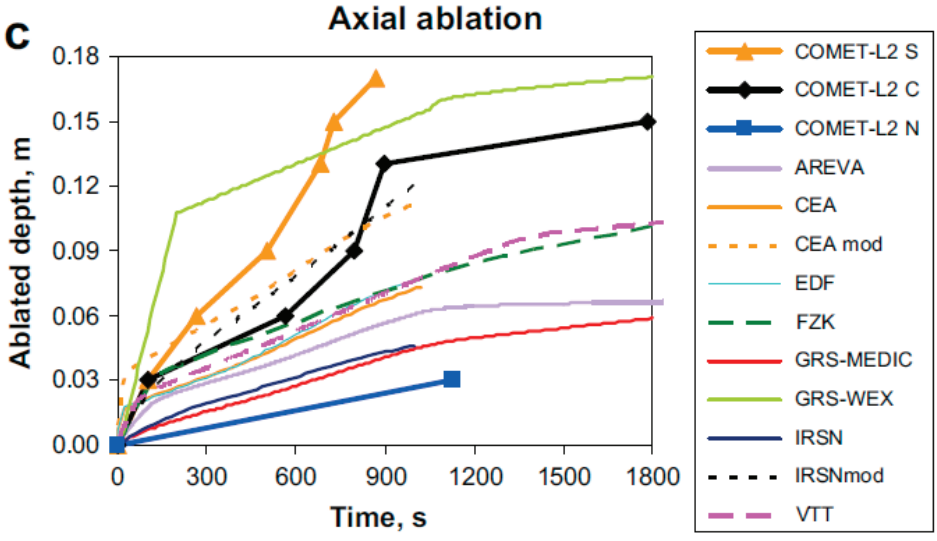

calculated and measured axial ablation versus time.

Fig. 1-8 Predictions of axial ablation depth evolution in COMET-L2 experiment by different codes (Cranga et al., 2010)

Table 1-6 Main models and assumptions of current MCCI codes (Spindler, et al., 2007)

Code	ASTEC/MEDICS by GRS	ASTEC/MEDICS by IRSN	COSACO	CORCON CORQUENCH	MELCOR	TOLBIAC-ICB	WECHSL WEX
Heat transfer at concrete/pool side	Correlation from experimental results	BALI (Bonnet, 2000)+slag layer	BALI	(Kutateladze and Malenkov, 1978)	Slag layer	BALI	Depending on the existing gas flow
Heat transfer at concrete/pool bottom	Correlation from experimental results	BALI +slag layer	BALI	(Kutateladze and Malenkov, 1978)	Kutateladze	BALI	Depending on the existing gas flow
Heat transfer at pool upper surface	Correlation from experimental results	BALI	BALI	(Kutateladze and Malenkov, 1978)	Modified Kutateladze	BALI	Depending on the existing gas flow
Heat transfer at oxide/metal interface	(Greene and Irvine, 1988)	Greene	BALI	Not used	Greene	BALI	(Werle, 1982)
Pool/crust interface temperature	$T_{solidus}$	$0.8*T_{liquidus}+0.2*T_{solidus}$	Not used	$T_{solidus}$	$T_{solidus}$	$T_{liquidus}$	$T_{solidus} \leq T_{int} \leq T_{liquidus}$
Crust composition	Pool composition	Pool composition	Refractory material	Pool composition	Pool composition	Refractory material	Pool composition
Tsolidus and Tliquidus vs. oxide composition	Roche et al. 1993	NUCLEA data base (Cheynet et al., 2004)	COS-CHEM data base	Roche et al. 1993	Assuming ideal solutions	NUCLEA data base	Input data
Stratification criterion	Not used	Modified BALISE criterion	Density	Not used	Density	BALISE criterion	Not used

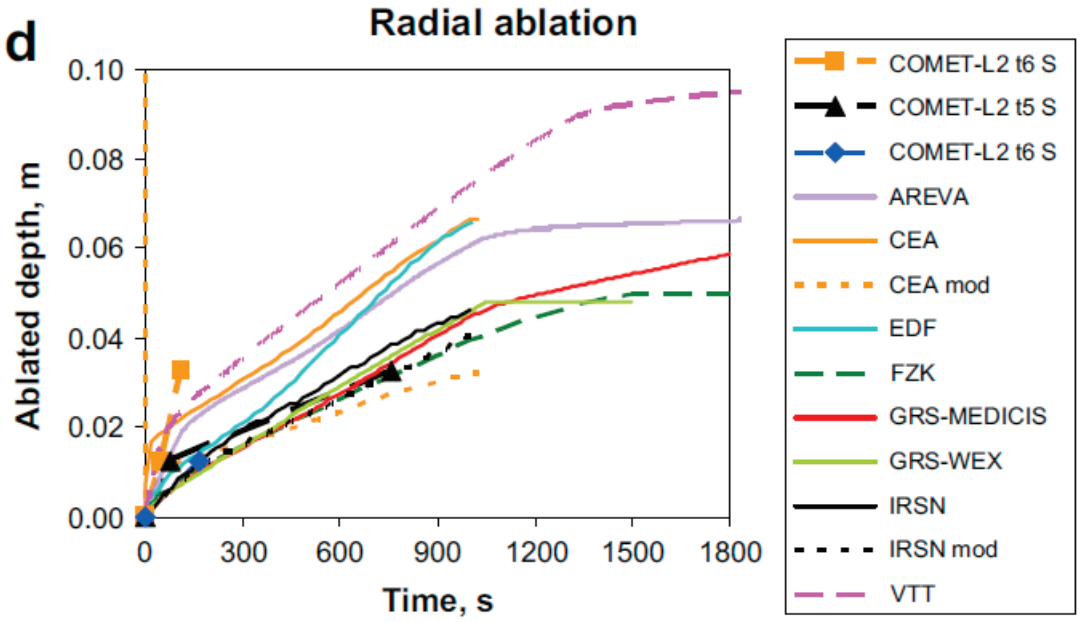

calculated and measured lateral ablation versus time.

Fig. 1-9 Predictions of lateral ablation depth evolution in COMET-L2 experiment by different codes (Cranga et al., 2010)

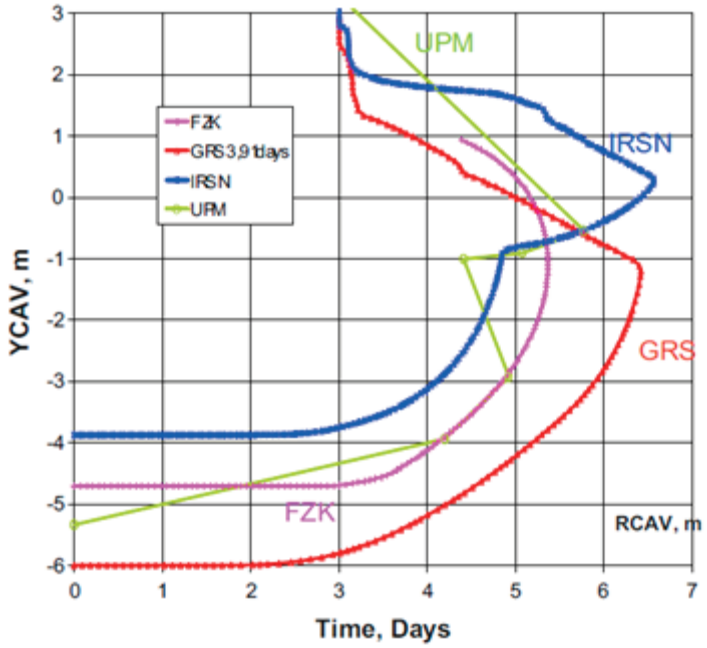

Fig. 1-10 Predictions of reactor cavity shape evolution, stratified pool, limestone
UPM: MELCOR; IRSN: ASTEC/MEDICIS; GRS: WEX; FZK: WECHSL (Cranga et al., 2010)

1.5 MPS method for MCCI analysis

1.5.1 The advantages of MPS method for MCCI analysis

From the previous review on past numerical study on MCCI, it can be concluded that the difficulty in understanding and predicting MCCI with these past computer codes arises not only from the difficulty in accurate modeling of thermal-hydraulics (heat transfer and convection) and phase change which governs MCCI, but also the difficulty in accurately modeling complex interactions of various influential factors, e.g., chemical reaction heat, formation of slag-film at boundaries, crust formation, dissolution and remelting, relocation of thermally stable aggregates, etc. As the results, the past studies had the following issues:

- Difficulties in understanding discrepancies among simulations or among simulation and experimental results in terms of physical phenomena.
- Good agreement of calculation results with experimental results does not necessarily assure appropriate modeling, because of adjustments of various parameters in the empirical correlations.

Considering the limitations of current MCCI codes highly dependent on empirical correlations and the importance and necessity to develop a mechanistic numerical method based on fundamental governing equations mentioned in the previous section, this study has introduced Moving Particle Semi-implicit (MPS) method into multi-dimensional MCCI study.

MPS method is a particle method using Lagrangian frame of reference for analyzing incompressible media first developed by S. Koshizuka and Y. Oka (S. Koshizuka and Y. Oka, 1996). As a Lagrangian method, MPS method discretizes the computation domain with particles instead of meshes or grids to represent the system and record its evolution. Thus, large distortions of meshes or grids can be avoided when dealing with boundaries or interfaces in numerical simulations. Also, generating and refining initial particle configuration of computation domain is much easier compared with mesh generation when the geometry of computation domain is complicated. The governing equations are

also discretized through weight function and particle interaction models in the Lagrangian frame of reference. In conventional Eulerian mesh/grid method, the simulation object is generally located or moves across the fixed mesh cells in space, with merely fixed locations in the computation domain can be tracked. In contrast, MPS method can track each particle that possesses a set of field variables such mass, position, velocity, temperature, enthalpy etc. As a result, the advantages of MPS method are that it can easily and accurately capture free surfaces, interfaces, boundaries and fluid thermophysical properties. Phase change can be mechanistically modeled by tracing the enthalpy of each particle. Convective heat transfer within the corium pool can be modeled by directly solving energy conservation equation combined with Navier-Stokes equation and continuity equation. These advantages of MPS method provide superiority to other methods when simulating important phenomena involving dynamic evolution of solid-liquid boundary and temperature stratification caused by convection that is observed in MCCI. Especially, the complex conditions and temperature at corium/crust/concrete interface can be evaluated rather than assume its state and temperature empirically as other MCCI codes do. Moreover, different 2-D or 3-D geometries of concrete cavity can be established accurately, which can further facilitate more accurate simulation of concrete ablation profile evolution with time in MCCI. Thus, these advantages of MPS method can promote more mechanistic understanding of the important determinants that control MCCI progression and promote more precise simulation of important parameters such as concrete ablation profile evolution in MCCI.

The above featured advantages of MPS method have been validated against various physical phenomena in a in a wide range of engineering applications including nuclear engineering (Tian et al., 2010; Chen et al., 2010; Li et al., 2013a, 2013b), chemical engineering (Chen et al., 2011) and ocean engineering (Shibata et al., 2012). Especially in nuclear engineering, the MPS method has been validated and proved effective to analyze a number of phenomena in a severe accident of LWR molten core spreading (Kawahara and Oka, 2012; Matsuura and Oka, 2013), stratification and

solidification/melting behaviors (Li et al., 2014), melt penetration and freezing behavior in an instrument tube (Chen and Oka, 2014a, 2014b).

1.5.2 Past research on MCCI analysis by MPS method

Besides the wide range of validation and application of MPS method mentioned in the previous section. There have also been successful attempts of applying MPS method to MCCI analysis by other researchers previously.

The first attempt of introducing MPS method to MCCI analysis was achieved by S. Koshizuka in 1999 (S. Koshizuka et al, 1999). In this study, the developed MPS code was applied to a 1-D MCCI test SWISS-2 carried out by Sandia National Laboratory. In SWISS-2 test, 304 stainless steel was used as corium to interaction with a cylindrical test section with limestone/common sand concrete as basemat and surrounded by MgO sidewall. Top water flooding was initiated from 99.0 second in the test. 2-D geometry of the test section was built as shown in Fig. 1-11. Only heat conduction was assumed among the melt pool, concrete and MgO (sidewalls). Phase change was modeled based on the enthalpy of particles. Nucleate boiling is considered by a simple correlation related to the temperature difference ΔT of melt pool and water pool. Gas release accompanied by the concrete ablation is ignored.

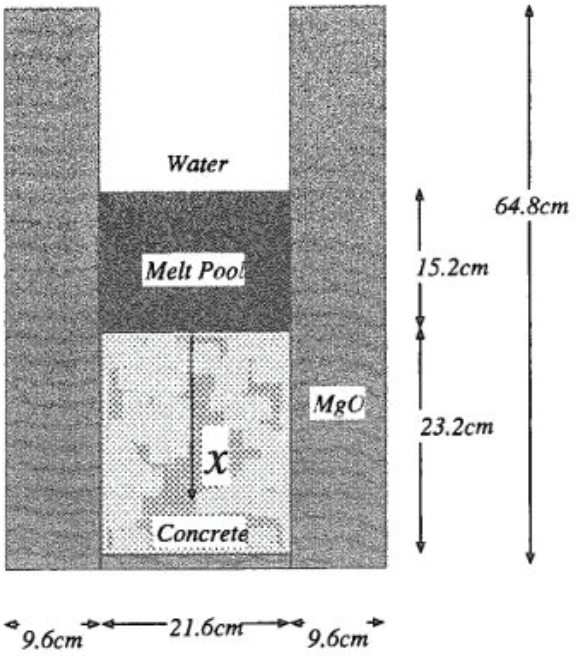

Fig. 1-11 Simulation geometry of MCCI test SWISS-2 by S. Koshizuka (S. Koshizuka et al, 1999)

Figure 1-12 shows the MCCI progression in SWISS-2 test. Some crust started to form from 60 second, but they soon remelted. The stable top crust supported by the MgO sidewalls above melt pool started to form at 500 second. The crust was almost flat and the thickness of crust stayed constant until the end of the test.

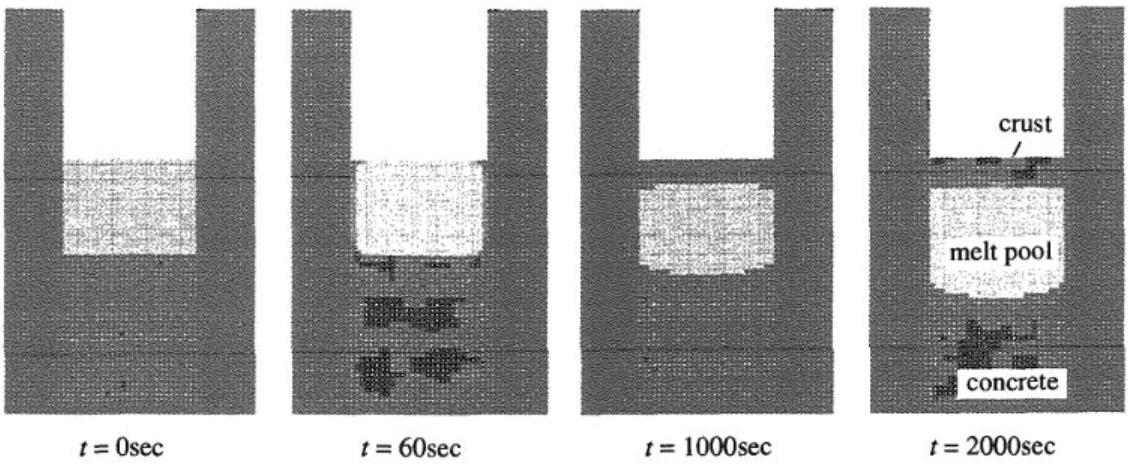

Fig. 1-12 Representative moments in SWISS-2 MPS simulation (S. Koshizuka et al, 1999)

Figure 1-13 shows the comparison of the depth of concrete ablation front between MPS simulation and the experimental measurements. As can be seen from the figure, the MPS simulation underestimated the depth of ablation front from 500 second. This is probably due to the overestimation of the heat flux to the overlying water pool and thus leads to the underestimation of the heat flux to the concrete. Moreover, the gas generation was ignored, which might also lead to underestimation of heat flux to the concrete.

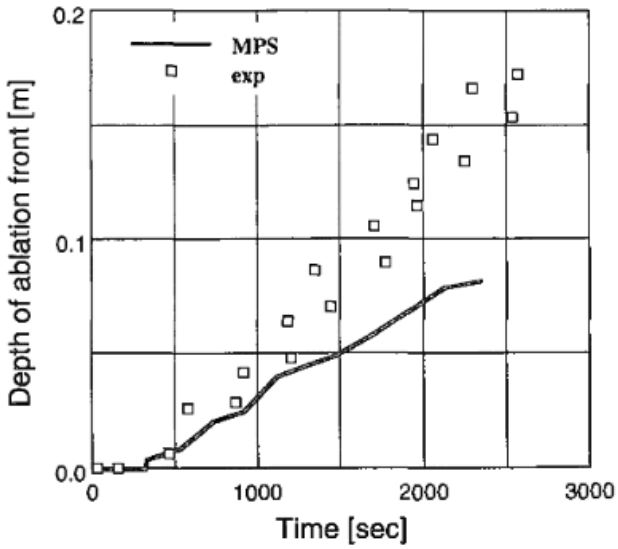

Fig. 1-13 Concrete ablation fronts by MPS simulation and experimental dada (Koshizuka et al, 1999)

Another MCCI study by MPS method was carried out by P. H. Chai (Chai et al., 2015). The MPS simulation was carried out on 2-D MCCI experiment CCI-2. CCI-2 used prototypic PWR corium with 8 wt% molten LCS concrete to interact with a specially designed rectangular basemat and sidewall made of LCS concrete. In Chai's MPS study, two novel mixing models were developed to consider the molten concrete mixing into the corium and the corresponding change of physical properties within the melt pool. Mixing model 1 (see Fig. 1-14) simply assumes that once the molten concrete particle touches the corium particles, this concrete particle will appear to have been mixed into the melt pool and its type will be switched from concrete to corium.

Meanwhile, the physical parameters of the melt pool are constantly updated to conserve the total mass and energy as shown in Eq. 1-11.

$$\varphi_{melt} = \frac{\varphi_{melt} * (total\_corium - total\_crust) + \varphi_{concrete} * total\_melt}{total\_melt} \tag{1-11}$$

where total_corium is the initial total number of corium particles, total_crust is the total number of crust particles, total_melt is the total number of melted particles, φ can represent the physical properties of particles such as viscosity, density, thermal conductivity and specific heat (Chai et al., 2015).

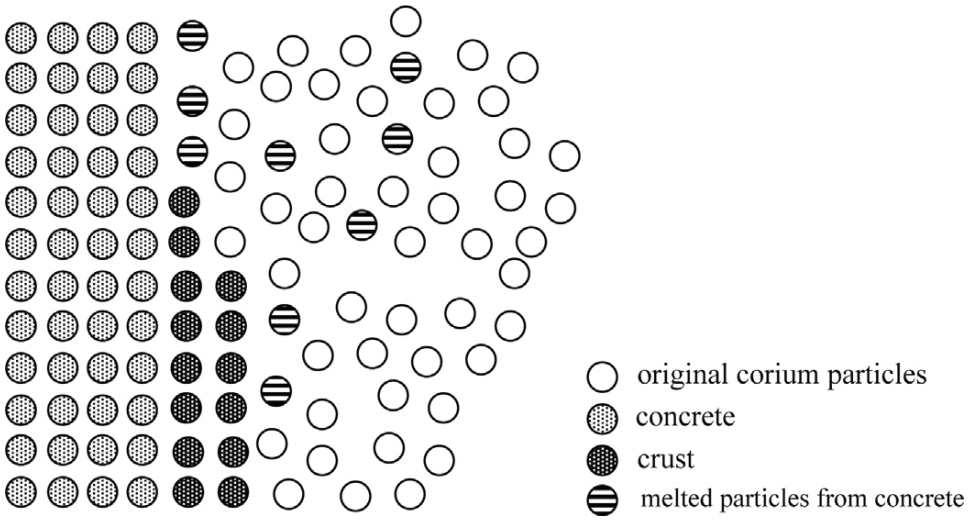

Fig. 1-14 Concept of mixing model 1 (Chai et al., 2015)

Since MCCI experiments have suggested that molten concrete does not immediately and completely mix into corium, another mixing model was developed to consider the real situation of diffion process of concrete into corium. In this model, each particle is composed of both corium and concrete; a particle can be assumed to have two barrels (see Fig. 1-15). For the concrete particles, the concrete barrel is 100% full and the corium barrel is empty. The materials in the barrels will be transferred to each other according to the following mass diffusion equation (Chai et al., 2015):

$$\frac{\partial m}{\partial t} = D\nabla^2 m \tag{1-12}$$

where m is the mass and D is the diffusion coefficient of the material.

Simulations with mixing model 1 and model 2 were performed on CCI-2 test, respectively. The simulated and experimental basemat (bottom) and sidewall ablation depths with elapsed time were shown in Fig. 1-16. As can be seen from the figure, for sidewall ablation, Case 3 with mixing model 2 well reproduced the experimental data, while Case 2 with mixing model 1 underestimated the abaltion depth in general. For basemat (bottom) ablation, both cases underestimated the ablation depth comparing to experimental data. This suggested that more significant sidewall concrete abaltion was predicted in the simulation which as a result presented an anisotropic abaltion pattern as shown in Fig. 1-17. However, this controdicted with the experimental observation of CCI-2 test that the final concrete cavity was isotropic and the consensus from other experimtnal observation that isotropic ablation pattern should be expected when MCCI happens in limestone-rich concrete with protypic oxidic corium. This indicats that the mixing models cannot well explain the mechanism of isotropic abaltion pattern.

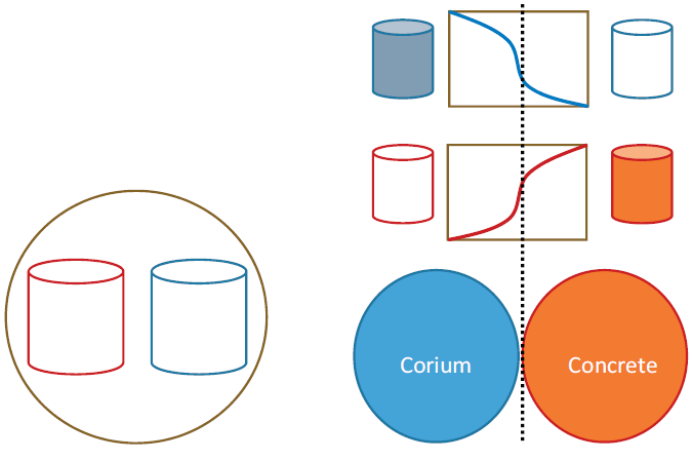

Fig. 1-15 Concept of mixing model 2 (Chai et al, 2015)

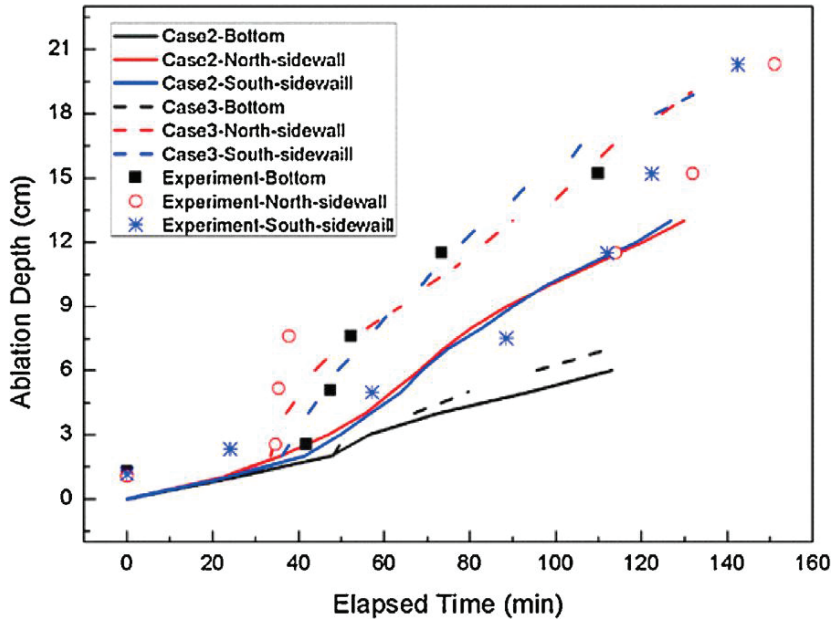

Fig. 1-16 Concrete ablation depths for mixing model 1 (Case 2) and 2 (Case 3) (Chai et al, 2015)

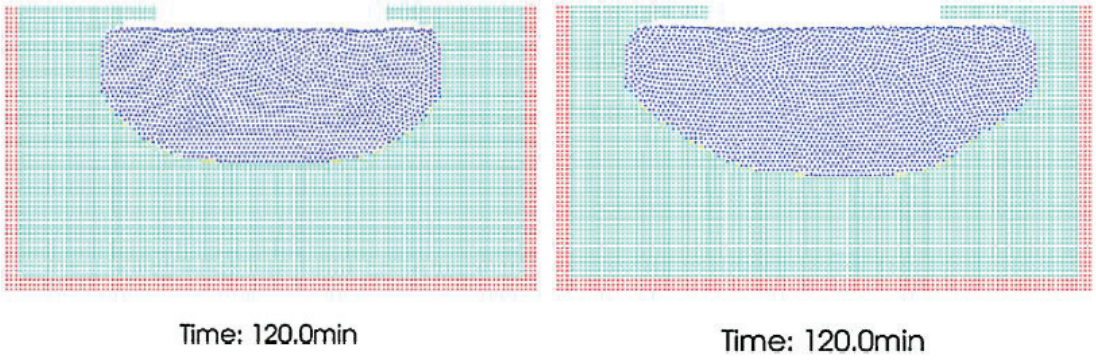

Fig. 1-17 Concrete cavities of Case 2 (left) and Case 3 (right) (Chai et al, 2015)

1.5.3 Remaining issues

Although there have been past successful research efforts on MCCI analysis by MPS method, the inadequacies can be easily identified and there are still remaining issues left unresolved, which mainly lies in the following three aspects.

- The validations of MPS method were performed on only 1-D test SWISS-2 with only metal corium and 2-D test CCI-2. It is necessary to validate MPS method against more multi-dimensional MCCI experiments in a comprehensive manner, in order to investigate the mechanism of important phenomenology in MCCI with prototypic corium materials and different types of concrete.

- Although previous MPS simulations has proved the capability of MPS method for MCCI analysis, the deviations of MPS simulation results from the experimental measurements can be seen from previous study. This indicates that improvements are needed to implement on current MPS method in order to achieve more precise prediction.
- The mechanism of isotropic and anisotropic ablation pattern in limestone-rich and siliceous concrete has not yet been investigated and well understood. Especially, no study has been carried out on anisotropic ablation pattern in siliceous concrete by MPS method. Thus, this knowledge gap should be filled.

Above all, this suggests a necessity to improve MPS method for more accurate multi-dimensional MCCI analysis and to understand the mechanism of MCCI from a more fundamental perspective.

1.6 Objectives of current study

Hence, the main objectives of current study are as follows:

(1) To further validate the capability of MPS method for MCCI analysis and improve the accuracy of its predictions.

(2) To identify the important influential factors of MCCI and reveal its mechanism from a more mechanistic and fundamental perspective by an improved multi-dimensional MPS method.

In this study, a step-by-step approach of code validation was applied and presented in this thesis. First, a brief introduction of the improved MPS method with additional and originally developed models is presented. Then, the heat conduction, chemical reaction heat and phase change models were validated with 1-D MCCI experiments SURC-2 and SURC-4 Then the slag film, crust dissolution models, and the anisotropic ablation mechanism were validated with 2-D MCCI experiments CCI-2 and CCI-3. Finally, the MPS code was applied to 3-D simulations of MCCI experiments VULCANO VB-U7 and COMET-L3 to validate the overall feasibility of multi-dimensional MPS code for

MCCI simulation and analysis. This thesis follows the above research logic and is presented in this logic order.

1.7 Originality of current study

MCCI is primarily governed by the basic thermal-hydraulics (heat transfer and convection) and phase change of the corium and concrete. The difficulties of understanding and accurately predicting MCCI is due to further influences and interactions of local phenomena, such as crust formation, crust dissolution, slag film formation (gas generation), and relocation of thermally stable aggregates. The past simulation method was not capable of identifying the influential factors on MCCI nor able to reveal complex interactions of these influential factors, because empirical correlations were extensively used in the basic thermal-hydraulics and phase change models. An example of such difficulty can be clearly seen when classical simulation codes fail to predict isotropic/anisotropic ablation of concrete by oxidic corium without adjustment of empirical parameters used in evaluation of the corium-concrete interface heat flux.

The MPS method used in this study is capable of mechanistic modeling of the basic thermal-hydraulics and phase change involved during MCCI. In this study, the MPS method is further developed and applied to multi-dimensional MCCI experiments (from 1-D to 3-D) systematically. This approach has succeeded in attaining a major breakthrough in understanding and predicting MCCI. That is, the influential factors of MCCI and their complex interactions have been understood mechanistically for the first time in the research of MCCI. The different mechanisms that distinguish isotropic and anisotropic ablations have been understood mechanistically with discussions on contributions of different models corresponding to the influential factor, rather than adjustment of the basic thermal-hydraulic models. The originality of current study is reflected on the following three aspects.

- This study has succeeded in identifying the influential factors and revealing the

complex interactions of these factors for the first time in the research of MCCI by using and developing the MPS method and applying the method to multi-dimensional MCCI experiments (from 1-D to 3-D) systematically. The past simulation method was neither capable of identifying the influential factors on MCCI nor able to reveal complex interactions of these influential factors since empirical correlations were generally used to model heat transfer, convection and phase change involved during MCCI. Thus, the past simulations could only provide empirical explanations for the observed MCCI phenomena. The MPS method used in this study is capable of mechanistic modeling of heat transfer, convection and phase change involved during MCCI, which provides superiority over past simulation method on modeling and clarifying the fundamental mechanism of MCCI.

- The mechanisms that characterize anisotropic ablation of siliceous concrete and isotropic ablation of limestone concrete by oxidic corium is discussed for the first time in the research of MCCI, which is particularly important for understanding and improving safety of nuclear reactors during severe accidents. In particular, the influence of thermally stable silica aggregates, which are the main composition of siliceous concrete, on anisotropic ablation of siliceous concrete by oxidic corium has been modeled and studied for the first time, which can facilitate the understanding of the characteristics of MCCI with siliceous concrete by oxidic corium.

The different characteristics of siliceous and limestone concrete and corresponding models that should be considered when simulating MCCI have been addressed and concluded originally from best estimation of multi-dimensional MCCI experiments. To consider the characteristics of siliceous and limestone concrete in different manners can facilitate precise modeling of MCCI by highlighting the main issues without sacrificing the accuracy of modeling.

1.8 Target accuracy of MCCI study with MPS simulations

The ultimate target accuracy of MCCI study with MPS simulations is to provide highly accurate predictions to improve the safety of nuclear power reactors by meeting accident management requirement and the corresponding safety evaluation for licensing. Although currently research efforts are still needed to realize this ultimate goal, the preliminary goal of the target accuracy can be described as flows:

1. One of the most important issues in MCCI is how much concrete can be ablated in a certain amount of time. To be more specific, from the viewpoint of accident management, the primary concern of MCCI is how much time MCCI may take to reach the containment liner before water injection, i.e., dry cavity ablation behavior. According to TEPCO's evaluation on MCCI in Fukushima Units 1-3 (TEPCO, 2015), the details of MCCI at Fukushima Units 1-3 are still not fully understood. In the case of BWR-3 Mark-1 containment for Fukushima Units 1-3, anisotropy in the ablation may lead to significant difference in the time required to fail the containment liner. Thus, under severe accident condition, it would be of great significance if the predicted liner failure would differ by the time scale of hours as the results of dry cavity isotropy/anisotropy in the ablation pattern, which gives us the necessity to investigate and identify the mechanism of isotropic and anisotropic ablation patterns in MCCI.
2. The current study, aiming at mechanistic modeling of MCCI to predict isotropic and anisotropic ablation by MCCI, may be the first step to evaluate such significance in the accident management.
3. In reality and in more advanced safety evaluation, the liner failure timing should be evaluated with consideration of water injection. Improving accuracy (by a timescale of hours) under such conditions may be the second goal.
4. Such accuracy evaluation would be relevant not only to Mark-1 containment, but also different types of reactor containment with different concrete composition and debris compositions. Although the current study focuses on some representative siliceous

and limestone concrete ablation with oxidic corium, capability of accurate predictions with various designs and conditions may also need to be studied.

5. A specific necessity can also be identified for BWR Mark-1 containment regarding sump ablation. Anisotropic ablation in the sump pit may lead to undercutting the pedestal wall, which may lead to collapse of the pedestal wall. Such collapse does not seem to have happened in Fukushima. However, strength of the containment floor supporting the pedestal wall may have weakened, which may need attention during debris removal.

Chapter 2 MPS method and developed models

2.1 MPS method

In order to solve problems in fluid mechanics with numerical simulations, the governing equations are established based on conservation laws, which include mass, momentum and energy conservation equations stating that these important variables should be conserved with time evolution within the computational domain of interest. Since it is very difficult to obtain analytical solutions from governing equations which are usually partial differential equations (PDE), the techniques of discretization are needed for the differential operators and domain so that these PDEs can be solved to obtain numerical values such as density, pressure, and velocity at discrete points regarding time and space.

There are two fundamental frames of coordinate to describe the governing equations of fluid mechanics: the Eulerian description and the Lagrangian description. The Eulerian description fixes the coordinates in space, while the Lagrangian description keeps track of the locations of individual fluid particles. Within these two frames, there are namely two types of space discretization techniques, namely meshed based methods such as Finite Element Method (FEM) or Finite Difference Method (FDN) and mesh free methods such as Smoothed particle hydrodynamics (SPH). MPS method is a type of particle method. Compared with mesh based methods, the problems of large deformation, tracking free surface, and adapt the changes of the topological structures can be easily solved.

The fundamental idea of MPS method is to discretize a continuum with particles. The differential operators in the mass, momentum and energy conservation equations are discretized with particle interaction models. The detailed descriptions of basic MPS method are described in the following sections.

2.1.1 Governing equations

The mass conservation (continuity) equation can be written as:

$$\frac{D\rho}{Dt} + \rho\nabla \cdot \mathbf{u} = 0 \tag{2-1}$$

For incompressible fluids, Eq. 2-1 can be rewritten as:

$$\frac{D\rho}{Dt} = 0 \tag{2-2}$$

Combining Eq. 2-1 and Eq. 2-2, we can get the incompressible condition as:

$$\nabla \cdot \mathbf{u} = 0 \tag{2-3}$$

Eq. 2-3 is used when solving pressure from Navier-Stokes equation, which will be described in detail in the later sections.

The Navier-Stokes equation can be written as:

$$\rho\frac{D\mathbf{u}}{Dt} = -\nabla P + \mu\nabla^2\mathbf{u} + \mathbf{F} \tag{2-4}$$

where ρ is density, μ is viscosity and **F** is external force. Thus, the terms on the right side of the equation represent gradient term, viscous term, and external force term, such as gravity and surface tension.

2.1.2 Weight function

In MPS method, the interactions between particles are accomplished through weight function. The common kernel function used to discretize the differential operators in MPS method is defined as:

$$w(r) = \begin{cases} \frac{r_e}{r} - 1 & 0 \le r < r_e \\ 0 & r_e \le r \end{cases} \tag{2-5}$$

where r is the distance between two particles i and j, namely, $r=|r_i-r_j|$; r_e is the effective particle interaction radius which defines the interaction range of particle i with its

neighboring particles. Eq.2-6 indicates that the effect of interaction between particles i and j decreases with the increase of their distance r and equals to zero when r is larger than r_e as shown in Fig.2-1. It also suggests that the value of Eq.2-6 tends to infinity when r approaches 0, which can prevent two particles from bumping into each other and thus guarantee the numerical stability of the incompressible calculations.

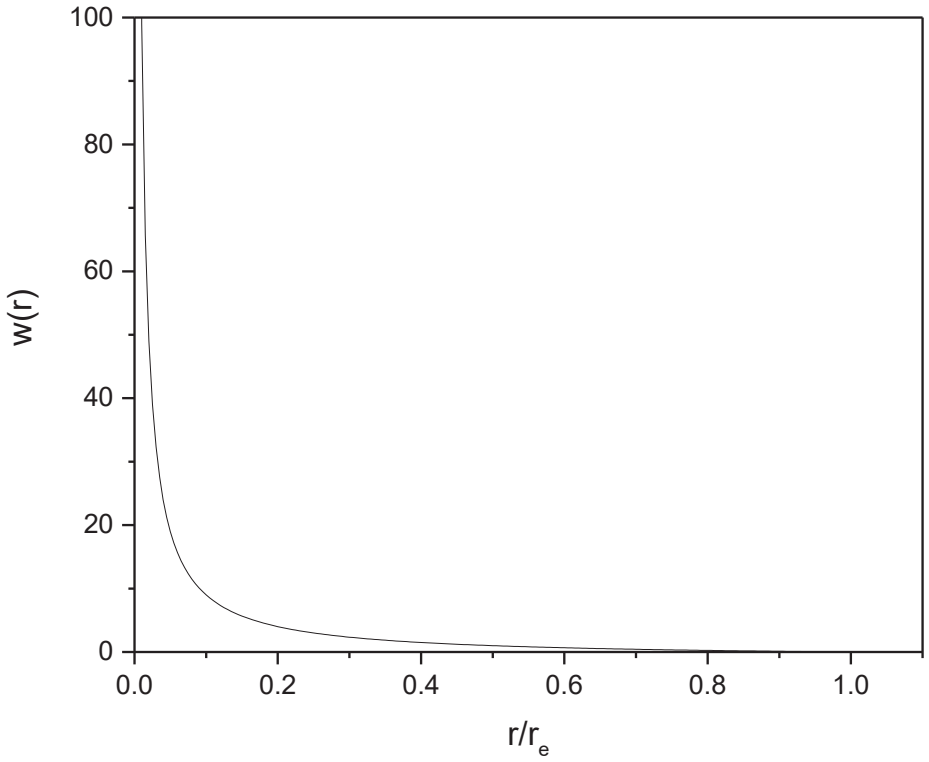

Fig. 2-1 Weight function

2.1.3 Particle number density

In MPS method, particle number density is used when calculating the density of the fluid and defined as the summation of weight function as:

$$n_i = \sum_{j \neq i} w(|\mathbf{r}_j - \mathbf{r}_i|) \tag{2-6}$$

Assuming that the mass of one particle is m and there are N particles in unit volume V, the density of the fluid can be then calculated as:

$$\rho = \frac{mN}{V} \tag{2-7}$$

Approximating N as particle number density and V as the integral of kernel function,

the density then can then be approximately represented as:

$$\rho = \frac{mN}{V} \cong \frac{mn}{\int w dv} \tag{2-8}$$

When effective particle interaction radius r_e is determined, $\int w dv$ is a constant value. Meanwhile m is also constant for a specific case. Thus, one can easily conclude that the density ρ is only dependent on and proportional to the particle number density n. Under this condition, for incompressible fluid, the particle number density remains constant as n^0, which can be expressed as:

$$n^0 = \sum_{j \neq i} w(\left|\mathbf{r}_j^0 - \mathbf{r}_i^0\right|) \tag{2-9}$$

2.1.4 Gradient model

Considering two neighboring particles i, j, $\phi_i = \phi(\mathbf{r}_i)$, and $\phi_j = \phi(\mathbf{r}_j)$, ϕ_i and ϕ_j indicate the scalar variables at position vectors $\mathbf{r}_i$ and $\mathbf{r}_j$. With Taylor expansion, scalar ϕ_j can be expressed as:

$$\phi_j = \phi_i + \nabla \phi|_i \bullet (\mathbf{r}_j - \mathbf{r}_i) + \ldots \tag{2-10}$$

Considering only the first order Taylor expansion and $\nabla \phi|_{ij}$ the gradient vector between particles i and j, the following equation can be obtained:

$$\nabla \phi|_{ij} \bullet (\mathbf{r}_j - \mathbf{r}_i) = \phi_j - \phi_i \tag{2-11}$$

If the both sides of Eq. 2-11 are multiplied by $\frac{(\mathbf{r}_j - \mathbf{r}_i)}{\left|\mathbf{r}_j - \mathbf{r}_i\right|^2}$, the following equation can be obtained (see Fig. 2-2):

$$\nabla \phi|_{ij} = (\phi_j - \phi_i) \frac{(\mathbf{r}_j - \mathbf{r}_i)}{\left|\mathbf{r}_j - \mathbf{r}_i\right|^2} \tag{2-12}$$

Introducing weight function to normalize the gradient, the gradient model then can be obtained as:

$$\langle \nabla \phi \rangle_i = \frac{d}{n^0} \sum_{j \neq i} \left[\frac{\phi_j - \phi_i}{|\mathbf{r}_j - \mathbf{r}_i|^2} (\mathbf{r}_j - \mathbf{r}_i) w(|\mathbf{r}_j - \mathbf{r}_i|) \right] \tag{2-13}$$

where d is the number for dimensions, namely d is equal to 2 or 3 for 2 dimensional or 3 dimensional simulation, w is weight function and n^0 is particle density number. Gradient model is used to solve the pressure in Poison equation which will be described in detail later in Section 2.3.

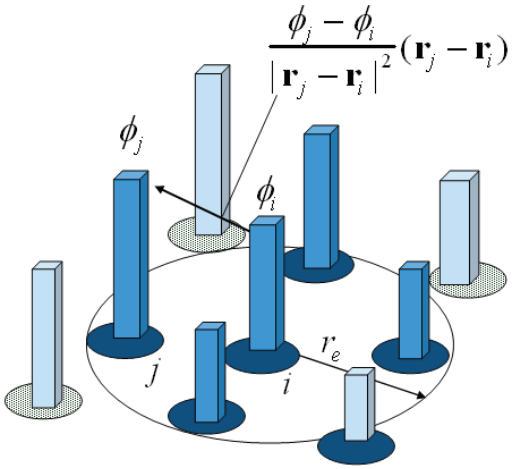

Fig. 2-2 Illustration for gradient model

2.1.5 Laplacian model

The Laplacian model which is used to express the physical meaning of diffusion is defined as:

$$\langle \nabla^2 \phi \rangle_i = \frac{2d}{\lambda n^0} \sum_{j \neq i} \left[(\phi_j - \phi_i) w(|\mathbf{r}_j - \mathbf{r}_i|) \right] \tag{2-14}$$

where λ is defined as $\lambda = \frac{\sum_{j \neq i} \left[|\mathbf{r}_j - \mathbf{r}_i|^2 w(|\mathbf{r}_j - \mathbf{r}_i|) \right]}{\sum_{j \neq i} w(|\mathbf{r}_j - \mathbf{r}_i|)}$ (see Fig. 2-3).

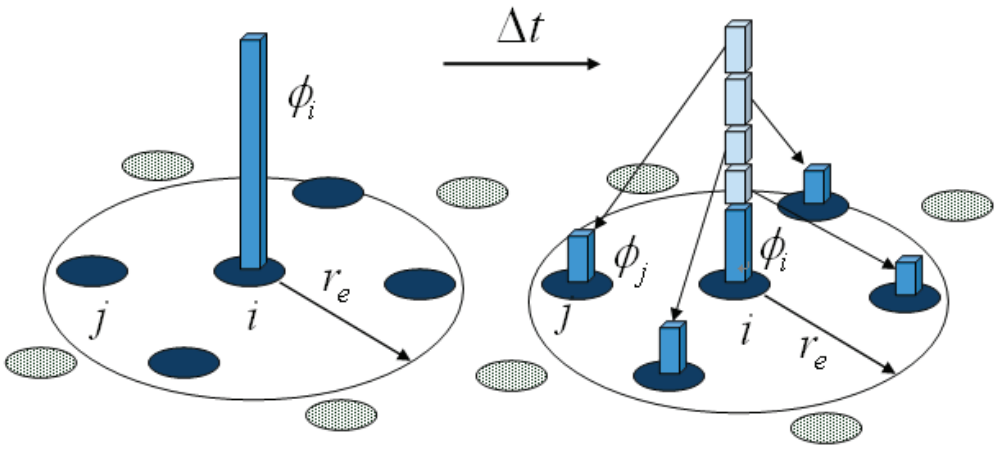

Fig. 2-3 Illustration for Laplacian model

2.1.6 Divergence model

The divergence model which is used to calculate the divergence of a vector variable **u** can be expressed as:

$$\left\langle \nabla \cdot \mathbf{u} \right\rangle_i = \frac{d}{n^0} \sum_{j \neq i} \left[\frac{(\mathbf{u}_j - \mathbf{u}_i) \cdot (\mathbf{r}_j - \mathbf{r}_i)}{\left| \mathbf{r}_j - \mathbf{r}_i \right|^2} w(\left| \mathbf{r}_j - \mathbf{r}_i \right|) \right] \tag{2-15}$$

The divergence model is used as the source term of Poison equation.

2.2 Additional models

For MCCI analysis using MPS method, it is necessary to develop and introduce several additional models in order to study the important phenomena in MCCI. The heat conduction and phase change models were introduced in the basic MPS code "MPS-SW-MAIN-Ver.2"* to realize temperature and phase change calculation. Besides heat conduction and phase change models, four additional original models have been developed specially for MCCI calculation, namely chemical reaction heat model, corium viscosity model, slag film heat transfer model and crust dissolution model. Chemical reaction heat model is to consider the chemical heat introduced in melt pool by metal oxidation. Corium viscosity model is to consider temperature dependence of

* MPS-SW-MAIN-Ver.2.0, P 第 8827 号-1, 2006.2.23（内容：粒子法流体解析プログラム）

corium viscosity. Slag film model is to consider the heat transfer influence of gas generation from concrete decomposition on corium/concrete interface. Crust dissolution model is to consider the effect of crust dissolution by molten concrete. These models are necessary to capture the main influential factors of MCCI.

2.2.1 Heat conduction model

The energy conservation equation can be expressed as:

$$\frac{DH}{Dt} = k\nabla^2 T + Q \tag{2-16}$$

where H is enthalpy, T is temperature, k is thermal conductivity and Q is heat source. Consider a linear function between temperature T and enthalpy H, then:

$$H(T) = \rho C_p (T - T_0) + H_0 \tag{2-17}$$

where C_p is specific heat, H_0 and T_0 are reference enthalpy and temperature, respectively. Substitute Eq. 2-17 into Eq. 2-16, then Eq. 2-16 can be written as:

$$\frac{DT}{Dt} = \frac{k}{\rho C_p}\nabla^2 T + \frac{Q}{\rho C_p} \tag{2-18}$$

Use Laplacian model in Eq. 2-14, then Eq. 2-18 can be discretized as:

$$T_i^{k+1} = T_i^k + \frac{k\Delta t}{\rho C_p}\frac{2d}{n^0 \lambda}\sum_{j\neq i}(T_j^k - T_i^k) w(\left|\mathbf{r}_j - \mathbf{r}_i\right|) + \frac{Q}{\rho C_p} \tag{2-19}$$

where k is determined based on the heat conduction law between two particles. Consider two particles i and j as shown in Fig.2-4, T_c is the center temperature of these two particles, then heat flux q'' can be calculated as:

$$q'' = k_i \frac{dT}{dx} = k_i \frac{T_i - T_c}{\frac{l}{2}} \tag{2-20}$$

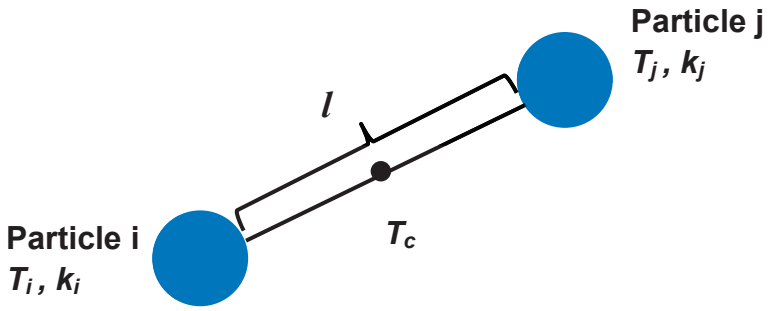

Fig. 2-4 Illustration of heat conduction between two particles in MPS method

$$q'' = k_j \frac{dT}{dx} = k_j \frac{T_i - T_c}{\frac{l}{2}}$$

(2-21)

Combining Eqs. 2-20 and 2-21, we can get:

$$k_i \frac{T_i - T_c}{\frac{l}{2}} = k_j \frac{T_i - T_c}{\frac{l}{2}} \tag{2-22}$$

The center temperature T_c between particles i and j can be written as:

$$T_c = \frac{k_i T_i + k_j T_j}{k_i + k_j} \tag{2-23}$$

Substitute Eq.2-23 into Eq.2-20, then:

$$q'' = \frac{2k_i k_j}{k_i + k_j} \frac{T_i - T_j}{l} \tag{2-24}$$

Thus, thermal conductivity k should be:

$$k = \frac{2k_i k_j}{k_i + k_j} \tag{2-25}$$

Eq.2-19 can then be expressed as:

$$T_i^{k+1} = T_i^k + \frac{\Delta t}{\rho C_p} \frac{2d}{n^0 \lambda} \sum_{j \neq i} \frac{2k_i k_j}{k_i + k_j} (T_j^k - T_i^k) w_{ij} + \frac{Q}{\rho C_p} \tag{2-26}$$

2.2.2 Phase change model

Melting and solidification processes of materials are one of the main concerns during MCCI. Phase transition is modeled with respect to the state of change of each particle in MPS method. Each particle is characterized by temperature T, enthalpy H and solid fraction γ. The temperature of the particle is calculated as a function of enthalpy, which is:

$$T=\begin{cases} T_s+\dfrac{H-H_{s0}}{\rho C_{ps}} & H<H_{s0} \\ T_s+\dfrac{T_l-T_s}{H_{sl}-H_{s0}}\left(H-H_{s0}\right) & H_{s0}\le H\le H_{sl} \\ T_l+\dfrac{H-H_{sl}}{\rho C_{pl}} & H_{sl}<H \end{cases} \tag{2-27}$$

The solid fraction of the particle is defined as:

$$\gamma=\begin{cases} 1 & H<H_{s0} \\ \dfrac{H_{sl}-H}{H_{sl}-H_{s0}} & H_{s0}\le H\le H_{sl} \\ 0 & H_{sl}<H \end{cases} \tag{2-28}$$

When γ= 0, the particle is in a completely fluid state; when γ=1, the particle is in a completely solid state; when 0<γ<1, the particle is in a partially fluid and partially solid state. Analysis of melt spreading experiments for stainless steel SPREAD suggested that about 55% of heat of fusion needs to be removed from the melt (i.e. containing 55% solid fraction) to stop the spreading process (Dinh et al., 2000). This indicated that a critical value of solid faction is important to determine the threshold at which the behavior of materials changes from the fluid to solid.

2.2.3 Original models developed for MCCI calculation

In Section 2.2.3, several original models specially developed for MCCI calculation are introduced, including chemical reaction model, corium viscosity model, slag film

model and crust dissolution model. Each model focuses on different aspects of MCCI and facilitates more accurate simulation with MPS method.

2.2.3.1 Chemical reaction heat model

When the molten materials from the reactor core are released into the cavity, several chemical reactions might happen within the melt pool, which can provide another heat source resulting from chemical reaction heat besides decay heat from the fission products. The main exothermic chemical reactions that can happen are the oxidation of metals such as Zr, Fe or Cr with the gas or water from the decomposition of concrete. It should be noted that the oxidation of Fe by H_2O and CO_2 are endothermic chemical reactions. The chemical reaction heat required by endothermic chemical reactions when concrete decomposes, such as decomposition of $CaCO_3$, has not been particularly included in the chemical reaction heat model. This amount of heat has already been considered in the decomposition enthalpy of concrete when calculating the phase change of concrete. The chemical reactions that are considered to happen are as follows:

$$Zr + 2H_2O = ZrO_2 + 2H_2 + 701kJ/mol \quad Zr \tag{2-29}$$

$$Zr + 2SiO_2 = ZrO_2 + 2Si + 190kJ/mol \quad Zr \tag{2-30}$$

$$Si + 2H_2O = SiO_2 + 2H_2 + 500kJ/mol \quad Si \tag{2-31}$$

$$Si + 2CO_2 = SiO_2 + 2CO + 424kJ/mol \quad Si \tag{2-32}$$

$$2Cr + 3H_2O = Cr_2O_3 + 3H_2 + 187kJ/mol \quad Cr \tag{2-33}$$

$$2Cr + 3CO_2 = Cr_2O_3 + 3CO + 146kJ/mol \quad Cr \tag{2-34}$$

$$Fe + H_2O + 168J/mol \quad Fe = FeO + H_2 \tag{2-35}$$

$$Fe + CO_2 + 27J/mol \quad Fe = FeO + CO \tag{2-36}$$

The total amount of chemical reaction heat is calculated from the mass of reference elements in Eqs. 2-29 to 2-36. Then the chemical heat is considered distributed evenly throughout the melt pool applying to every melt particle as a chemical heat source $Q_{chemical}$ in energy conservation equation 2-16, which can be expressed as:

$$\frac{DH}{Dt} = k\nabla^2 T + Q_{decay} + Q_{chemical} \tag{2-37}$$

2.2.3.2 Corium viscosity model

The viscosity of molten corium and concrete mixture is an important parameter to predict its rheological behavior during MCCI. Since the viscosity of molten corium and concrete mixture has strong dependence on temperature, especially between the solidus and liquidus temperature of corium, a temperature dependent model is used in current MPS code. In real situation, the viscosity of the corium and concrete mixture can also be related to the change of composition. However, for oxidic corium concrete mixture, the influence of temperature change is more significant than that of the composition change (Penttilä, 2012). Thus, in current study, the fitting correlations of viscosity from the experimental measurements of viscosity of corium with 27.5 weight-% concrete Epstein (1998) were used as the representative corium-concrete mixture viscosity. The correlations are as follows:

$$\mu = \begin{cases} 5.187 \cdot 10^{-17} \cdot \mathrm{e}^{\,82230/\mathrm{T}}, & 2000\mathrm{K} < \mathrm{T} < 2284\mathrm{K} \\ 1.275 \cdot 10^{-5} \cdot \mathrm{e}^{\,22200/\mathrm{T}}, & 2284\mathrm{K} \le \mathrm{T} < 2600\mathrm{K} \end{cases} \tag{2-38}$$

In this paper, this viscosity model is used to estimate the corium with 15 weight-% siliceous concrete and 8 weight-% limestone concrete. The viscosities for over 2600K and less than 2000K were deemed as constant values calculated from the above

correlations at the 2000K and 2600K.

2.2.3.3 Slag film heat transfer model

As shown in Fig.2-5, the slag film is assumed to be a thin film that can form on the corium-concrete interface due to concrete ablation and decomposition gas generation from the concrete during MCCI. The thermal resistance of this slag film can be influenced by decomposition gas bubbles on the interface generated from concrete between the melt pool and the bulk concrete. Mechanistic calculation of the slag film with MPS may be possible. However, the required calculation resolution may be too high to simulate interactions of this influential factor with other influential factors to understand mechanism of MCCI. Hence, for the purpose of the current study, slag film is modeled with empirical correlation. In order to introduce the effects of agitated gas generation from limestone concrete on thermal resistance of the slag film, the slag film model which was modified by Bradley (Bradley, 1988) from the bubble agitation heat transfer model of Kutateladze and Malenkov (Kutateladze and Malenkov, 1978) has been implemented.

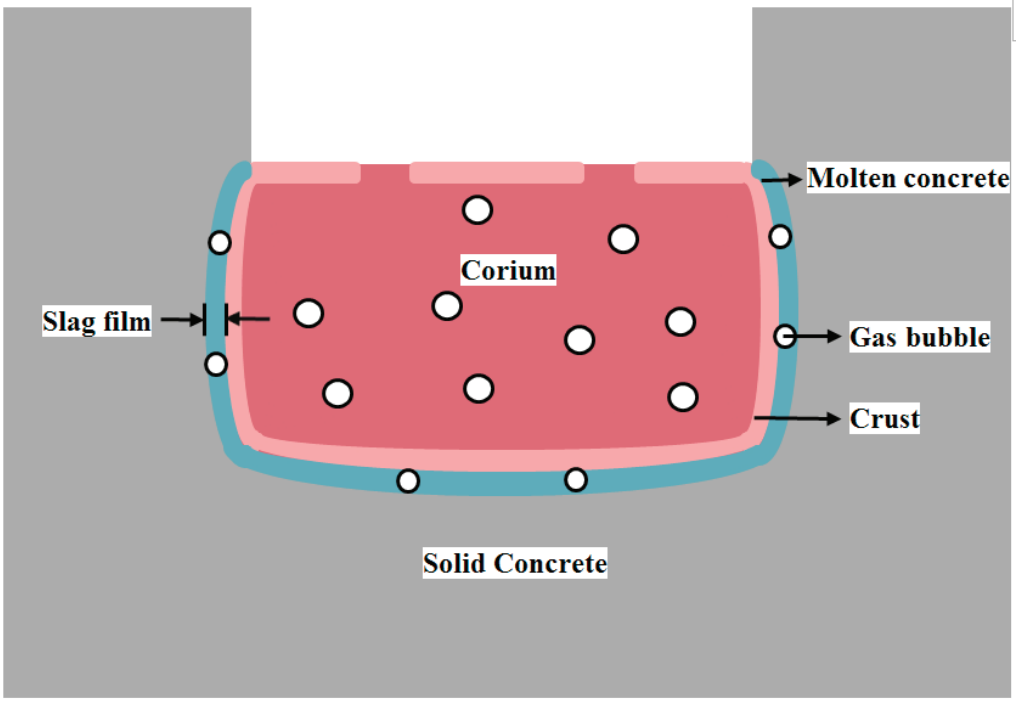

Fig. 2-5 Illustration of the configuration of the melt pool during MCCI

The heat flux at the bottom of the melt pool can be expressed as:

$$q_b = h_b(T_m - T_{dc}) \tag{2-39}$$

The heat transfer coefficient could be written as:

$$h_b = \begin{cases} C_\beta^3 C_\xi^2 (T_m - T_{dc})^2; & j < j_{tr} \\ C_\beta^{6/5} C_\xi^{1/5} j_{tr}^{3/5} (T_m - T_{dc})^{1/5}; & j \geq j_{tr} \end{cases}, \tag{2-40}$$

where:

$$C_\beta = 1.5 \cdot 10^{-3} C_{slag} \left(\frac{c_m P}{k_m g} \right)^{2/3} \frac{k_m}{L_\lambda} \tag{2-41}$$

$$C_\xi = \frac{\chi_g}{\rho_g e_d} \tag{2-42}$$

and the expression $j = \left[C_\beta C_\xi (T_m - T_l) \right]^3$ is used to determine if the superficial gas velocity j lies above or below the transition velocity $j_{tr} = 4.3 \cdot 10^{-4} \sigma_m / \mu_m$. In this study, the heat transfer coefficient calculated from Eq. 2-40 is applied to the corium and concrete particles on the corium-concrete interface when the concrete temperature exceeded the evaporation temperature of free water 373K.

The applicable range of slag film heat transfer model can be determined from the original experimental study carried out by Kutateladze and Malenkov (Kutateladze and Malenkov, 1978) on bubble agitation heat transfer. The experiments were carried out with bubbling of hydrogen, helium, nitrogen and argon at pressures from 1 to 40 abs atm into water and water-glycerin solutions through a micro-porous surface (porous rates 0.13, 0.2 and 0.44). The experiment was carried out at 5℃when the developed nucleate bubbling region was least extended. As can be seen from the experimental parameters and conditions, the applicable range of the correlation is subject to the pressure from 1 to 40 abs atm and capillary number $Ca = \frac{j\mu}{\sigma}$ ranging from 10^{-3} to 0.1. In current study, the pressure is usually around 1 abs atm and the typical capillary

number of corium ranges from 10^{-3} to 5×10^{-3}, which falls within the applicable range of slag film model. Meanwhile, the applicable range of temperature required in the correlations of slag film model might need further clarification. It is required that corium should be in the liquid phase, which corresponds to above 2150 K for the corium used in CCI-2 simulation of current study.

In current study, slag film model was applied to the simulation of MCCI tests carried out with limestone-rich concrete. In MPS method, the slag film model was applied in the following way. When corium is in direct contact with concrete, which is defined as when a concrete particle is within the radius of twice particle size away from a corium particle (see Fig. 2-6), the heat transfer coefficient h_b calculated from Equ.2-40 was used instead of the thermal conductivities of corium and concrete. It should be noted that this modification of thermal conductivity only applies to corium and concrete particles. For crust and molten concrete particles, their thermal conductivities still remain their original values regardless of their relative distance from the corium particles. Also, the interaction radius has been chosen as two times of particle size in current study, assuming that the slag film model will only be effective when there is no thick crust formed between corium and concrete. This tentative selection of interaction radius has been made based on the fact that thick crust is impermeable and can diminish the bubble agitation effect in the slag film, and can therefore compromise the effectiveness of slag film model. However, sensitivity studies with different interaction radius considered in the slag film model might still need to be conducted in the future work.

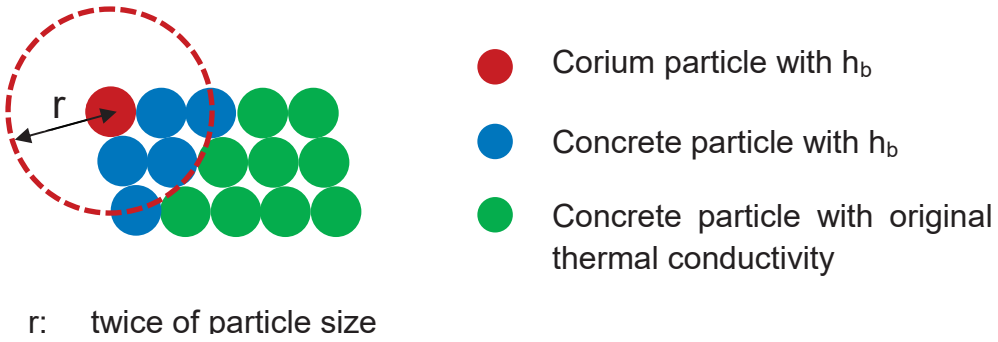

Fig. 2-6 Illustration of slag film model application in MPS method

2.2.3.4 Crust dissolution model

When concrete is ablated by corium, crust could form on the interface between the melt pool and concrete. The crust of high temperature could continue to ablate the cold concrete and lead to molten concrete accumulation beneath it. Under this circumstance, a crust dissolution process induced by compositional convection could start since the thermal and compositional fields at the interface will be unstable. Journeau first proposed the crust dissolution model and used it for numerical analysis of VULCANO B-U5 and U6. A brief introduction of this crust dissolution model will be given thereinafter and the readers can refer to reference authored by Carenini et al. (Carenini et al., 2007) and Kerr (Kerr, 1995) for more specific information.

The conservation of species at the corium-concrete interface could be written as:

$$D\frac{C_m - C_i}{h_d} = (C_i - C_0)V \tag{2-43}$$

where D is the diffusion number; V is the dissolution rate of crust; h_d is the thickness of the compositional boundary layer at the surface of concrete; C_m, C_i and C_0 are the concentration of concrete in melt, interface and crust.

Solutal convection will start when the solutal Rayleigh number satisfies the following condition:

$$Ra = \frac{g(\rho_i - \rho_m){h_d}^3}{D\mu_m} \tag{2-44}$$

Combining Eqs. 2-43 and 2-44 and assuming C_m=1 and C_0=0, namely supposing a crust of pure corium over pure concrete melt, the dissolution rate of crust can be expressed as:

$$V_i = \frac{(1-C_i)^{4/3}}{C_i}\left(\frac{g(\rho_0 - \rho_m)D^2}{Ra_c\mu_m}\right)^{1/3} \tag{2-45}$$

According to the calculations of dissolution rates carried by Journeau for VULCANO VB U5 and U6 experiments, for the case with siliceous concrete (VB-U5), a small dissolution rate no higher than 3 cm/s was obtained, while for the case with limestone concrete (VB-U6), the dissolution rate was much higher, ranging from 2 to 12 cm/s. Thus, in this study, the crust dissolution effect was neglected for CCI-3 simulation which utilized siliceous concrete while a dissolution rate which was derived for VB-U6 experiment and expressed as in Eq. 2-46 is used for CCI-2 simulation which utilized limestone concrete.

$$V_i = 8\cdot 10^{-28} e^{0.0289T} \tag{2-46}$$

The time that each crust particle needs to dissolve is roughly estimated by the particle size divided by the dissolution rate at the phase change temperature of corium. Then after this certain amount of dissolution time, the crust particle would turn into a corium particle even if its temperature is below the temperature when phase change of crust to corium occurs.

2.3 Algorithm

In MPS method, a semi-implicit algorithm is employed. The viscosity term and external force term from Eq.2-4 and the temperature from Eq. 2-19 are explicitly calculated, while the pressure gradient term is implicitly calculated. In each time step, the Navier-Stokes equation is first explicitly solved to obtain the temporal velocity **u*** and position **r*** except the pressure gradient term. The temporal velocity **u*** and

position **r*** are calculated as:

$$\mathbf{u}^* = \mathbf{u}^k + \Delta t\left[\nu\nabla^2\mathbf{u} + \mathbf{f}\right]^k \tag{2-47}$$

$$\mathbf{r}^* = \mathbf{r}^k + \Delta t\mathbf{u}^* \tag{2-48}$$

Since the density of fluid can be deemed as constant for impressible fluid and the density of the fluid is proportionate to the particle number density as mentioned previously in Section 2.1.3, in order to maintain the impressibility, the particle number density must be remained constant as n^0 for each time step. Assuming that at time step k+1, the particle number density is n* after the explicit calculation of viscosity term and external force term, then:

$$n^0 = n^{k+1} = n^* + n' \tag{2-49}$$

$$\mathbf{u}^{k+1} = \mathbf{u}^* + \mathbf{u}' \tag{2-50}$$

$$\mathbf{r}^{k+1} = \mathbf{r}^* + \Delta t\mathbf{u}' \tag{2-51}$$

where n' is the correction of particle number density and **u**' is the correction of velocity.

The correction of velocity **u**' is generated by the implicit pressure term in the Navier-Stokes equation, which can be calculated as:

$$\mathbf{u}' = -\frac{\Delta t}{\rho^0}\nabla P^{k+1} \tag{2-52}$$

Considering Eq. 2-1 and using ρ^0 to approximately replace ρ, Eq.2-1 can be rewritten as:

$$\frac{D\rho}{Dt} + \rho^0\nabla\cdot\mathbf{u} = 0 \tag{2-53}$$

Since the density of the fluid is proportionate to the particle number density, Eq. 2-47 can be rewritten as:

$$\frac{1}{n^0}\frac{Dn}{Dt} + \nabla\cdot\mathbf{u} = 0 \tag{2-54}$$

Then the correction of particle number density n' can be related to the correction of the velocity **u**' as:

$$\frac{1}{n^0}\frac{n'}{\Delta t}+\nabla\cdot\mathbf{u}'=0 \tag{2-55}$$

Substituting Eq.2-52 and Eq.2-53 into Eq. 2-55, the following Poison pressure equation can be obtained:

$$\nabla^2 P^{k+1}=-\frac{\rho^0}{\Delta t^2}\frac{n^*-n^0}{n^0} \tag{2-56}$$

The pressure is then calculated implicitly with the above Poison pressure equation deduced from above. Then the new position and velocity of the particles at next time step k+1 are corrected by the pressure gradient as shown in Eqs. 2-57 and 2-58. A calculation flowchart for MPS algorithm is shown in Fig.2-7.

$$\mathbf{u}^{k+1}=\mathbf{u}^*-\frac{\Delta t}{\rho^0}\nabla P^{k+1} \tag{2-57}$$

$$\mathbf{r}^{k+1}=\mathbf{r}^*-\frac{\Delta t^2}{\rho^0}\nabla P^{k+1} \tag{2-58}$$

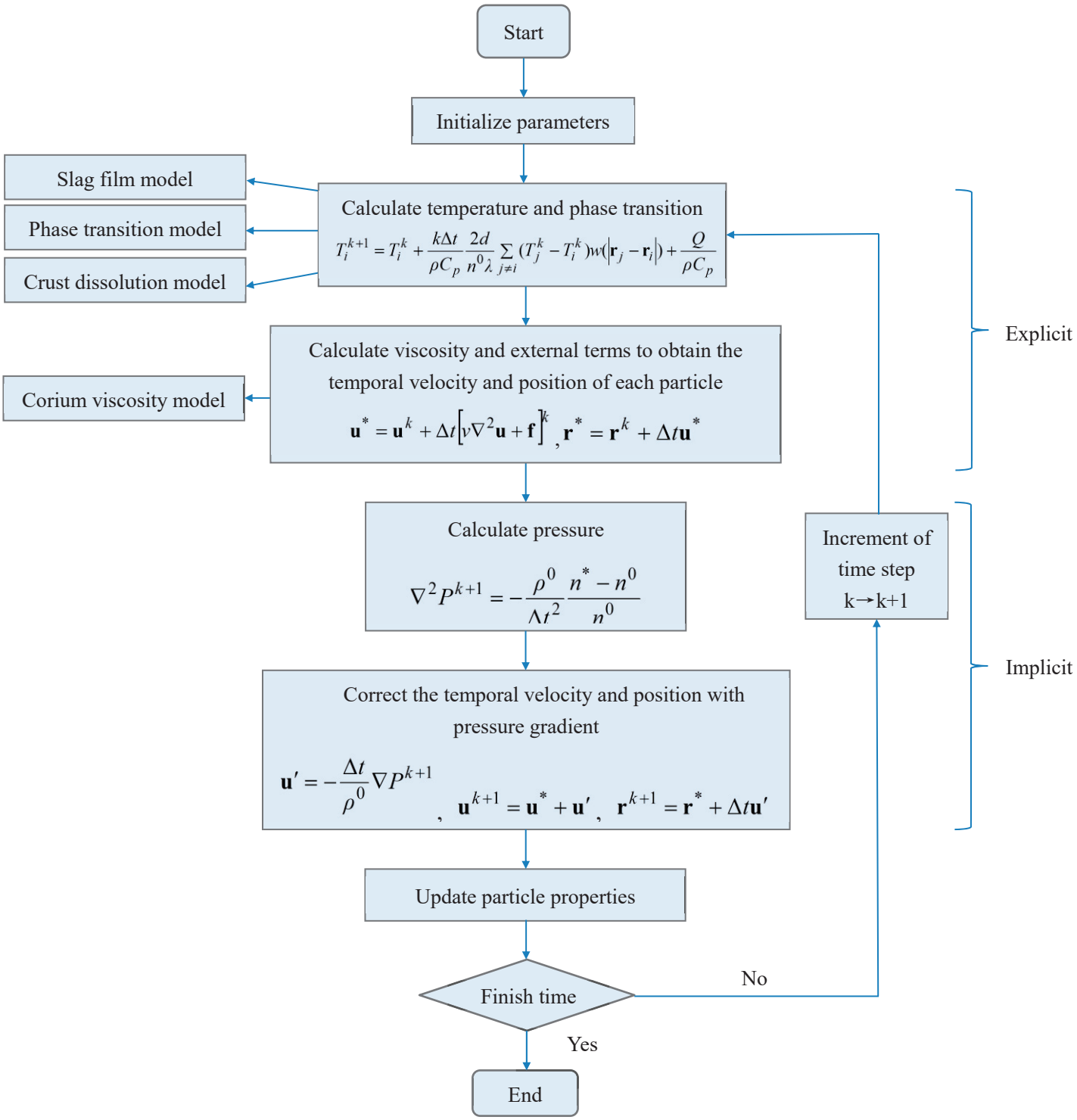

Fig. 2-7 Algorithm of MPS method in current study

2.4 Initial particle configuration and time step criteria

In MPS method, it is necessary to generate different initial particle configurations according to different problems and initial conditions. The main parameters that need to

be determined are particle size, the number of particles, and initial spatial coordinates, velocities and pressure of each particle. Generally, the particles are evenly distributed in space in order to maintain consistency in calculating particle number density. Since the convective and diffusive terms are calculated explicitly in every time step in MPS method, the numerical stability should be guaranteed by choosing an appropriate time step. The stability of convective term can be guaranteed by satisfying Courant-Friedrichs- Lewy (CFL) condition. The Courant number is defined as:

$$C = \frac{\Delta t u_{max}}{l_0} \tag{2-59}$$

where C is Courant number, Δt is time step, u_{max} is the largest absolute value of velocity, l_0 is the particle size. In order to maintain numerical stability, the maximum value of C_{max} is empirically selected as 0.2. Thus, the time step determined by Courant number can be expressed as:

$$\Delta t_{Courant} = \frac{C_{max} l_0}{u_{max}} \tag{2-60}$$

Since the viscous term is also calculated explicitly in this study, the numerical stability of diffusive term should also be guaranteed. The diffusive number is determined as:

$$d = \frac{\Delta t v}{{l_0}^2} \tag{2-61}$$

Thus, the time step determined by diffusive number can be expressed as:

$$\Delta t_{diffusion} = \frac{d_{max} {l_0}^2}{v_{max}} \tag{2-62}$$

Generally, $d_{max} = C_{max}=0.2$ is used for MPS simulations. And the time step is selected as the smaller one determined from Eqs. 2-60 and 2-62. In current study, the preset time step has been chosen as 10^{-3} s, and this value can be maintained for the simulation cases in current study.

2.5 Boundary conditions

2.5.1 Free surface

The free surface is judged by particle number density in MPS method. Since there are no particles configured beyond the free surface, the particle number density of particles on the free surface should be lower than that of the particles within the fluid, as shown in Fig.2-7. Thus, the particles on the free surface can be judged with the following condition:

$$n_i^* < \beta n^0 \tag{2-63}$$

where n_i^* is the particle number density of free surface particles, n^0 is the constant particle number density of a compressible medium. β is an empirical value less than 1.0. Generally, the closer β is to 1.0, the more particles are judged as free surface particles. Empirically, β should be among 0.90 to 0.99 in order to ensure reasonable calculation results. In this study, β is selected as 0.97.

The pressure of the particles judged as free surface particles is set to be 0.0 Pa in the Poisson equation of pressure, namely:

$$P_i^{k+1} = 0 \tag{2-64}$$

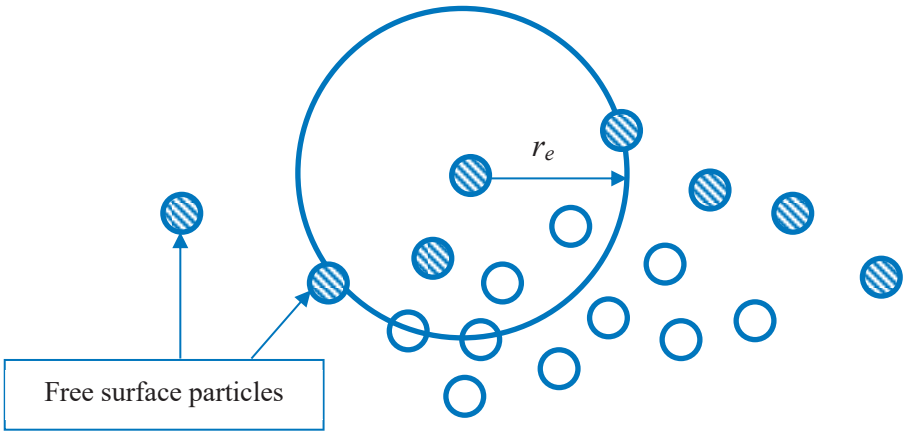

Fig. 2-8 Free surface boundary condition

2.5.2 Wall boundary condition

Wall boundary conditions are represented by wall particles whose coordinates are fixed. There are two types of particles used in current MPS method (see Fig.2-8). The particles that are in direct contact with the fluid particles are called wall particles, of which pressure calculation is performed. The particles that are outside this layer of wall particles are called dummy wall particles, of which pressure calculation is not performed. The main function of the dummy wall particles is to maintain certain particle number density for the wall particles. If there are no dummy wall particles configured outside the wall particles, the wall particles might be judged as free surface particles due to low particle density number. In this sense, the layers of dummy wall particles should be determined. Generally, if the effective of particle interaction radium r_e in weight function is selected as 2.1 times of the initial particle distance l_0, then at least two layers of dummy wall particles are necessary for the geometry in MPS simulation.

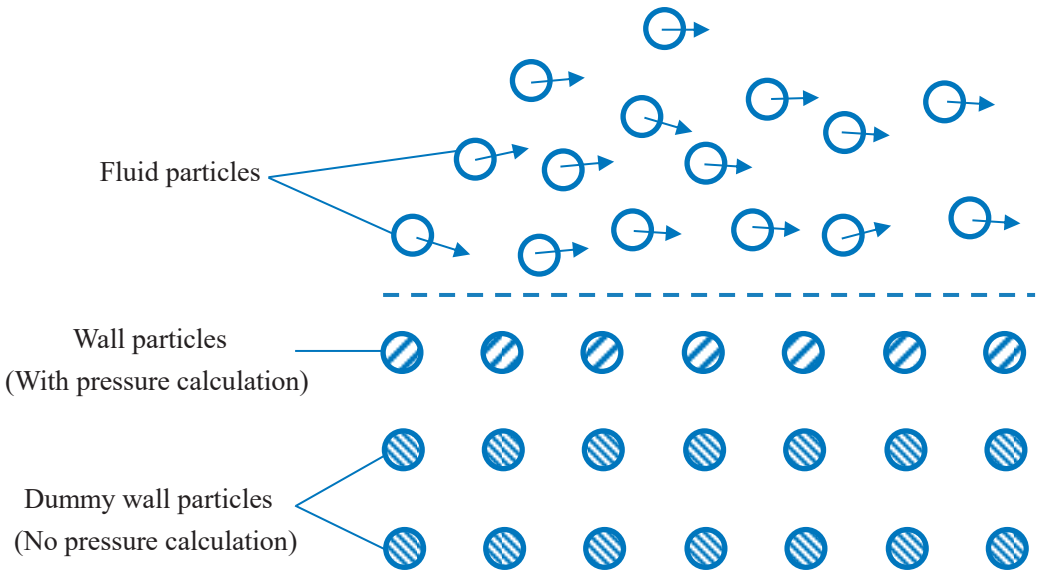

Fig. 2-9 Wall boundary condition

For viscous fluid flows over a solid wall boundary, it is generally acknowledged that no-slip boundary condition should be applied. No-slip boundary condition refers to the condition that the fluid motion relative to the wall boundary will be brought to zero due

to the energy loss through viscosity dissipation. The general requirement of no fluid motion relative to the wall should be that there is neither perpendicular motion nor tangential motion of the fluid relative to the wall. According to the statement and definition raised by Day (Day M.A., 1990), it is suggested that the condition requiring no perpendicular motion is often called the impermeability condition, while the condition requiring no tangential motion is called the no-slip condition (Day M.A., 1990). In MPS method, in which wall particles and dummy wall particles are both employed, generally the velocity of wall and dummy wall particles is set to be zero so that no-slip boundary condition can be retained when the viscosity force is calculated between fluid particles and wall particles.

Chapter 3 Simulations of 1-D MCCI experiments by MPS method

This chapter focuses on the simulations of 1-D MCCI experiments by MPS method with developed models described in the previous chapter. The simulations have been carried out on 1-D MCCI experiments SURC-2 and SURC-4. The research focus is to validate the heat conduction, phase change, and chemical reaction heat models in current improved MPS method. Important parameters during MCCI such as downward concrete ablation front has been studied and compared with experimental measurements. The importance of Zr oxidation and crust formation on the corium/concrete interface has also been investigated.

3.1 Test descriptions of SURC-2 and SURC-4

The SURC-2 and SURC-4 experiments are among the SURC test series carried out by Sandia National Laboratories as part of the Integral Core-Concrete Interactions Experiments Program, which was intended to provide a data base for MCCI with different concretes and melt compositions (Copus et al., 1992). The SURC-2 experiment used prototypic UO_2-ZrO_2 materials of high temperature as melt materials to interact with basaltic concrete, while the SURC-4 experiment used the 304 stainless steel melt with Zr addition to investigate the influence of Zr oxidation on the interaction process. Both tests employed similar experimental apparatus as shown in Fig. 3-1. The primary test section was an interaction crucible comprised of a 40.0 cm diameter basaltic concrete slug surrounded by an MgO annulus. The MgO crucible was 100.0 cm high with an outside diameter of 60.0 cm and an inside diameter of 40.0 cm. The interaction crucible was instrumented with numerous thermocouple arrays cast into the concrete cylinder and MgO annulus to provide temperature measures during the tests. The arrangement of the thermocouples is presented in Fig. 3-2. An induction coil was placed around the crucible to heat and melt the charge within the test article and to sustain the

interaction for the duration of the experiment. Both the MgO crucible and the concrete slug were housed in a sealed, water cooled, aluminum containment vessel. The composition of the melt materials and concrete for SURC-2 and SURC-4 are listed in Tables 3-1, 3-2 and 3-3, respectively. For both tests, after an initial preheat phase, the charge materials became molten and began to attack the underlying concrete basemat. Brief descriptions of the test procedures for SURC-2 and SURC-4 are listed in Tables 3-4 and 3-5, respectively. Comprehensive measurements of melt pool temperature, erosion distance, sidewall heat losses, total gas production, total aerosol production, gas composition, and aerosol composition were taken throughout the test using a computerized data acquisition system.

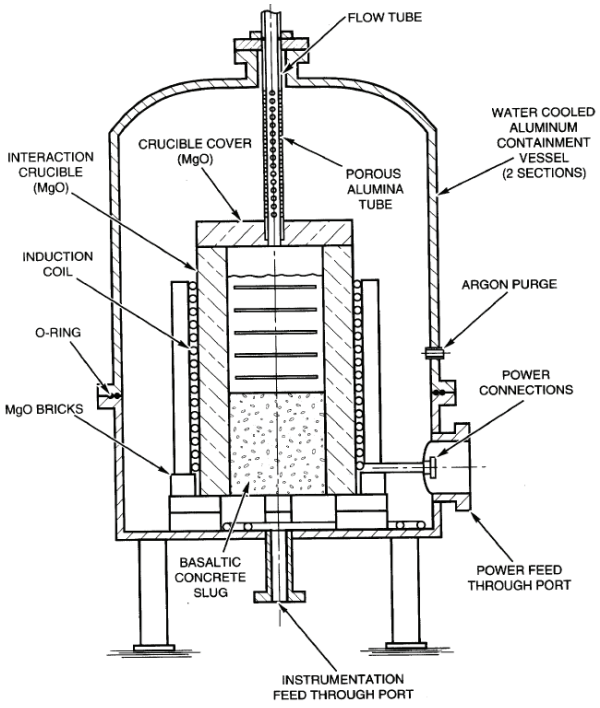

Fig. 3-1 SURC-2 experimental apparatus (Copus et al., 1992)

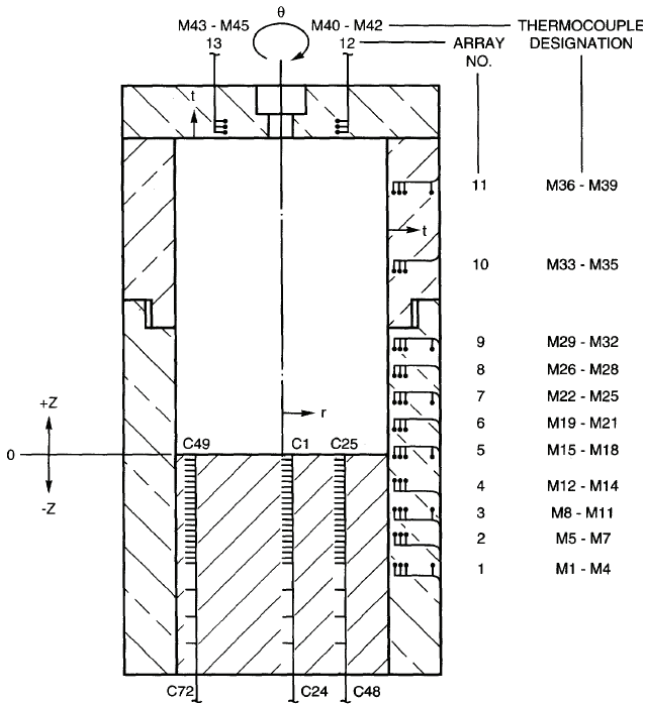

Fig. 3-2 Relative thermocouple locations for SURC-2 and SURC-4 (Copus et al., 1992)

Table 3-1 Chemical composition of the 304 stainless steel used in SURC-4 (Copus et al., 1992)

Element	Fe	Cr	Ni	Si	Cu	Mo	Mn	C	P	S
Weight percent (%)	71.18	18.50	8.25	0.50	0.25	0.25	1.00	0.04	0.02	0.01

Table 3-2 Melt composition in SURC-2 (Copus et al., 1992)

Composition	UO_2	ZrO_2	Zr
Weight percent (%)	69.1	22.6	8.3

Table 3-3 Main chemical composition of the basaltic concrete used in SURC-2 and SURC-4 (Copus et al., 1992)

Composition	SiO_2	CaO	Fe_2O_3	Al_2O_3	MgO	K_2O_2	Na_2O	TiO_2
Weight percent (%)	56.1	13.4	4.3	7.0	3.85	3.74	1.40	0.75

Table 3-4 Test procedures of SURC-2 (Copus et al., 1992)

Time(minute)	SURC-2 Events
0.0	Start of data acquisition system
10.0	Power supply turned on; power meter reading 50 kW
40.0	Power increased to 100 kW
110.0	Power increased to 150 kW
130.0	Onset of concrete ablation
220.0	Power increased to 200 kW
280.0	Power supply turned off

Table 3-5 Test procedures of SURC-4 (Copus et al., 1992)

Time(minute)	SURC-4 Events
0.0	Start of data acquisition system
10.7	Power supply turned on; power meter reading 98 kW
44.0	Power increased to 200 kW
80.5	Power increased to 245 kW
105.4	Onset of concrete ablation
119.0	20 kg Zr delivered to the melt
162.5	Power supply turned off

3.2 Simulation conditions of SURC-2 and SURC-4

In order to model SURC-2 and SURC-4 experiment, the x-y two-dimensional geometry of initial particle configuration was established as shown in Fig. 3-3. Four types of particles were used to simulate different materials in the geometry, namely the melt, the concrete and two types of wall particles representing the MgO sidewalls. In addition, another two kinds of particles were set to represent the solidified melt and molten concrete for phase transition calculation. A detailed description of the physical properties of the materials is listed in Table 3-6. The bulk of MgO sidewalls were described with dummy wall particles of which the pressure was set to be 0.0 Pa and not calculated in each step, except for the layer of particles immediately contacted with the melt and concrete. Meanwhile, no-slip boundary condition was applied on this layer of particles as previously described in Section 2.5.2. The initial conditions of simulation for both experiments are listed in Table 3-7.

During the interaction process, when the solidus rate of the melt particles exceeded the set value, these particles would turn into crust particles, their velocities were corrected to 0.0 and their positions no longer changed. As to the concrete, when the solidus rate was equal to 0.0, the concrete was considered to have reached its melting point and obtained the heat equivalent to its latent heat, the concrete would be deemed as ablated and the corresponding particles would turn into fluid particles.

The solid fraction of corium was chosen considering the spreading experiment carried out with stainless steel (Suzuki et al., 1993), in which a value of 0.55 was suggested. Meanwhile, an immobilization volume solid fraction as 50 vol% was suggested in the VULCANO VE-U7 prototypic corium spreading benchmark (Journeau et al., 2006). The corresponding solid fraction of enthalpy considering heat of fusion can be calculated as approximately 0.45. Thus, a range of 0.45 to 0.55 can be considered as reasonable for oxidic and metal corium. In current study, a value of 0.55 was used for both studies.

The decomposition enthalpy of concrete in current study was chosen as 1.8 kJ/kg

(Sehgal, 2011; Journeau et al., 2012a). The decomposition enthalpy is defined as the enthalpy that is needed for concrete to be heated from room temperature to melting temperature (Sehgal, 2011; Journeau et al., 2012a). The effective melting temperature of concrete corresponds to the temperature at which 30–50 vol% is liquid. In current study, a melting temperature was chosen as 1350 K according to the experimental report (Copus et al., 1992) and the assessment of CORCON-MOD3 code for MCCI simulation (Strizhov et al., 1996).

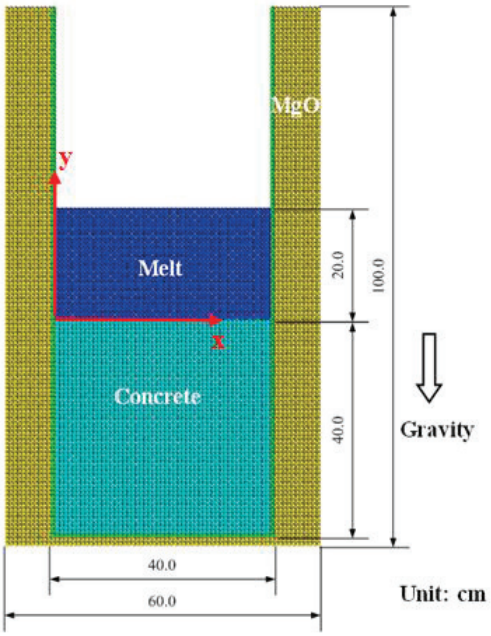

Fig. 3-3 Initial particle configuration

Table 3-6 Physical property of the materials (Copus et al., 1992)

Property	UO_2-ZrO_2-Zr	304 Stainless Steel	Concrete (Basaltic)	MgO
Density (kg/m^3)	8875	6920	2400	2680
Specific heat (J/kg·℃)	498	600	950	1250
Heat conduction coefficient (W/m·K)	1.5	18.9-28.9	1.5	6.7
Solidus temperature (K)	2173	1673	1350	
Liquidus temperature (K)	2673	1723	1650	
Latent fusion heat or decomposition enthalpy (kJ/kg)	367.04	280.0	1800.0	

Table 3-7 Initial conditions for SURC-2 and SURC-4

Parameters	SURC-2	SURC-4
Average distance between particles (m)	0.008	0.008
Total particle number	6951	7053
Initial melt temperature (K)	2720	1817
Initial concrete temperature (K)	300	300
Net input power (kW)	60-85	62

3.3 Results and discussion

3.3.1 Results of SURC-2 experiment

Figure 3-4 shows a series of figures depicting the simulated evolution of MCCI in the SURC-2 experiment. The configurations of the solidified and molten particles can be clearly seen. According to the experimental report, the concrete interaction began at 130 min (Copus et al., 1992). The solidified particles, namely the crust, appeared at a very

early stage (131.0 min) of MCCI on the interface between the melt and the concrete. As time continued, the solidified particles melted again. This solidified-and-remelted process continued throughout the whole simulation, indicating that the crust was continuously renewed, which has also been reported in the experimental observations. Although the concrete that was in intermediate contact with the crust could still be ablated by the crust of high temperature, the concrete ablation progression was to some extent delayed because the crust prevented the melt from moving downwards and the concrete from moving upwards. This influence on the concrete ablation rate would be discussed in detail in the following section. According to the simulation results, the fluid concrete particles gradually rose, merged into the melt pool and floated in the upper part of the melt pool due to its smaller density compared to the molten corium.

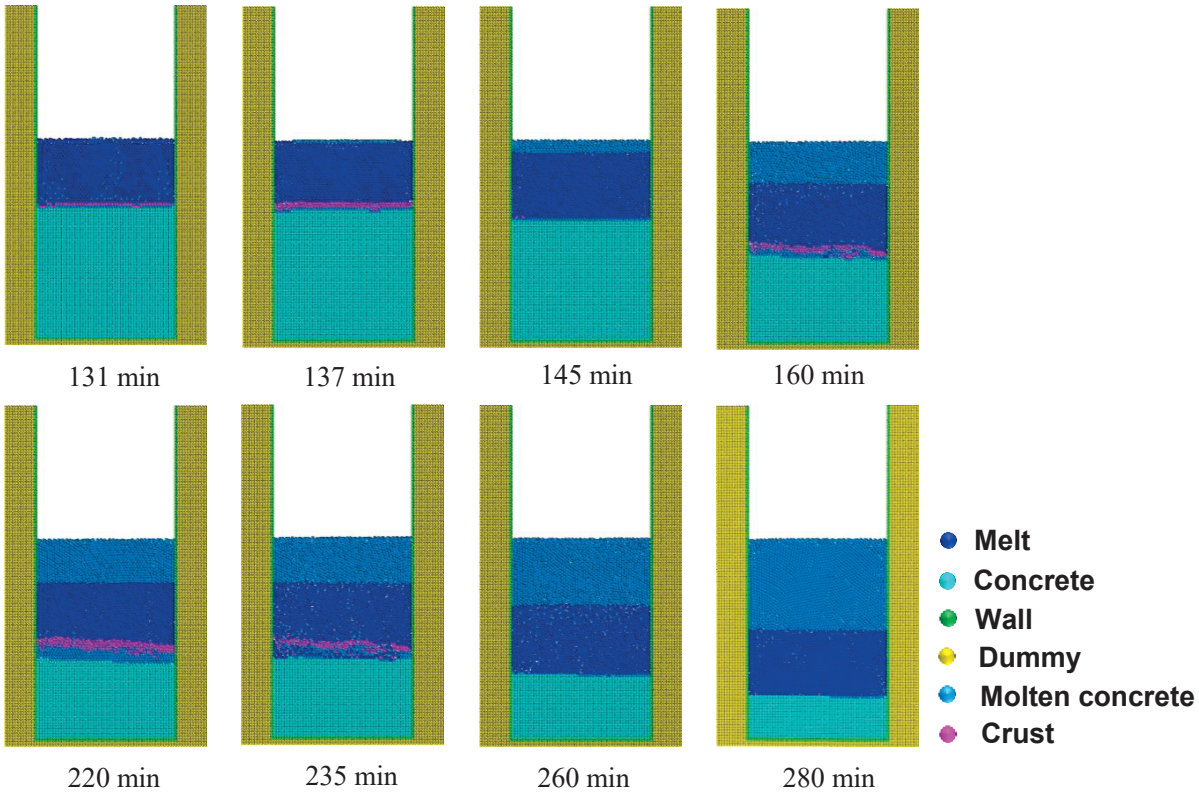

Fig. 3-4 Representative moments of simulated MCCI process of SURC-2 experiment

The simulated ablation front of concrete by MPS for SURC-2 experiment is compared with the results predicted by the CONCOR code (Strizhov et al., 1996) and

the experimental measurements as shown in Fig. 3-5. Good agreement can be seen from the figure. The ablation began at 130.0 min. According to the experimental report, the whole concrete ablation process could be divided into three phases, namely the initial phase, the mid phase and the late phase. The experimental and numerically predicted ablation rate of the three phases can be found in Table 3-8.

During the initial phase (130.0-160.0 min) of the interaction, nearly 15 cm of concrete is observed to be ablated with an average ablation rate of about 30 cm/h. The MPS predicted erosion rate during this phase was 30.8 cm/h, which is quite similar to the experimental value. The relatively high erosion rate is believed to be caused by the oxidation of Zr, which generates a considerable amount of heat during exothermic chemical reactions. The chemical reactions that were taken into consideration were shown in Eqs. 3-1 to 3-4. In the MPS code, the effects of the Zr on concrete ablation were taken into account by introducing the corresponding chemical heat calculated from these chemical reaction equations. The series of BETA (Alsmeyer, 1992) tests performed at KfK and the SURC-4 (Copus et al., 1989) test performed at SNL also showed the dominant effect of the Zr/SiO_2 condensed phase chemistry, i.e. the reduction of SiO_2 by metallic zirconium (Foit, 1997).

During the mid phase of the interaction (160.0 – 220.0 min), the concrete ablation rate dropped from 30.0 cm/h to 5.0 cm/h because all of the Zr metal had been oxidized. In the MPS simulation, following completion of the Zr oxidation, crust was formed on the interface between the melt and the concrete. This may indicate the reason for the significantly decreased concrete ablation rate. The crust prevented the higher temperature melt from directly contacting the concrete, thus slowed down the ablation progression. The crust did not seem to disappear until the net power to the melt was increased from 65 kW to 84 kW in the late phase (220.0-280.0 min). Significant increase in the ablation rate was also observed both in the experiment and the MPS simulation during the late phase after the power increase.

$$Zr + 2H_2O = ZrO_2 + 2H_2 + 701kJ/mol \quad Zr \tag{3-1}$$

$$Zr + 2SiO_2 = ZrO_2 + 2Si + 190kJ/mol \quad Zr \tag{3-2}$$

$$Si + 2H_2O = SiO_2 + 2H_2 + 500kJ/mol \quad Si \tag{3-3}$$

$$Si + 2CO_2 = SiO_2 + 2CO + 424kJ/mol \quad Si \tag{3-4}$$

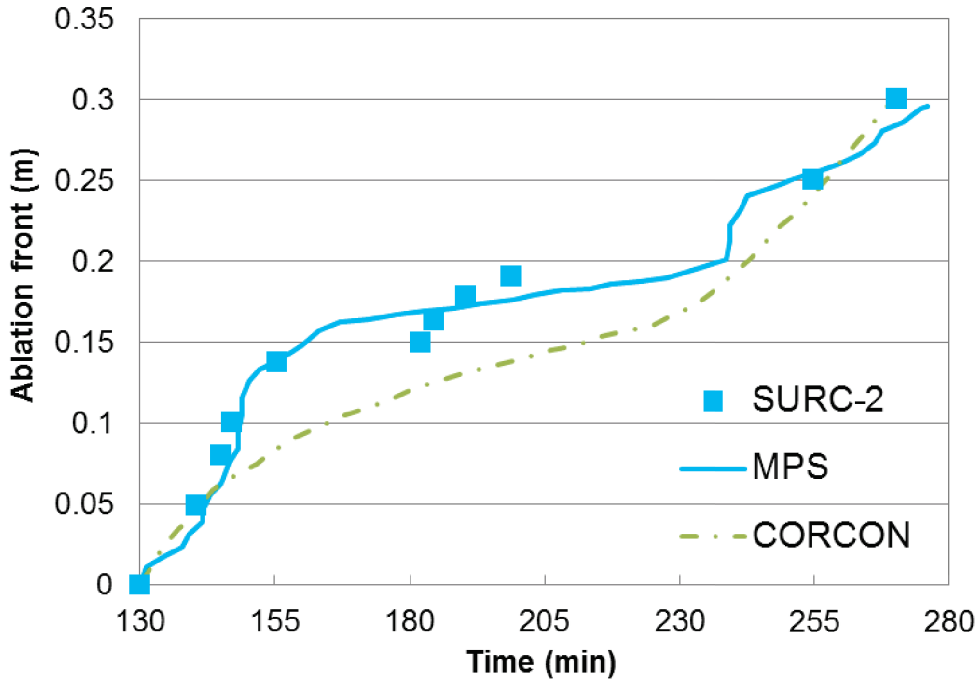

Fig. 3-5 Concrete ablation front history of the SURC-2 experiment

Table 3-8 Concrete ablation rate for different phases in SURC-2

Ablation rate (cm/h)	Initial phase (130.0-160.0 min)	Mid phase (160.0 – 220.0 min)	Late phase (220.0-280.0 min)
Experiment	30.0	5.0	15.0
MPS	30.8	4.4	13.9

3.3.2 Results of SURC-4 experiment

Figure 3-6 shows a series of representative moments for the simulated evolution of MCCI in the SURC-4 experiment. A layer of crust quickly formed at the interface between the melt and concrete at the beginning of the melt and concrete interaction. This fast crust formation is due to the high thermal conductivity of stainless steel compared with oxidic corium such as UO_2-ZrO_2. Then the concrete that is in direct contact with the crust began to melt at 107.0 min. The crust did not remelt into the melt pool until around 116.0 min, which hindered the concrete ablation to some degree during the first 10 minutes of the MCCI process. Twenty kg Zr was then added into the melt pool at 119.0 min, the oxidation process of Zr was estimated to last for 800.0-900.0s until around 133.0 min. During this period, the concrete was quickly ablated due to the chemical heat generated from Zr oxidation reactions. After the oxidation of Zr was over, crust was formed again at the interface between the melt and concrete, which slowed down the concrete ablation rate for the next 17 minutes. After the crust gradually remelted, the concrete ablation rate returned to a higher value and maintained to the end of the experiment.

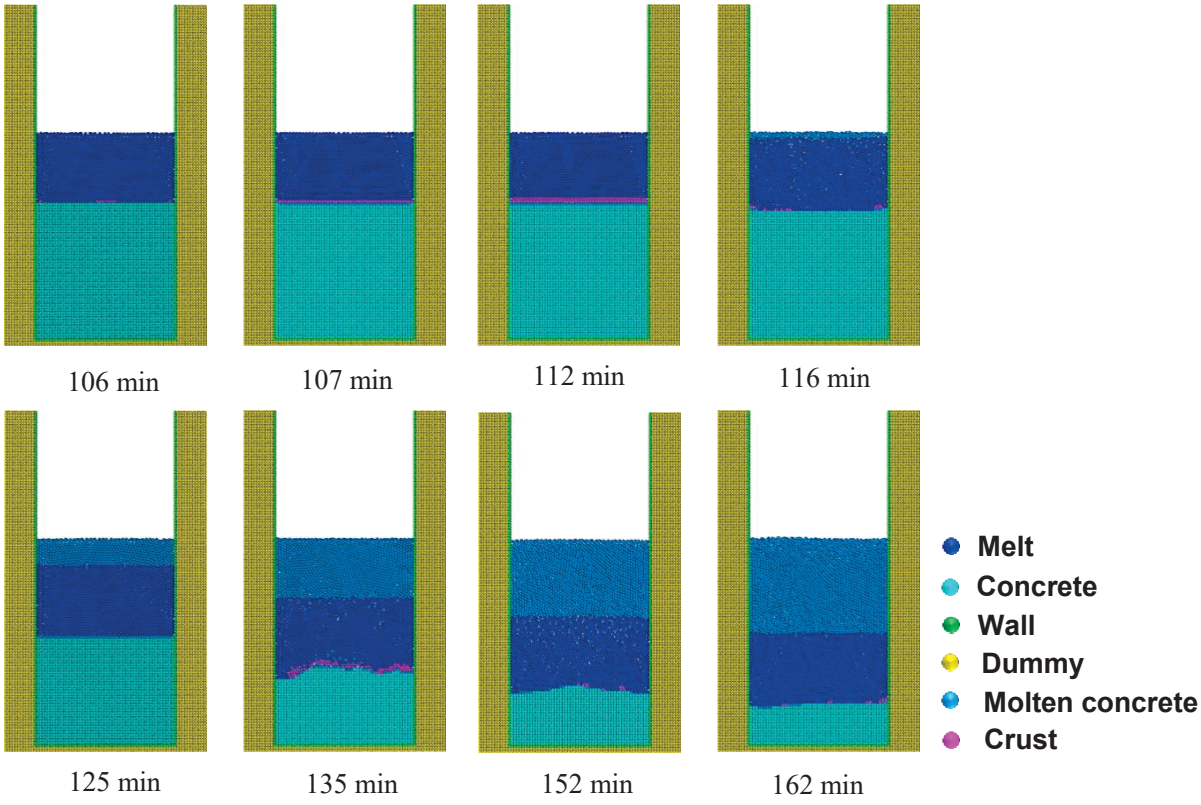

Fig. 3-6 Representative moments of simulated MCCI process of SURC-2 experiment

Figure 3-7 shows the ablation front of experimental measurements and the simulated results by CORCON (Strizhov et al., 1996) and MPS method. The corresponding concrete ablation rates for different phases by experiment and MPS are listed in Table 3-9. The ablation began at 105.0 min and 4 cm of concrete was ablated with an average ablation rate of 18.0 cm/h during the initial phase which lasted for 14 minutes. Then 20 kg Zr was added into the melt pool at 119.0 min. A significant increase of the concrete ablation rate to 48.0 cm/h was observed from 119.0 min to 135.0 min. The effect of the Zr oxidation on the concrete ablation process was also taken into consideration by introducing the corresponding amount of heat into the melt pool as was in the SURC-2 experiment. It can be obviously seen that Zr, even accounting for only less than 10% of the total mass of the melt, can tremendously increase the concrete ablation rate by triggering exothermic chemical reactions. From 135.0 min to 152.0 min, the concrete ablation rate dropped because the Zr oxidation was over and crust was formed again at

the bottom of the melt pool. The concrete ablation rate did not increase until the crust almost remelted at 152.0 min, after which the concrete ablation rate resumed to a higher value.

In Fig. 3-7, two arrays of thermocouples, namely the center and outer arrays, were selected since they presented slightly different responses of the concrete ablation depth. The specific configuration of the center (C1-C24) and outer array (C49-C72) thermocouples can be seen in Fig. 3-2. The outer array pronounced higher values than the center array after about 130.0 min, indicating that the circumferential ablation was faster than that of the central ablation. As for MPS simulation, the reason might be that the crust mainly forms at the central part of the interface between the melt and concrete instead of the peripheral part. Thus, the ablation front occurs earlier at the peripheral position than the central position, which could be observed at moments from 135.0 min to 162.0 min presented in Fig. 3-6. Generally, the predictions by the MPS method for both the center and outer arrays agreed well with the experimental data.

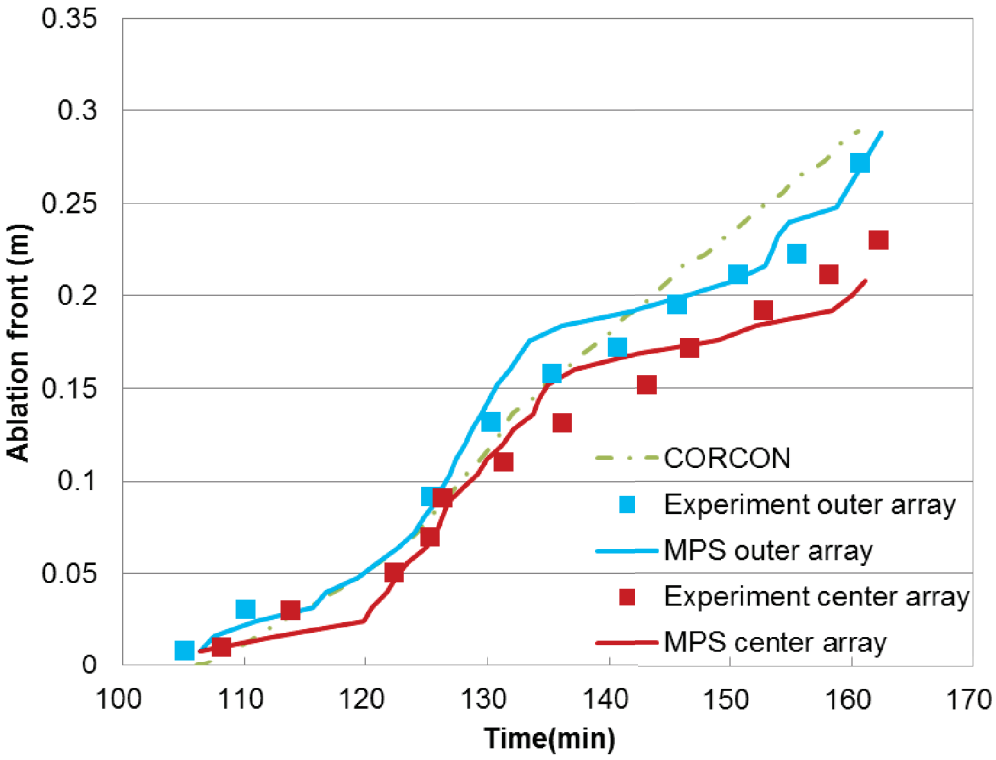

Fig. 3-7 Concrete ablation front history of the SURC-4 experiment

In Fig. 3-8, an indicator concrete particle was selected for temperature analysis. Figure 3-9 shows the temperature evolution with time of the indicator concrete particle. As can be seen from Fig.3-9, the temperature of concrete particle rapidly increased until curst started to form at around 108.0 min. Then during 108.0 to 121.0 min, in which steady crust formation was observed, the temperature increase of the indicator concrete particle dramatically decreased. However, as soon as crust remelted at 121.0 min, there was a small rapid temperature increase of the concrete particle as it moved upward and entered the melt pool. After the indicator concrete particle merged into the melt pool, the temperature slightly fluctuated as the concrete particle moved in the melt pool due to convection and finally stabilized to around 1958.0 K. Contrasting the rapid temperature increase observed before crust started to form (108.0 min) and the short period immediately after the crust remelted (121.0 min), the slow temperature increase during 108.0 to 121.0 min, in which steady crust formation was observed, indicated that crust formation can hinder the heat transfer process for concrete. As soon as crust came to formation, its coordinate was fixed in space. Thus, crust can serve as heat insulation between the melt pool and concrete. As a result, crust can reduce the effect of convective heat transfer, which is only possible when concrete is in direct contact with corium in the melt pool.

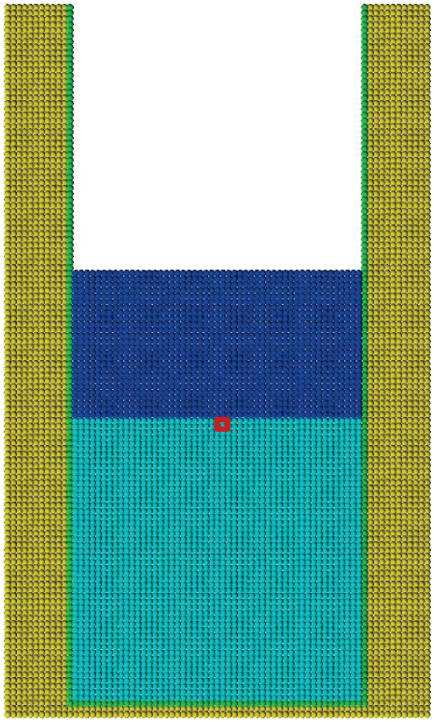

Fig. 3-8 The indicator concrete particle selected for temperature analysis (highlighted with red square)

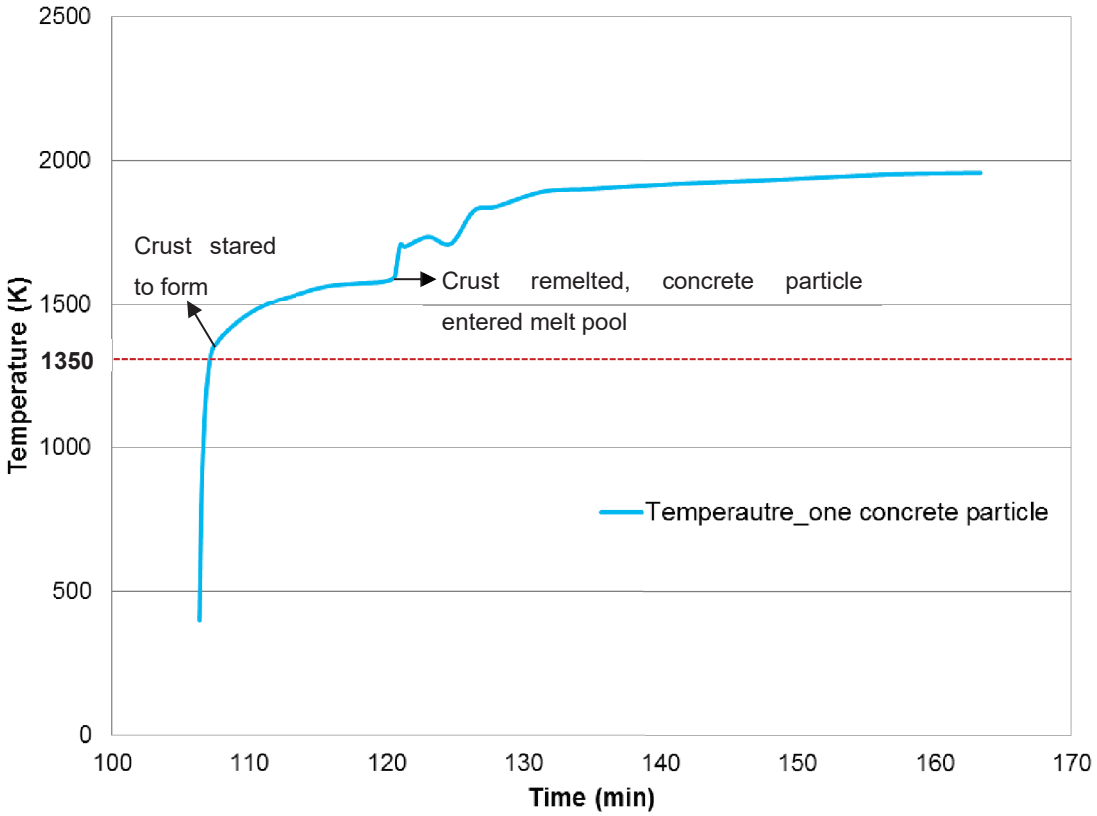

Fig. 3-9 Temperature evolution with time of one concrete particle in SURC-4

Table 3-9 Concrete ablation rate for different phases in SURC-4

Ablation rate (cm/h)	Initial phase (105.0-119.0 min)	Mid phase (119.0 – 134.0 min)	Late phase (134.0-162.0 min)
Experiment	16.0	40.0	27.0
MPS	17.1	44.7	24.0

3.3.3 Sensitivity study

Sensitivity study on particle size has been performed on SURC-4 experiment. The results of simulated ablation front history for cases with different particle sizes 0.005 m, 0.008 m and 0.1 m were compared with the experimental measurement and shown in Fig. 3-8. Large differences were not seen between the cases with particles sizes of 0.008 m and 0.005 m, while the case with 0.01 m has shown greater deviation from the first two cases and the experimental data. The effectiveness of heat transfer between two particles seems to be decrease with the increase of particle size. From currently study, it can be concluded that the choice of 0.008 m in current study is reasonable.

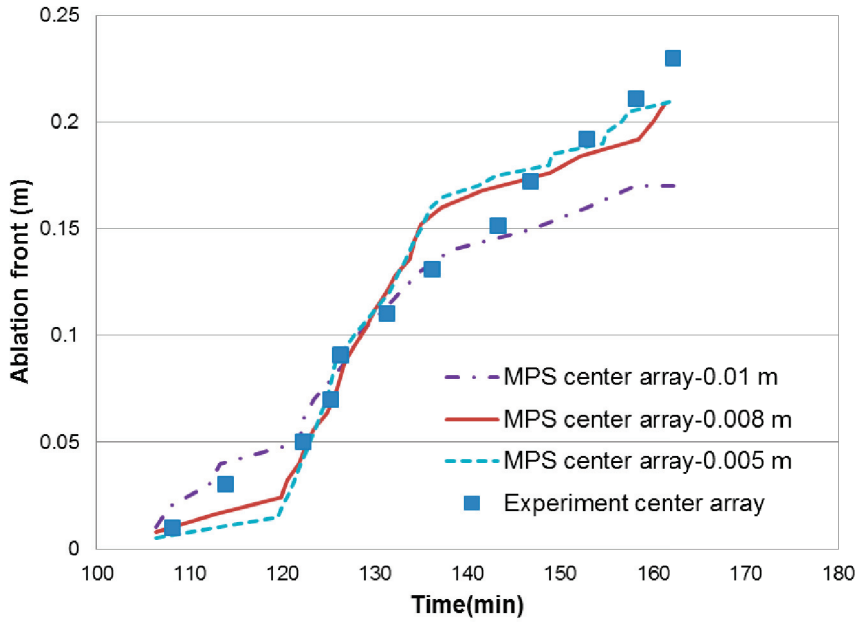

Fig. 3-10 Sensitivity study of SURC-4 experiment

3.5 Conclusions

In this chapter, the developed MPS code was applied to the SURC-2 and SURC-4 experiments intended for MCCI using prototypic oxidic materials and 304 stainless steel-Zr materials, respectively. The following conclusions can be drawn from the present simulation:

1) The simulated ablation front history of the concrete and the concrete ablation rate agreed well with those of the experiments, which not only validated the heat conduction, phase change and chemical reaction heat models but also demonstrated that the governing phenomena in MCCI has been captured, reproduced and properly modeled by the developed MPS method.

2) Crust formation and remelting was observed to occur on the interface between the melt and the concrete in the MPS simulation. During the period before crust was remelted, the concrete ablation rate calculated by MPS decreased significantly. It was indicated by the MPS results that the crust formation could play an important role in MCCI since it could slow down the concrete ablation rate by preventing the melt from interacting with the concrete. Although the experiments did not clarify this observation, the evidence for this phenomenon could be deduced from the decreased concrete ablation rate during the same period of interaction presented by the experimental results.

3) Dramatic increase of concrete ablation fronts have been observed from both experiments and MPS simulation results. This indicated that Zr oxidation by H_2O, Zr/SiO_2 condense phase reactions and the subsequence Si oxidation can significantly increase the ablation rate by introducing a large amount of chemical reaction heat into the melt pool .

Chapter 4 Simulations of 2-D MCCI experiments by MPS method

This chapter focuses on the simulations of 2-D MCCI experiments by MPS method with developed models described in Chapter 2. The simulations have been carried out on 2-D MCCI experiments CCI-2 and CCI-3. The research focus is to investigate the mechanism of isotropic and anisotropic ablation patterns in limestone-rich and siliceous concrete with prototypic oxidic corium. The originally developed slag film and crust dissolution models have also been validated by applying to CCI-2 simulations. The importance of gas generation and crust formation on corium-concrete interface and isotropic/anisotropic ablation pattern has been studied and stressed.

4.1 Test descriptions of CCI-2 and CCI-3

Core-Concrete Interaction (CCI) experiments were a series of large scale reactor materials experiments performed within the OECD/MCCI program in order to address remaining uncertainties related to long-term two-dimensional corium-concrete interaction under both wet and dry cavity conditions (Farmer et al., 2006). The corium melt was generated by chemical thermite reaction with specially designed exothermic chemical mixtures and was heated by direct electrical heating throughout the tests. The apparatus for containment of the corium melt consists of a test section that is about 3.4 m tall with a square internal cross-section which initially measures 50.0 x 50.0 cm. The principal components of the test section consist of a bottom support plate, two sidewall sections, one basemat section and an upper enclosure lid. The concrete basemat is initially 55.0 cm deep and each of the two concrete sidewalls (so called north and south sidewalls) is 56.2 cm thick, which provides about 20.0 cm of remaining sidewall thickness once the 35.0 cm axial and lateral ablation limits have been reached. The east and west sidewalls are made of an inert, refractory material MgO. Type K and Type C thermocouple assemblies were instrumented into the concrete sidewalls and basemat to record the temperature data regarding the two-dimensional ablation profile and melt as a

function of time. Figures 4-1 and 4-2 show the top view and side view of the main test sections. The main parameters of CCI-2 and 3 are listed in Table 4-1.

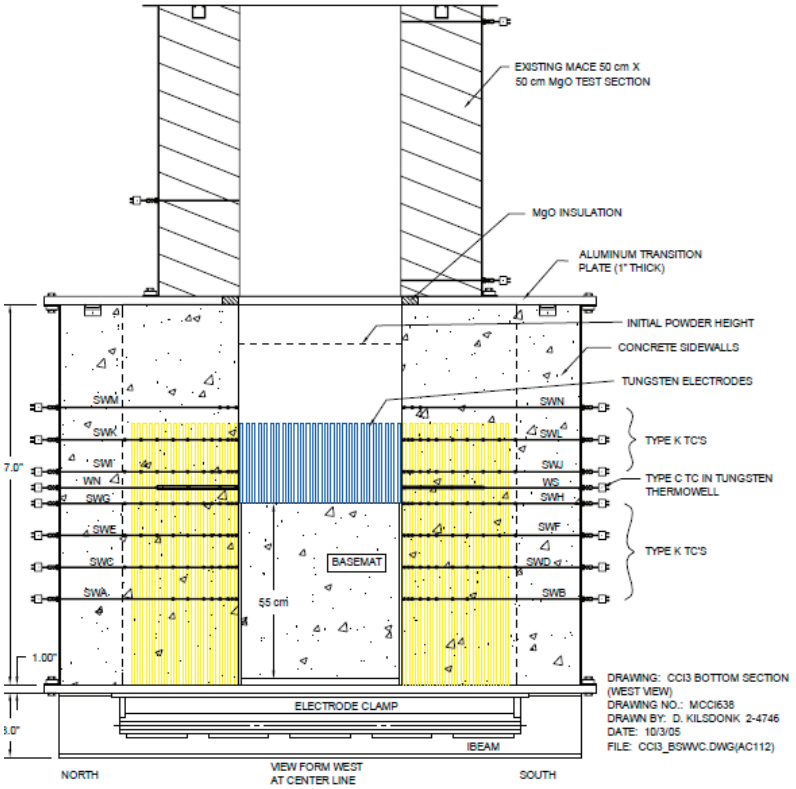

Fig. 4-1 Side view of CCI-2 and CCI-3 test section (Farmer et al., 2006)

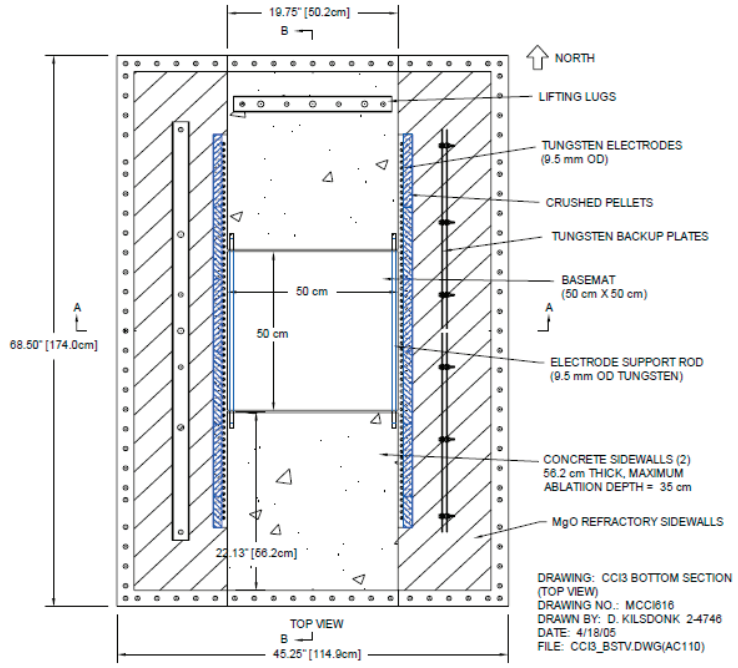

Fig. 4-2 Top view of CCI-2 and CCI-3 test section (Farmer et al., 2006)

Table 4-1 Main parameters of CCI-2 and 3 experiments (Farmer et al., 2006)

Test	CCI-2	CCI-3
Initial melt composition (wt%)	61% UO_2, 25% ZrO_2, 8% LCS concrete, 6% Cr	56% UO_2, 23% ZrO_2, 15% siliceous concrete, 6% Cr
Concrete type	Limestone/Common Sand	Siliceous Europe type
Electric heating power before water addition (kW)	120	120
Time of test duration before water addition (min)	300.8	107.6
Final cavity ablation pattern	Isotropic	Anisotropic

4.2 Simulation conditions of CCI-2 and CCI-3

CCI-2 and 3 experiments were simulated with two slightly different initial particle configurations as shown in Fig. 4-3. Since the geometry of the test sections in CCI 2 and 3 experiments is symmetrical, only half of the real test section geometry was built in consideration of computational cost. These two particle configurations with the same geometry are almost the same with the only difference lying in whether there exist particles that represent thermally stable aggregates in the concrete. For simulation of CCI-2 experiment, Configuration 2 was applied to all the cases since limestone aggregates are not stable and would decompose at high temperature. Thus the effect of aggregates on MCCI with limestone concrete was not stressed in particular in this study. For simulation of CCI-3 experiment, both Configuration 1 and 2 were used. The purpose of carrying out a case with Configuration 2 was to identify the effect of thermally stable aggregates on MCCI with siliceous concrete, since aggregates are believed to account for the anisotropic ablation profile for 2D MCCI experiments with siliceous concrete.

Five types of particles were used to represent different materials in the geometry,

namely the melt, the concrete, the aggregate and two types of wall particles. The aggregate particles were considered to distribute evenly within the concrete. Additionally, another two types of particles were set to represent the solidified melt (crust) and the molten concrete for phase transition simulation. The bulk of MgO sidewalls were described with dummy wall particles, and wall particles were applied on the layer that is immediately in contact with the melt and concrete. The difference between these two types of wall particles is that the pressure was set to be 0 and not calculated for dummy wall particles, while the pressure of wall particles was calculated in each time step. Meanwhile, nonslip boundary condition was applied on this layer of wall particles. The left sidewall was deemed as adiabatic during simulation. A detailed description of the physical properties of the materials was listed in Table 4-2.

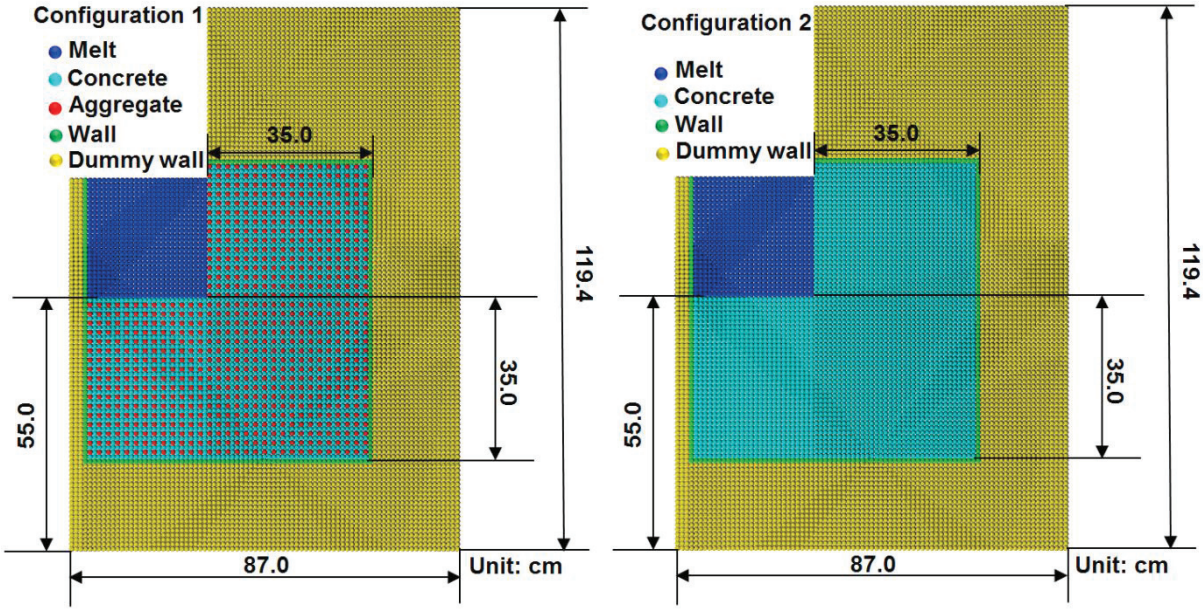

Fig. 4-3 Initial particle configurations for simulation

The physical properties of the melt, concrete and silica aggregates referenced several literatures on physical properties for these materials (Sevón, 2005; Doremus, 2002), and temperature dependence was taken into consideration during simulation for the specific heat of concrete and silica aggregate. The temperature dependence of the specific heat of silica aggregates and concrete was considered as shown in Fig. 4-4 and 4-5. For the specific heat of limestone concrete and siliceous concrete, curve 4 and curve 2 in

Fig.4-5 are selected for CCI-2 and CCI-3 simulation, respectively.

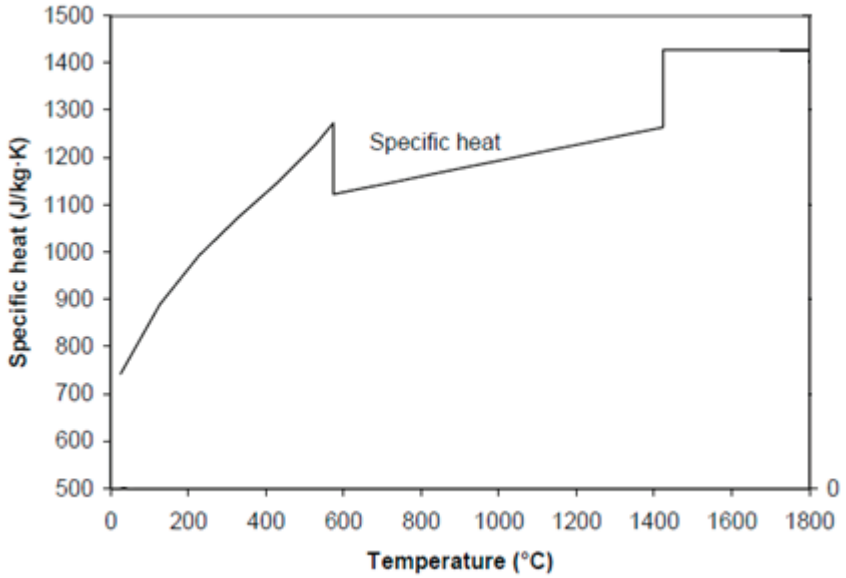

Fig. 4-4 Specific heat of silica with temperature change (Chase, 1998)

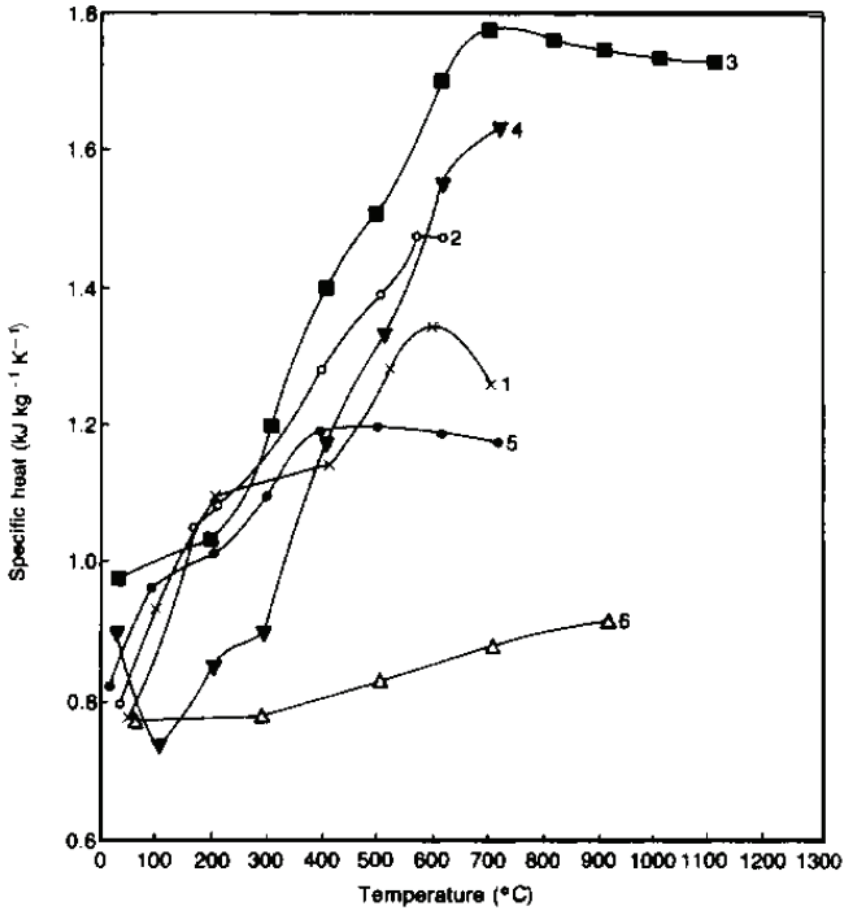

Fig. 4-5 Measured specific heats of siliceous (curves 2 and 3), limestone (1, 4 and 5)

and granite (6) concrete (Bažant and Kaplan 1996).

In reality, concrete can be regarded as a mixture of mortar (a mixture of sand, cement and water) and coarse aggregates. Here it has to be pointed out that the same physical properties of siliceous concrete were applied to the concrete particles in the simulation of CCI-3 test regardless of the existence of aggregates, namely the difference in physical properties of siliceous concrete and mortar was not considered in MPS simulation for CCI-3 test. Although it is more precise to apply the physical properties of mortar to the concrete particles in Configuration 1, it was not applied in current simulation for CCI-3 test. This is due to the fact that the composition of mortar can vary significantly for different manufacturing processes of different concrete. Consequently, it is very difficult to evaluate the precise thermal physical properties of mortar. Thus, the physical properties of siliceous concrete were applied to the concrete particles in all the cases of CCI-3. Since the influence of aggregates is the main research focus in CCI-3 simulation, this treatment will not significantly influence this objective.

The initial conditions of simulation for CCI-2 and 3 were listed in Table 4-3. Since the MPS simulation only considered dry cavity ablation, the simulation time is 300.0 min (18000.0 seconds) and 107.6 minutes (6456.0 seconds) for CCI-2 and 3 tests, respectively.

As to phase change simulation, initially, the melt particles were fluid, while the concrete and aggregate particles were solid, respectively. During the MCCI process, when the solid fraction of the corium melt particles exceeded a set critical value, these fluid particles would turn into solid crust particles, of which velocities were corrected to 0 and positions no longer change. For the concrete, when the solid fraction was equal to a set solid fraction, the solid concrete was deemed as completely melting and ablated. The corresponding solid concrete particles would turn into molten concrete particles of which the velocity and positions were updated by solving momentum equation. For the aggregates, they were deemed not to melt during the simulation. They would become

free to move once their adjacent concrete particles melted, and would flow into the melt pool to mix with the melt and molten concrete.

In the simulation of CCI-2 and CCI-3, the threshold solid fraction for corium particle to change into crust particle was selected as 0.55. The melting temperatures of siliceous concrete and limestone concrete were chosen as 1323 K and 1500 K according to the code manual of CORQUENCH (Farmer, 2011).

Table 4-2 Physical property of the materials (Farmer et al., 2006; Journeau et al., 2009b)

Property	Corium (For CCI-2)	Corium (For CCI-3)	Concrete (limestone, 300K)	Concrete (siliceous, 300K)	Aggregate (silica, 300K)	MgO (300K)
Density (kg/m^3)	6500.0	6500.0	2330.0	2270.0	2650.0	2680
Specific heat (J/kg·℃)	595.0	550.0	1250.0	845.2	782.6	1250.0
Thermal conductivity (W/m·K)	3.0	4.0	1.0	1.1	2.5	6.7
Solidus temperature (K)	1959.0	1573.0	1393.0	1373.0		
Liquidus temperature (K)	2865.0	2573.0	1568.0	1523.0		
Latent fusion heat or decomposition heat (kJ/kg)	500.0	300.0	2000.0	1800.0		

Table 4-3 Initial conditions for CCI-2 and 3 simulations (Farmer et al., 2006)

Parameters	CCI-2	CCI-3
Particle size (Initial average distance between particles) (m)	0.008	0.008
Simulation time (s)	18000.0	6460.0
Total particle number	8920	8920
Initial melt temperature (K)	2153.0	2223.0
Initial concrete temperature (K)	300.0	300.0
Input power (kW)	120.0	120.0

4.3 Results and discussion

4.3.1 Simulation results of CCI-2

Two cases were designed to study CCI-2 experiment. The main models and assumptions used in both cases are listed in Table 4-4. The only difference is that Case 1 used slag film model while Case 2 did not include slag film model. The main purpose of designing these two cases was to study the influence of gas generation on the corium/concrete interface and isotropic ablation in limestone concrete.

Figure 4-6 shows a series of representative figures depicting the simulated progression of MCCI in CCI-2 experiment. In general, both cases showed similar progress and isotropic ablation pattern until the end of the simulation. Early crust formation on the basemat and sidewall was found in both cases. Due to the existence of crust, which prevented the corium from being in direct contact with the concrete and limited the heat transfer to the concrete to mere heat conduction, the sidewall and basemat ablation did not occur until 830.0 s and 1110.0 s, respectively. Differences were observed not only in the time at which basemat and sidewall ablation occurred but also at which the basemat and sidewall crust remelted. This is caused by the difference between the heat transfer coefficient calculated from slag film model used in Case 1 and

the heat conductivity of concrete/corium/crust applied in Case 2. The slag film model generally slowed down the ablation progress and contributed to more crust formation on the basemat in the late phase (after 8000.0 s) of MCCI. This difference in basemat crust formation led to slightly different final cavity shapes in the end. Case 2 presented a more flat and deeper basemat ablation front, while Case 1 presented more sidewall ablation but with a similar sidewall ablation front with that of Case 2. The more sidewall ablation in the final cavity of Case 1 is also due to the higher heat transfer coefficient between molten concrete and concrete calculated from slag film model.

Table 4-4 Main models and assumptions in cases for CCI-2 simulation

Models and assumptions	Case 1	Case 2
Slag film model	Yes	No
Crust dissolution model	Yes	Yes
Sidewall crust formation	Yes	Yes

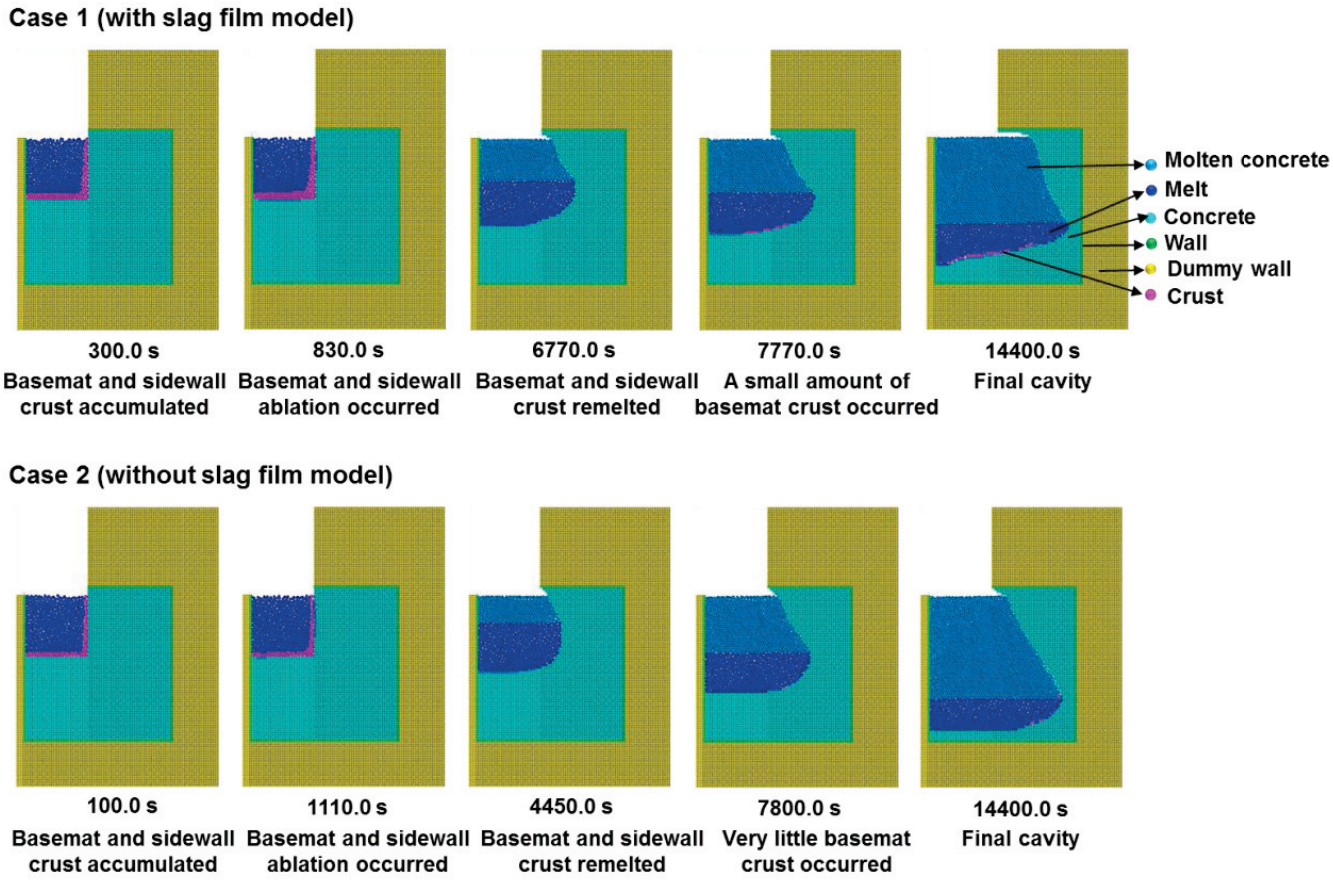

Fig. 4-6 Representative moments of simulated MCCI process in CCI-2 experiment

Figures 4-7 and 4-8 show the MPS simulation results and the corresponding experimental measurements of the sidewall and basemat ablation fronts in CCI-2, respectively. Generally, good agreement is obtained with a slight overestimation for both sidewall and basemat ablation fronts of MPS simulations. A comparison with the calculation results from CORQUENCH code was also presented. Since the Bradley slag film heat transfer model (Farmer, 2011) was applied on both sidewall and basemat concrete surfaces and there was no spatial nasalization considered in CORQUENCH, CORQUENCE presented identical results for sidewall and basemat ablation, both of which tends to underestimate the ablation depth and rate. The progression of ablation front is smoother in Case 2, while Case 1 presented more rugged and stepwise progression. This can be attributed to more crust formation and remelting processes in

Case 1 simulation compared with that in Case 2.

From the experimental dada in Figs. 4-7 and 4-8, it can also be noticed that there are several increases in the sidewall and basemat ablation rates at different time. The time for north sidewall, south sidewall and basemat ablation rate increases is around 2200.0 s, 2500.0 s and 5500.0 s, respectively. This indicates that there might have been some sidewall crust and basemat crust formed at the early stage of CCI-2 experiment and then could have remelted or broken later, thus causing the sudden increase in the ablation rates. The simulation in Case 1 reproduced the acute increases in the sidewall and basemat ablation rates at around 2500.0 s and 5500.0 s. Similar experimental observations of this fast removal of thermally destructed concrete have also been reported in other MCCI experiments – SURC, ACE and MOCKA test series (Foit et al., 2014), which pointed out that crust of high temperature could also heat the concrete to a temperature that is close to the concrete decomposition temperature and lead to fast ablation once the crust broke. In general, Case 1 with slag film model reproduced the experimental data better by more accurately capturing the crust formation and remelting processes.

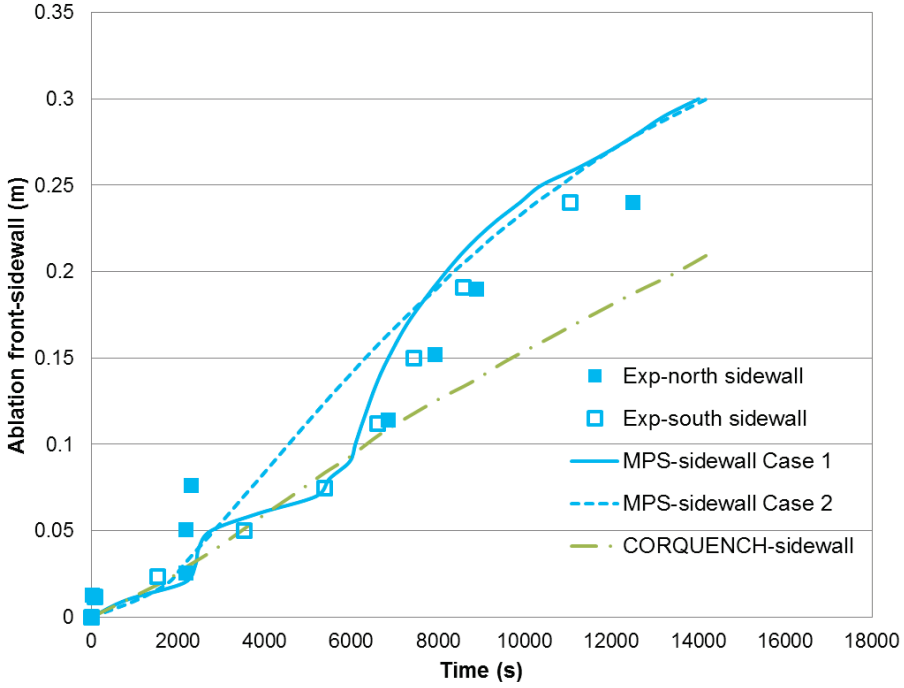

Fig. 4-7 Sidewall ablation fronts of MPS simulation and CCI-2 experimental measures

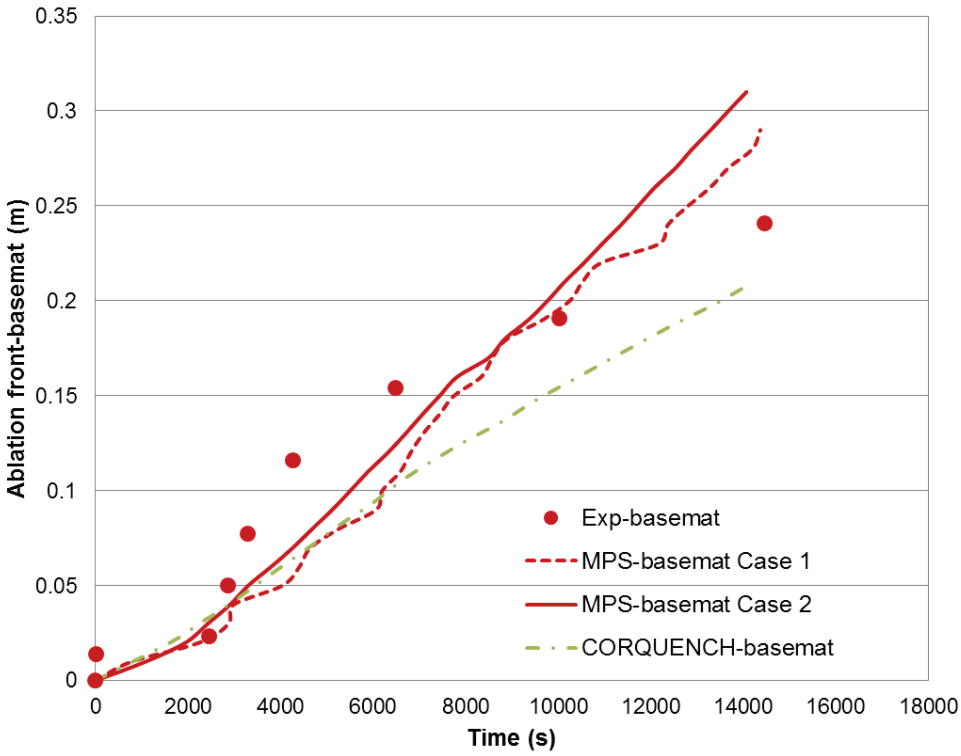

Fig. 4-8 Basemat ablation fronts of MPS simulation and CCI-2 experimental measures

Table 4-5 shows the comparison of the basemat and sidewall ablation rates predicted by MPS simulation and calculated from experimental data of CCI-2. Case 1 presented a better agreement with the calculations from experimental measurements than Case 2. The sidewall/basemat ablation ratios for both cases and the experimental value are around 1.0, in accordance with the fact that isotropic ablation pattern was observed from both experiment and simulations.

Table 4-5 Experimental and MPS predicted concrete ablation rate for CCI-2

	Experiment	MPS (Case 1-With slag film model)	MPS (Case 2-Without slag film model)
Basemat ablation rate (cm/h)	6.0	7.0	7.9
North Sidewall ablation rate (cm/h)	6.9	7.5	7.6
South Sidewall ablation rate (cm/h)	7.8	7.5	7.6
Sidewall/Basemat ablation ratio	1.2	1.1	0.96

4.3.2 Simulation results of CCI-3

Four cases were designed to study CCI-3 experiment. The main models and assumptions used in four cases are listed in Table 4-6. Slag film model and crust dissolution model are not included in CCI-3 simulation, which means that the influence of gas generation on the corium/concrete interface and crust dissolution effect were neglected for siliceous concrete. Since siliceous concrete generates much less CO_2 during decomposition, which means that the influence of gas generation on the corium/concrete interface and crust dissolution effect were neglected for siliceous concrete. Since siliceous concrete generates much less CO_2 during decomposition, the effect of slag film can be ignored. On the other hand, the diffusivity of siliceous concrete is much smaller than that of limestone concrete, resulting in much less rapid crust dissolution (Carenini et al., 2007). Therefore, neglect of gas generation and crust dissolution effect can be regarded as reasonable for siliceous concrete. The no sidewall crust assumption was made based on the observation that CCI-3 experiment showed evidence of initial crust formation on the concrete basemat, but there was no evidence

of initial sidewall crust formation for this test (Farmer et. al., 2006). Moreover, this phenomenon was also observed in other MCCI tests performed with siliceous concrete, such as VULCANO VB-U5 and VB-U7 (Journeau et al., 2012b). The main purpose of designing these four cases were to study the influence of aggregates and sidewall crust formation on anisotropic ablation pattern in siliceous concrete.

Table 4-6 Main models and assumptions in cases for CCI-3 simulation

Models and assumptions	Case 3	Case 4	Case 5	Case 6
Aggregates	Yes	No	Yes	No
Sidewall crust formation	No	No	Yes	Yes
Crust dissolution model	No	No	No	No
Slag film model	No	No	No	No

Figures 4-9 and 4-10 show four sets of figures depicting some representative moments of the simulated progression of MCCI in CCI-3 experiment. Case 3 and Case 5 used Configuration 1 in which relatively thermally stable silica aggregates were taken into consideration by assigning a special type of particles (red particles in the figure) that are evenly distributed in the concrete slug, while Case 4 and 6 used Configuration 2 in which the effect of silica aggregates was not stressed. No sidewall crust formation during the simulation was assumed for Case 3 and 4; while Case 5 and Case 6 assumed both sidewall and basemat crust formation during the simulation.

From the figures, it can be seen that both Case 3 and 4 presented significant anisotropic profiles in the cavity at the end of simulation, in which the lateral sidewall ablation was much more significant than the axial basemat ablation. This agreed with the post-test view of final cavity shape in CCI-3 experiment. Anisotropic profiles were also observed in the finial cavities in Case 5 and Case 6, but they were not as significant as those in Case 3 and 4. This is because the sidewall crust formation in Case 5 and

Case 6 at the beginning of the simulation hindered sidewall ablation, thus contributing to less sidewall ablation and more basemat ablation.

The sidewall ablation occurred at 250.0 s and 260.0 s while basemat ablation did not occur until at 3500.0 s and 3150.0 s for Case 3 and Case 4, respectively. As in Case 5 and Case 6, sidewall ablation and basemat ablation were both delayed until after 2600.0 s. The delay of concrete ablation was caused by the thick crust that was formed on the corium/concrete interface, which again suggested that crust formation can hinder concrete ablation. This so-called incubation period during which the ablation rate is very low is caused by crust formation on the corium/concrete interface, which plays an important part in MCCI. The duration of the incubation period was longer in Case 3 than that in Case 4. This is probably one of the effects that aggregates have on MCCI because aggregates are more thermally stable than concrete. Although the concrete that was in intermediate contact with the crust could still be ablated by the crust of high temperature, there was an obvious delay on the concrete ablation progression because the heat conduction between crust and concrete was much smaller than that between corium and concrete. Fluid corium could create a convective effect on the concrete that contacted with it, which could enhance the heat transfer between the corium and concrete, and lead to faster ablation than for the crust and concrete.

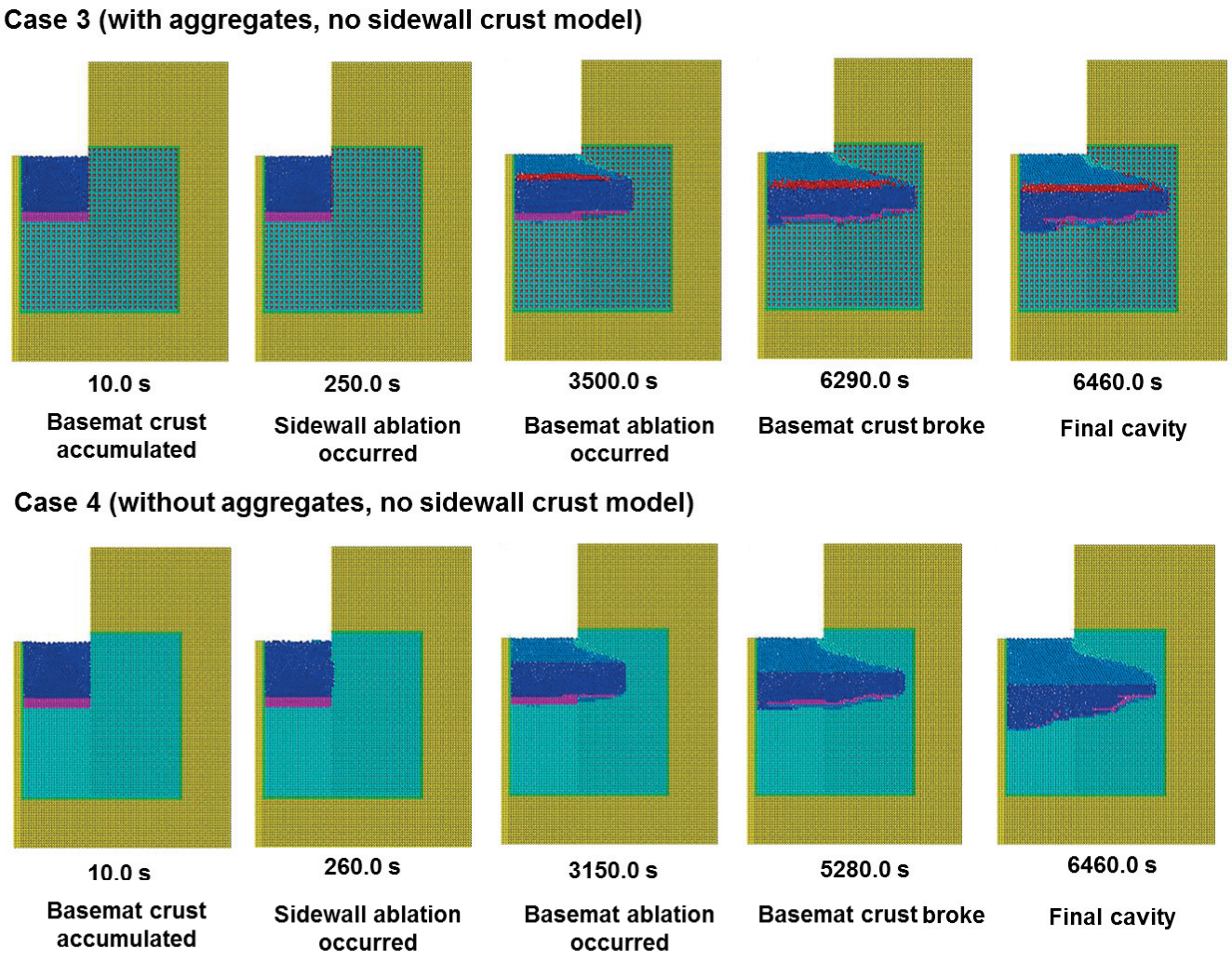

Fig. 4-9 Representative moments of simulated MCCI process in Case 3 and Case 4

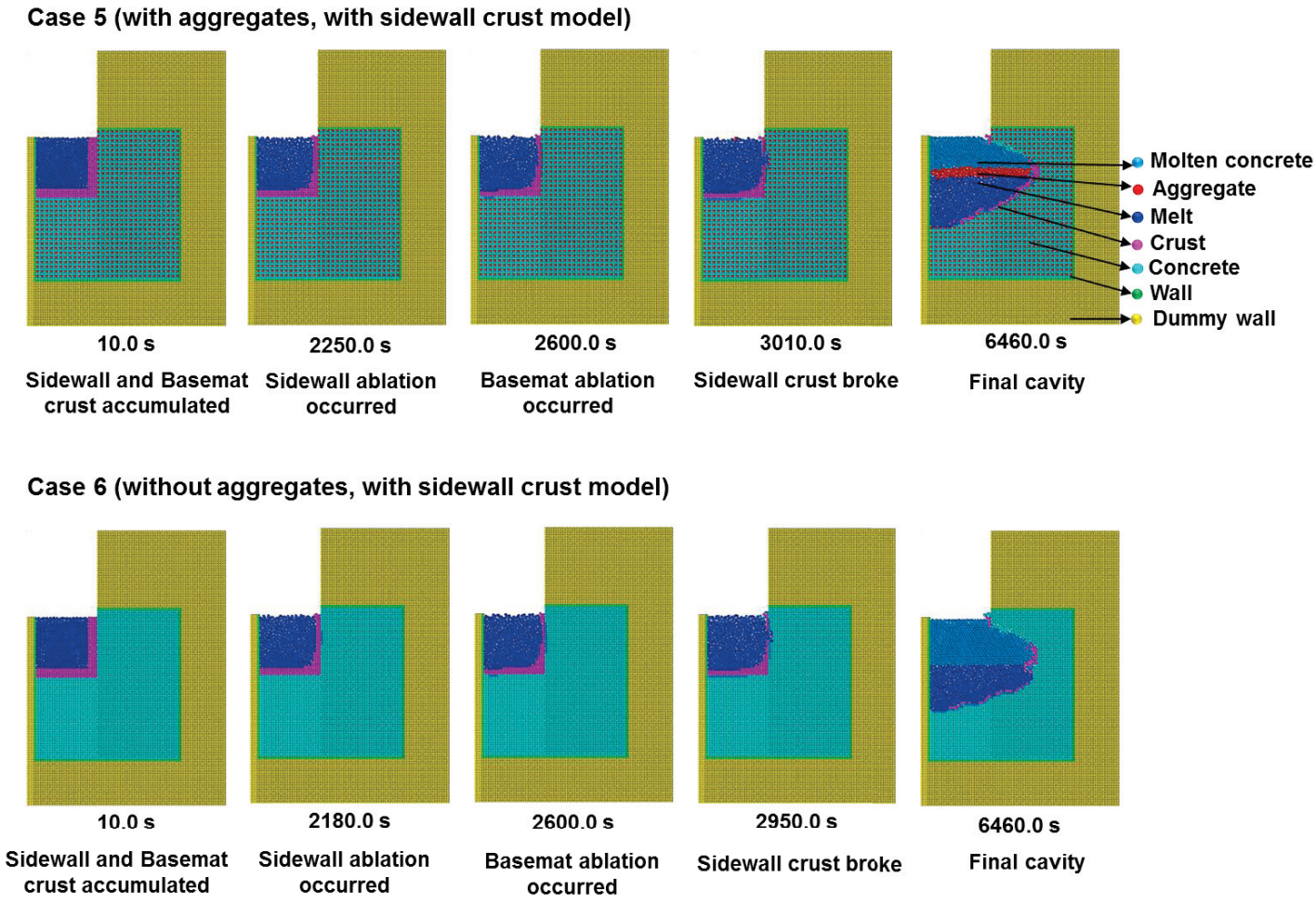

Fig. 4-10 Representative moments of simulated MCCI process in Case 5 and Case 6

For the final melt pool, stratification was observed in all the cases. Two zones can be clearly recognized: a corium melt phase immediately over the basemat and an overlying molten concrete phase. For Case 3 and 5, there was another phase comprised of aggregates between the corium melt phase and the molten concrete phase. This phenomenon agrees with the post-test observation of CCI-3 experiment (Farmer et al., 2006). The post-test observation indicated that two zones appeared to be present: a heavy monolithic oxide phase immediately over the basemat that was enriched in core oxides, with a second overlying porous, light oxide phase that was enriched in concrete oxides for siliceous concrete tests (Farmer et al., 2006). This stratification behavior was caused by the density difference between the materials. After melting, the molten

concrete and aggregate particles with lower density compared to corium melt gradually rose, merged into the melt pool, floated and occupied the upper part of the melt pool.

The simulated basemat (axial) and sidewall (lateral) ablation fronts of Case 3, 4, 5 and 6 are compared with experimental measurements in CCI-3 as presented in Fig.4-11. A comparison with simulation of CORQUENCH code for CCI-3 test was also included. In CORQUENCH simulation, the Bradley slag film model was applied for both sidewall and basemat surfaces. Thus, identical results of ablation fronts were obtained by CORQUENCH. However, CORQUENCH did not predict the sidewall and basemat ablation fronts well. Both the sidewall and basemat ablation front progressions were underestimated and the anisotropic ablation pattern was not obtained. This indicated that that the Bradley slag film model might not appropriate for simulation of MCCI with siliceous concrete. On the other hand, in MPS simulation, the isotropic ablation pattern was obtained successfully in general, which indicated that MPS simulation was capable of presenting anisotropic ablation by way of simulating convective heat transfer mechanistically. More specifically, the sidewall ablation fronts progressed much more quickly than the basemat ablation fronts. For sidewall ablation, Case 3 and Case 4 presented rather similar trends with Case 4 having a slightly faster ablation rate. Case 5 and Case 6 presented similar trends while Case 6 having a slightly faster ablation rate. This indicated that the influence of aggregates on sidewall ablation is relatively small.

In Case 3 and Case 4, the sidewall ablation rates were quite steady before basemat crust remelted while reached plateau after around 5000.0 s at which time basemat ablation rate started to increase quickly. This is because the basemat crust remelting gave rise to a sudden increase in basemat ablation rate, which resulted in the corresponding decrease in the sidewall ablation. The final lateral ablation fronts (depths) of Case 3 and Case 4 were almost the same, which were 32.0 cm each and generally agreed with the experimental measurement 29.2 cm at the end of the dry cavity ablation.

The sidewall ablation in Case 5 and Case 6 presented rather similar trends with that of Case 3 and Case 4. A plateau of sidewall ablation rate in Case 5 and Case 6 was also

reached after the sudden increase in basemat ablation rate due to basemat curst remelting. Case 5 and Case 6 presented a rather small sidewall ablation rate until the sidewall crust began to remelt at around 3000.0 s, after which the sidewall ablation rate began to increase dramatically until the sidewall crust started to form again at around 4700.0 s. The final sidewall ablation front (depth) of Case 5 was merely 20.0 cm, much smaller than that of Case 3 and Case 4 due to the hindering of ablation by early sidewall crust formation.

On the other hand, the axial ablation rates remained relative low compared to the lateral ones, especially for those in Case 3 and Case 4. The axial ablation rates of Case 3, Case 4, Case 5, and Case 6 remained steadily low and came to a significant rise after 6290.0 s, 5280.0 s, 4000.0 s and 3900.0 s, respectively. These moments were the time when basemat crust remelted for all the cases. For all cases, the basemat crust never formed again after the break. The final axial ablation fronts (depths) of the three cases were 0.05 m, 0.1 m, 0.14 m, and 0.15 m, respectively. This indicated that both crust and aggregates have an effect of slowing down basemat ablation.

The mechanistic reasons to support the theory that the aggregates have an effect on the anisotropic ablation profile with siliceous concrete can be deduced by comparing Case 3 and Case 4 (or Case 5 and Case 6). The reason why there is such delay in basemat crust break and slight delay in sidewall ablation can be perceived as that the aggregates have a higher thermal conductivity than concrete, which can influence the power split in the melt pool, namely the heat dedicated to the crust, the aggregate and the rest part of the concrete. As aggregates of higher thermal conductivity could gain more heat from the corium material than concrete, the heat that was distributed to the crust and concrete was less in Case 3 than Case 4, which resulted in later crust break and slower lateral ablation in Case 3.

On the other hand, by comparing the sidewall ablation rate in Case 3 and Case 5, the role of crust that played in slowing down the ablation rate can be further addressed. Meanwhile, anisotropic ablation pattern was still observed in Case 5 and Case with the

assumption of both sidewall and basemat crust formation. This indicated that anisotropy was not only caused by the incubation effect of crust but also associated with the characteristics of natural convection in an internally heated pool. Natural convection generally occurs when there is an imbalance between buoyant forces and viscous forces in the flow field (Kulacki et al., 1975). It is suggested by experiments that natural convection is largely anisotropic in an internally heated pool in absence of bubbling (Kulacki et al., 1975; Lee et al., 2007; Journeau et al., 2009). Figure 4-12 shows a close-up view of the velocity vector field in Case 5 at 3470.0 s. As can be seen from the figure, the velocity of corium particles near sidewall is higher than that of the corium particles near basemat, which suggests there is more intense convection near sidewall compared to the basemat. This observation is consistent with experiments carried out by C. Journeau in a rectangular pool with an internal heat source. In the experiment, natural convection in the pool exhibits a large anisotropy with a small heat transfer to the bottom wall (Journeau et al., 2009).

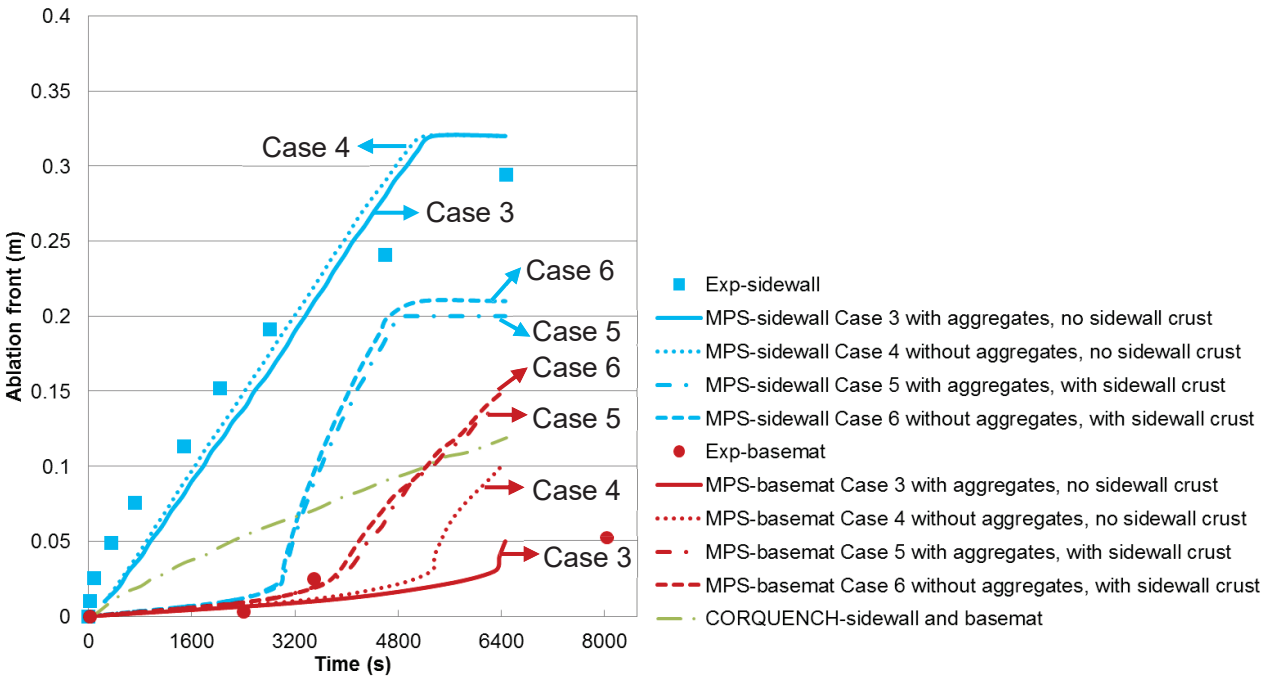

Fig. 4-11 Axial and lateral ablation fronts of MPS simulation and CCI-3 experimental measures

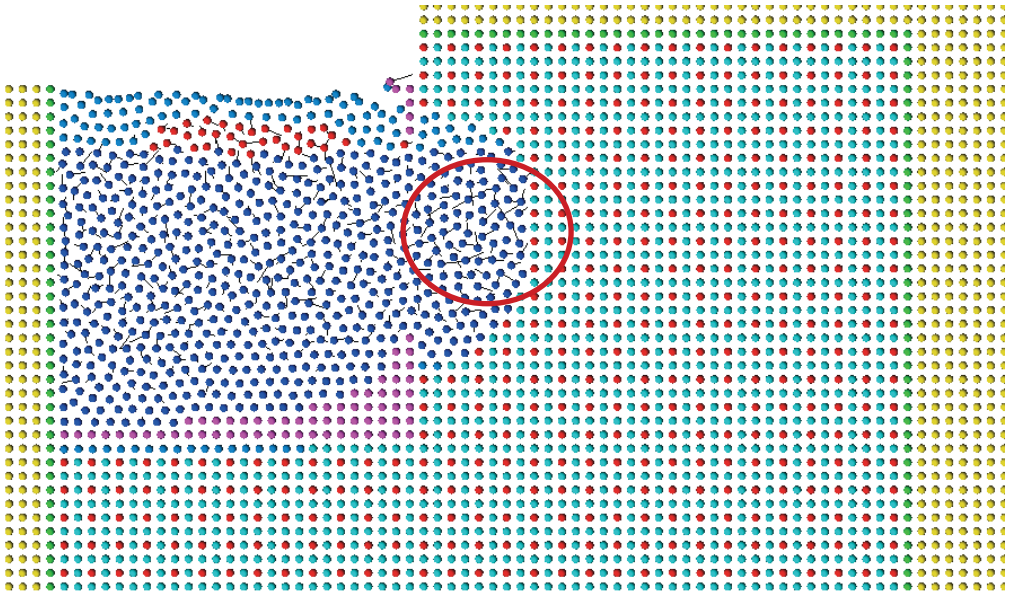

Fig. 4-12 A close-up view of velocity vectors in corium pool (Case 5 at 3470.0 s; velocity vectors shown in black lines)

The MPS predicted and experimental average ablation rate of CCI-3 are shown in Table 4-7. From the experimental observations of sidewall ablation in CCI-3 test, the dry cavity ablation process can be divided into two phases, which is marked by the time around 2800.0 s when basemat ablation began. The sidewall ablation rate after basemat ablation began (after 2800.0 s) was slowed down by the commencement of increase in axial basemat ablation rate. The lateral ablation rate before 2800.0 s predicted by MPS method for Case 3 and Case 4 are lower than that calculated from the experimental measurements, while the lateral ablation rate after 2800.0 s predicted by MPS method for both cases are higher than that from the experimental measurements. Case 5 and Case 6 presented totally reversed results with a relatively low lateral ablation rate (2.5 cm/h) before 2800.0 s and a high lateral ablation rate (18.0 cm/h and 18.7 cm/h). In general, considering the whole dry cavity ablation process, namely during first 6460.0 s of CCI-3 experiment, the overall average ablation rate predicted by MPS method in Case 3 and Case 4 agreed well with the value calculated from experimental measurements.

The overall average lateral ablation rate is about 6 times of the overall average axial

ablation rate. The axial ablation rate of Case 3 was close to the experimental measurement while those of Case 4 and Case 5 were two and three times as much as the experimental measurement. This indicated that both aggregates and curst could hinder the axial basemat ablation, and the influence of crust could be stronger. Meanwhile, due to the slight difference of lateral ablation rates before and after 2800.0 s in Case 3 and Case 4, the aggregates also have an influence on the lateral ablation rate. However, the effect is not as obvious as that on the axial ablation rate. As previously discussed, this may be caused by the difference in thermal conductivities of aggregates and concrete. The difference of influence on axial and lateral ablation rate can be considered as due to the different amount of aggregates that was gradually released from the basemat and sidewall into the melt pool. With more aggregates being gradually released into the melt pool as ablation progressed, the difference of lateral ablation rates of Case 3 and Case 4 gradually increased, which indicated more heat was dissipated to aggregates floating in the melt pool rather than sidewall and basemat crust in Case 3 than in Case 4. This again demonstrated the influence of aggregates on power split in MCCI.

Table 4-7 Experimental and MPS predicted concrete ablation rates for CCI-3

Average ablation rate (cm/h)	Test	MPS (Case 3)	MPS (Case 4)	MPS (Case 5)	MPS (Case 6)
Sidewall (before 2800.0 s)	24.4	20.6	22.5	2.5	2.5
Sidewall (after 2800.0 s)	10.2	15.7	14.0	18.0	18.7
Sidewall (in general)	16.3	17.8	17.8	11.1	12.8
Basemat	2.5	2.8	5.6	7.8	8.4

4.3.3 Sensitivity study

A sensitivity study of particle size is shown in Fig 4-13. For previous cases in this chapter, a particle size of 0.01 m was used. It can be seen that when particle size was decreased by 20% to 0.008 m, there is only slight difference in the prediction. However, when particle size was increased by 50% to 0.015 m, a significant underestimation of sidewall ablation rate can be seen due to a reduction in the resolution inadequate particles within the system. The sensitivity study suggests that current selection of particle size for CCI-3 study is reasonable.

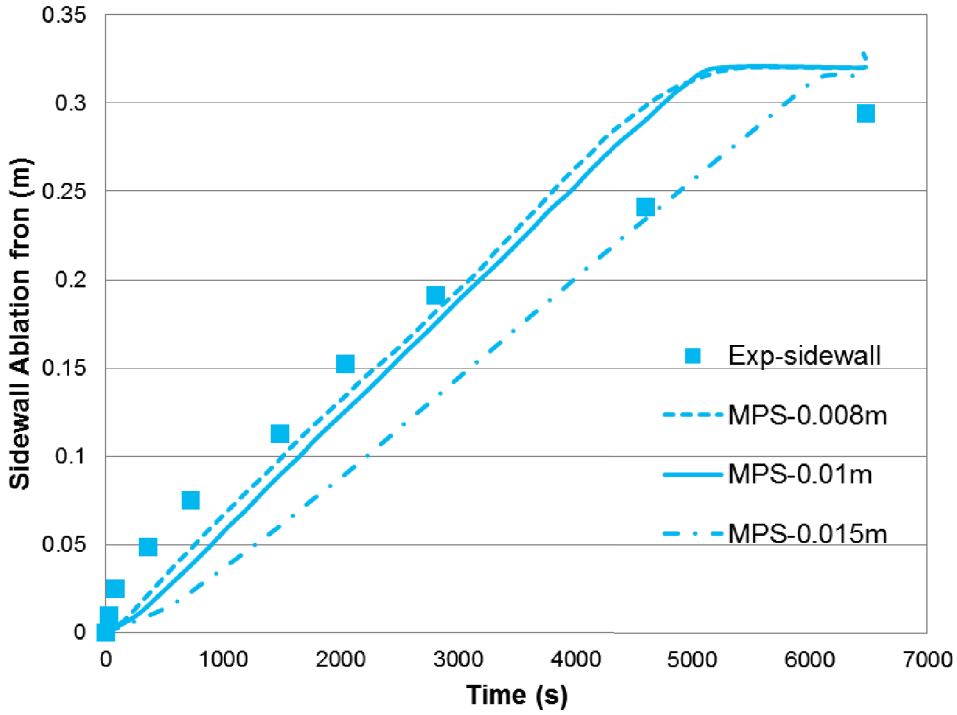

Fig. 4-13 Sensitivity study on particle size for CCI-3 simulation

4.4 Conclusions

In this chapter, the improved MPS code was successfully applied to numerical simulation of CCI-2 and CCI-3 experiments which intended to investigate the interaction of fully oxidized PWR core melts with 2-D limestone and siliceous concrete test sections. The following conclusions can be drawn from the present study:

1) Best estimation of CCI-2 and CCI-3 tests has been achieved by appropriate

assumptions and models. The assumptions and models for best estimation of CCI-2 and CCI-3 tests are listed in Table 4-8. For CCI-2 test with limestone/common sand concrete, best estimation can be obtained by assuming no aggregates and considering sidewall crust formation, slag film (gas generation) and crust dissolution. For CCI-3 test with siliceous concrete, best estimation can be achieved by considering the effect of aggregates, assuming no sidewall crust formation, and neglecting slag film (gas generation) and crust dissolution. These assumptions and models are applied in consistency with the different characteristics of limestone and siliceous concrete. For limestone concrete, the limestone aggregates can easily decompose at high temperature generating more CO_2 and its diffusivity is high. Thus, it is reasonable to assume no aggregates and consider slag film (gas generation) and crust dissolution. For siliceous concrete, the silica aggregates are thermally stable with high melting point and have been found to remain intact in MCCI experiments. Siliceous concrete also generation much less CO_2 and its diffusivity is ten times smaller than that of limestone concrete. Thus, it is reasonable to consider aggregates and neglect slag film (gas generation) and crust dissolution. Sidewall crust formation assumption is made based on experimental observations of MCCI experiments. Sidewall crust formation assumption is made based on observations of MCCI experiments, which suggested that sidewall crust formation is less likely to be found in MCCI experiments with siliceous concrete interacting with prototypic oxidic corium.

Table 4-8 Assumptions and models for best estimation of CCI-2 and CCI-3 tests

Models and assumptions	CCI-2	CCI-3
Aggregates	No	Yes
Sidewall crust formation	Yes	No
Crust dissolution model	Yes	No
Slag film model	Yes	No

2) The best estimation cases of MPS simulation reproduced the isotropic and anisotropic ablation patterns for CCI-2 and CCI-3 tests, which were in accordance with the post-test observation of cavity shape. The overall lateral and axial ablation rates evaluated from the MPS simulation results matched well with the experimental measurements, but the detailed ablation front history by MPS simulation had some deviation from the experimental measurements. The MPS simulation results showed that the average sidewall/basemat (lateral/axial) ablation rate ratios were about 1.0 for CCI-2 test and 6.0 for CCI-3 test, which were also consistent with the experimental observation.

3) Crust on the interface between the basemat and melt pool plays an important part in axial concrete ablation process. Early crust formation was predicted in both CCI-2 and 3 simulations. According to MPS simulation, the major delay of ablation was caused by the crust formation on the corium/concrete interface. Once the crust remelted, the ablation rate began to increase dramatically. This could also lead to temporary significant anisotropy in ablation rates. More study is needed to extrapolate current conclusion to plant scale. In real plant-scale MCCI, crust formation and break is also crucial to determine the progression of MCCI. However, the crust stability and break mechanism for real plant cavity needs more research and study.

4) The effect of gas generation was modeled with slag film model for simulation of CCI-2 test. The influence of gas generation tends to be increasing the heat transfer on the corium/concrete interface and favored more stable crust or crust formation. The gas sparging effect in the melt pool was not considered in the current study, which might contribute to less stable crust, more uniform lateral and axial heat fluxes and a more homogenous melt pool in general, resulting in a more isotropic ablation pattern for MCCI in limestone concrete with more gas generation.

5) Aggregates have an influence on both the axial and lateral ablation rate according to the analysis of the different MPS results for CCI-3 experiments: the cases with and

without aggregates. The differences in average basemat ablation rate between these two cases indicated that aggregates could hinder the axial ablation, while the influence on sidewall ablation rate was not as obvious as on the basemat one. The influence of the aggregates on power split in MCCI was also presented. Due to the higher thermal conductivity and density, aggregates could count for more power consumption than concrete.

6) Anisotropic ablation pattern is more associated with crust formation than with aggregates. The anisotropic heat flux distribution, in which lateral heat flux is larger than that of the axial one, in natural convection of a internally heated pool can also contributed to the anisotropic ablation pattern in MCCI with siliceous concrete.

Chapter 5 3-D Simulations of 2-D MCCI experiments

In previous sections, MPS method with original models has been applied to and validated against 1-D and 2-D MCCI experiments. Good agreement has been obtained through MPS simulation under proper assumptions. In this chapter, 3-D simulation of 2-D MCCI experiment VULCANO-VB U7 and COMET-L3 is presented, aiming to provide a more accurate simulation of the experiment geometry and investigate whether the assumptions and models that have been validated in 2-D simulations can also apply to the 3-D simulation.

5.1 Simulation of VULCANO-VB U7

5.1.1 Test descriptions of VULCANO-VB U7

VULCANO-VB U7 was one of the MCCI experiments carried out in the VULCANO experimental facility in Cadarache, France, under the cooperation between CEA and VTT. The test was proposed by VTT and was perfumed on 14th and 15th October 2009. The aim of the VULCANO VB-U7 test was to investigate the ablation by prototypic oxidic corium and a special sacrificial concrete that contains high percentage of hematite (Fe_2O_3) and is used for the EPR reactor pit. On the other hand, VULCANO VB-U7 was designed to complement the previous MCCI experiments carried out in the VULCANO facility. The previous VULCANO MCCI experiments indicated that with molten prototypic oxidic corium the ablation in limestone-rich concrete test block tends to be isotropic while the ablation in silica-rich concrete test block tends to be anisotropic. Yet, the mechanism of this phenomenon was not well understood. It was expected that with a different type of silica-rich and hematite-rich concrete VULCANO VB-U7 could lend help to further understand the phenomenon (Sevón et al., 2012; Ferry et al., 2010).

The experimental facilities included the VULCANO plasma arc furnace, which was

used to heat and melt the prototypic oxidic corium, and the concrete test section where the molten prototypic oxidic corium was poured in and the MCCI took place. The concrete test section was a rectangular concrete block measured 600 × 300 × 400 mm. There was a half-cylindrical cavity which was 300 mm in diameter and 250 mm high in the concrete block. It was used as a crucible to hold the corium. Induction heating was used to simulate the decay heat in the test. Thus, the concrete test section was inserted in a rectangular induction heater. 14 induction copper coils (25 x 10 mm) were placed at 5 mm intervals. The whole concrete block and the induction heater were surrounded with Siporex cellular concrete blocks used to provide insulation and protection. A detailed description of the test sections was depicted in Figs. 5-1 and 5-2 (Sevón et al., 2012; Ferry et al., 2010).

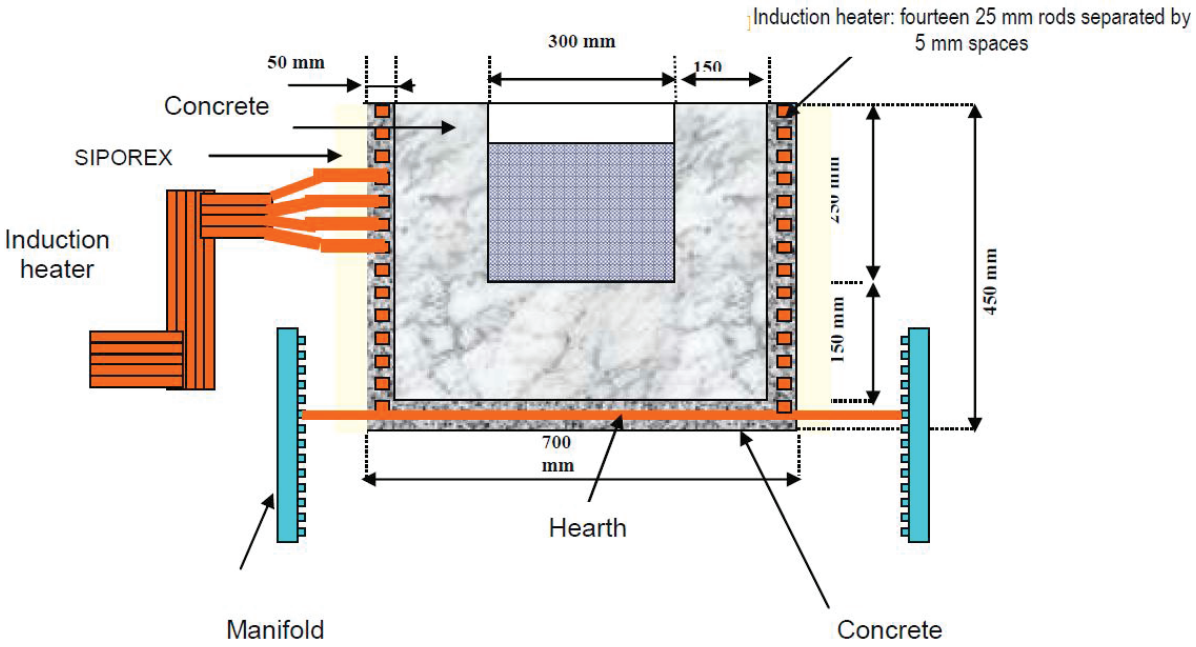

Fig. 5-1 Front view of the test section (Ferry et al., 2010)

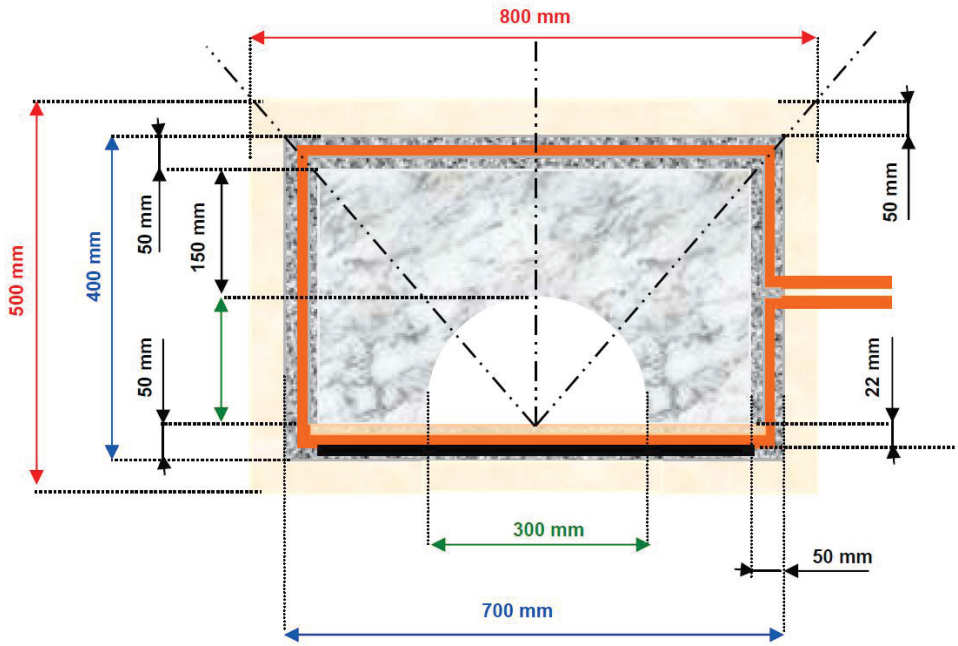

Fig. 5-2 Top view of the test section (Ferry et al., 2010)

The entire VB-U7 test lasted for about 2 hours and 40 minutes. 54 kg molten corium at about 2250℃ was poured into the cavity of the concrete test section. There was a small incident that a power outage occurred around 1 hour and 20 minutes and was restored 20 minutes later. Considering the reliability and validity of the experimental data, the MPS simulation was applied only to the period before power failure. The composition of corium and concrete used in the test were listed in Tables 5-1 and 5-2.

Table 5-1 Melt composition in VULCANO-VB U7 (Sevón et al., 2010)

Composition	UO_2	ZrO_2	SiO_2	FeO
Weight percent (%)	59.0	30.0	7.0	3.0

Table 5-2 Main chemical composition of the concrete used in VULCANO-VB U7 (Ferry et al., 2010)

Composition	SiO_2	Fe_2O_3	CaO	Al_2O_3	MgO	FeO	H_2O	CO_2
Weight percent (%)	45.5	32.9	12.7	3.3	0.3	0.2	3.7	1.4

5.1.2 Simulation conditions of VULCANO-VB U7

VULCANO-VB U7 experiment was simulated with two slightly different initial particle configurations as shown in Fig. 5-3. As in previous simulations for CCI-3 test, Configuration 1 was configured with no aggregates in the geometry, while Configuration 2 was configured with aggregates evenly distributed in the geometry. Both configurations were identical in size and represented only half of the real size of the test section used in VULCANO-VB U7 experiment in order to save computational cost. Five types of particles were used to represent different materials in the geometry, namely the melt, the concrete, the aggregate and two types of wall particles. The difference between these two types of wall particles is that the pressure was set to be zero and not calculated for dummy wall particles, while the pressure of wall particles was calculated in each time step. Meanwhile, nonslip boundary condition was applied on this layer of wall particles. Additionally, another two types of particles were set to represent the solidified melt (crust) and the molten concrete during phase change simulation.

The physical properties of melt, siliceous concrete and silica aggregates that are used in VULCANO-VB U7 simulation are listed in Table 5-3 (Ferry et al., 2010). The temperature dependence of the specific heat of siliceous concrete and silica aggregates was applied as mentioned in Section 4.3.1 (see Figs. 4-3 and 4-4). The initial conditions for VULCANO-VB U7 simulation are listed in Table 5-4 (Ferry et al., 2010).

The models and assumptions that applied in two different cases for simulation of VULCANO-VB U7 are listed in Table 5-5. The main difference is the assumption about

aggregates. Case 1 used Configuration 1 for aggregate assumption, and Case 2 used Configuration 2 to neglect the influence of aggregates. As in previous 2-D simulation of CCI-3 experiment, slag film model and crust dissolution model were not applied to simulate siliceous concrete. This is because siliceous concrete generates much less gas (CO_2) when it decomposes and its diffusivity is much less than that of limestone concrete.

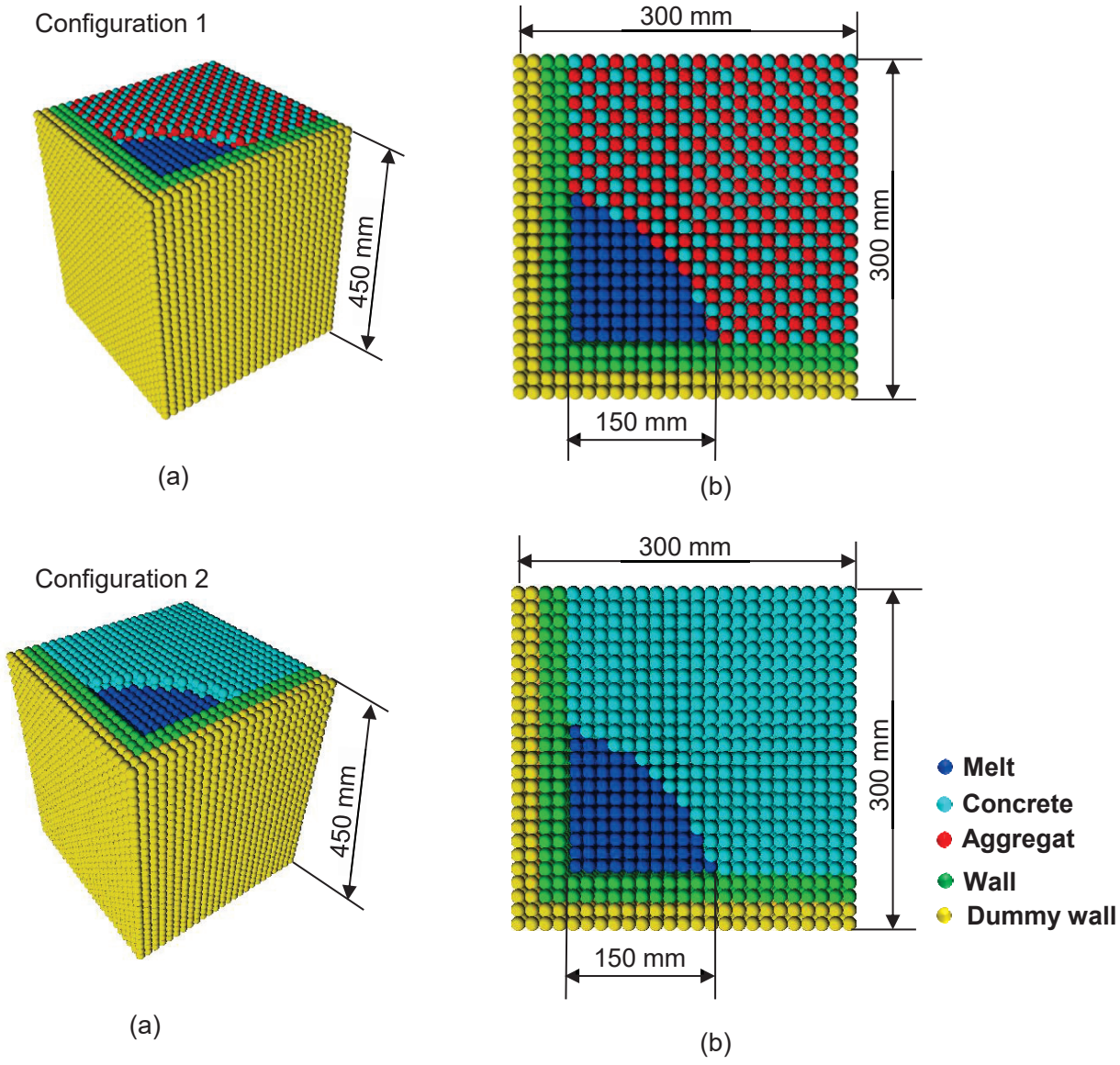

Fig. 5-3 Two particle configurations used for MPS simulation of VULCANO-VB U7: (a) 45 degree front view; (b) Top view

Table 5-3 Physical property of the materials used for VULCANO-VB U7 simulation (Ferry et al., 2010)

Property	Corium	Concrete (300 K)	Aggregate (silica, 300 K)
Density (kg/m^3)	7000.0	2600.0	2650.0
Specific heat (J/kg·℃)	541.0	845.2	782.6
Heat conduction coefficient (W/m·K)	3.6	1.1	2.5
Solidus temperature (K)	1463.0	1413.0	
Liquidus temperature (K)	2623.0	1703.0	
Latent fusion heat or decomposition heat (kJ/kg)	360.0	1800.0	

Table 5-4 Initial conditions for VULCANO-VB U7 simulation (Ferry et al., 2010)

Parameters	VULCANO-VB U7
Particle size (Initial average distance between particles) (m)	0.015
Simulation time (s)	4800.0
Total particle number	16559
Initial melt temperature (K)	2473.0
Initial concrete temperature (K)	300.0
Input power (kW)	21.2

Table 5-5 Main models and assumptions in cases for VULCANO-VB U7 simulation

Models and assumptions	Case 1	Case 2
Aggregates	Yes	No
Sidewall crust formation	No	No
Crust dissolution model	No	No
Slag film model	No	No

5.1.3 Results and discussion

The representative moments of both cases to simulate VULCANO VB-U7 were shown in Fig.5-4. As can be seen, both cases showed anisotropic ablation pattern in the final cavity. The time when sidewall ablation and basemat ablation occurred was almost the same. However, the final cavity in Case 2 showed more basemat ablation compared to Case 1. This indicated that aggregates did have an influence of enhancing anisotropy due to their thermally stable physical properties. The influence appeared to be stronger on basemat ablation compared to sidewall ablation. This is because in the cavity shape evolution in MCCI progression the melt (dark blue particles in Fig. 5-4) tends to come in contact with more aggregates. Combining temperature distribution shown in Fig. 5-5, it can be seen that the evolution processes of temperature distribution were slightly different in Case 1 and Case 2. Until stable basemat crust formed, which was at 700.0 s, the temperature distributions in both cases were quite similar. The temperature distributions on the corium-concrete interfaces on basemat and sidewall as shown in black circles were also similar. However, after stable basemat crust formed, the temperature distribution on the corium-concrete interfaces on basemat and sidewall for both cases became different. Generally, the temperature distribution on the corium-concrete interface on basemat of Case 1 was lower than that in Case 2. This was due to the thermally stable silica aggregates which have higher thermal conductivity and can consume more power than pure concrete. Thus, on one hand, the aggregates can

favor more stable crust formation on the basemat.

On the other hand, the existence of aggregates can lower the overall temperature of the corium, which can also facilitate the stable crust formation on the basemat. On the whole, the aggregates tend to influence the power distribution in the melt pool and reduce the temperature of whole melt pool. Moreover, the influence seems to be more significant on basemat ablation compared to sidewall ablation. This can be explained by the shape evolution of corium-concrete interfaces. As concrete ablation progressed with time, the area of corium-concrete interface on the sidewall tended to expand. However, since the upper part of the melt pool was occupied by molten concrete and aggregates if there were any due to density driven force, corium mainly occupied the lower part of the melt pool. Consequently, the area of corium-concrete interface on the sidewall that the corium came into contact with gradually reduced, while the area of corium-concrete interface on the basemat that the corium came into contact with gradually increased. In this way, the influence of the aggregates on the basemat is more significant since corium confronted more aggregates in the basemat region during MCCI progression.

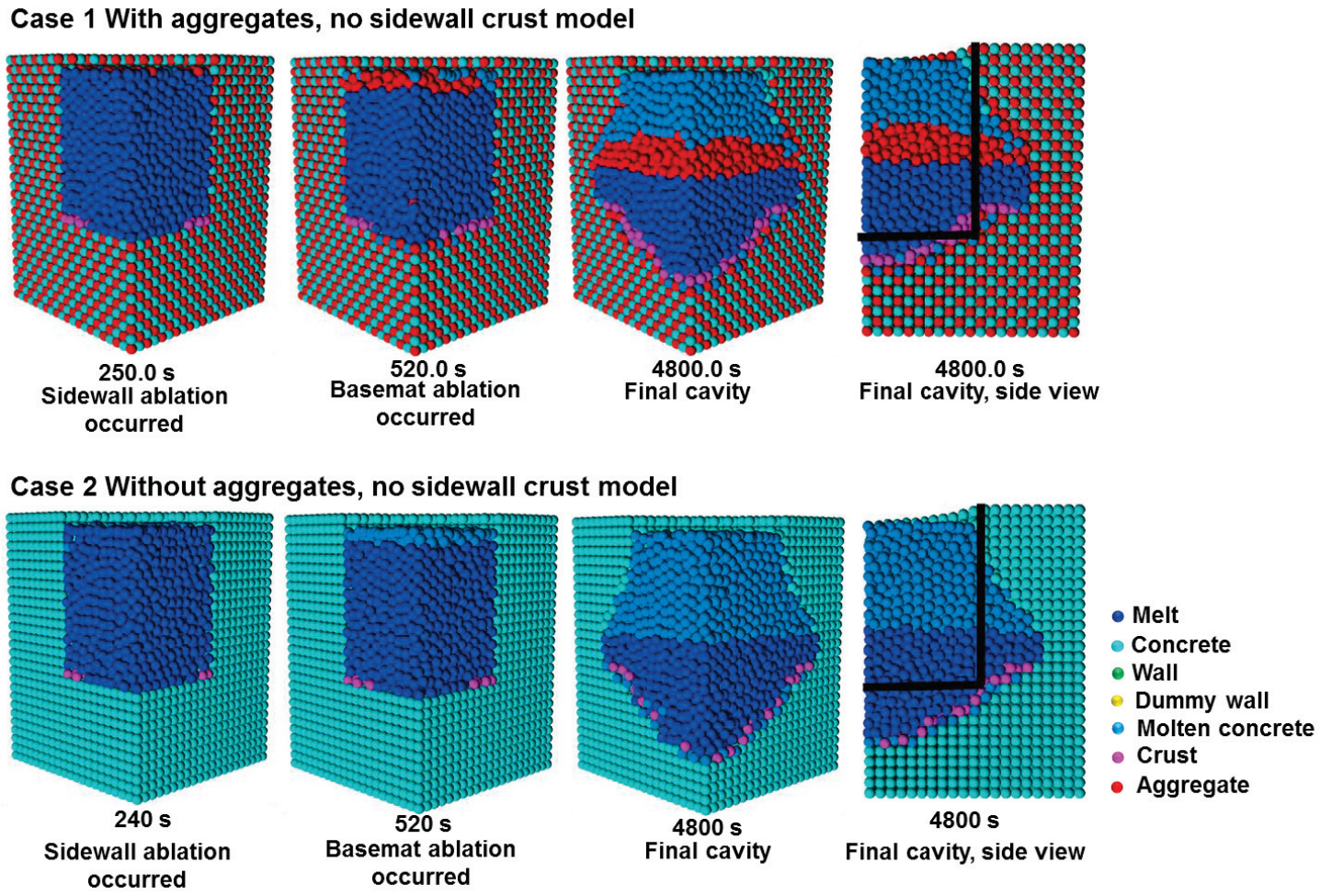

Fig. 5-4 Representative moments in Case 1 and Case 2 (Initial cavity shape was marked out by black solid lines in the last figure of Case 1 and Case 2)

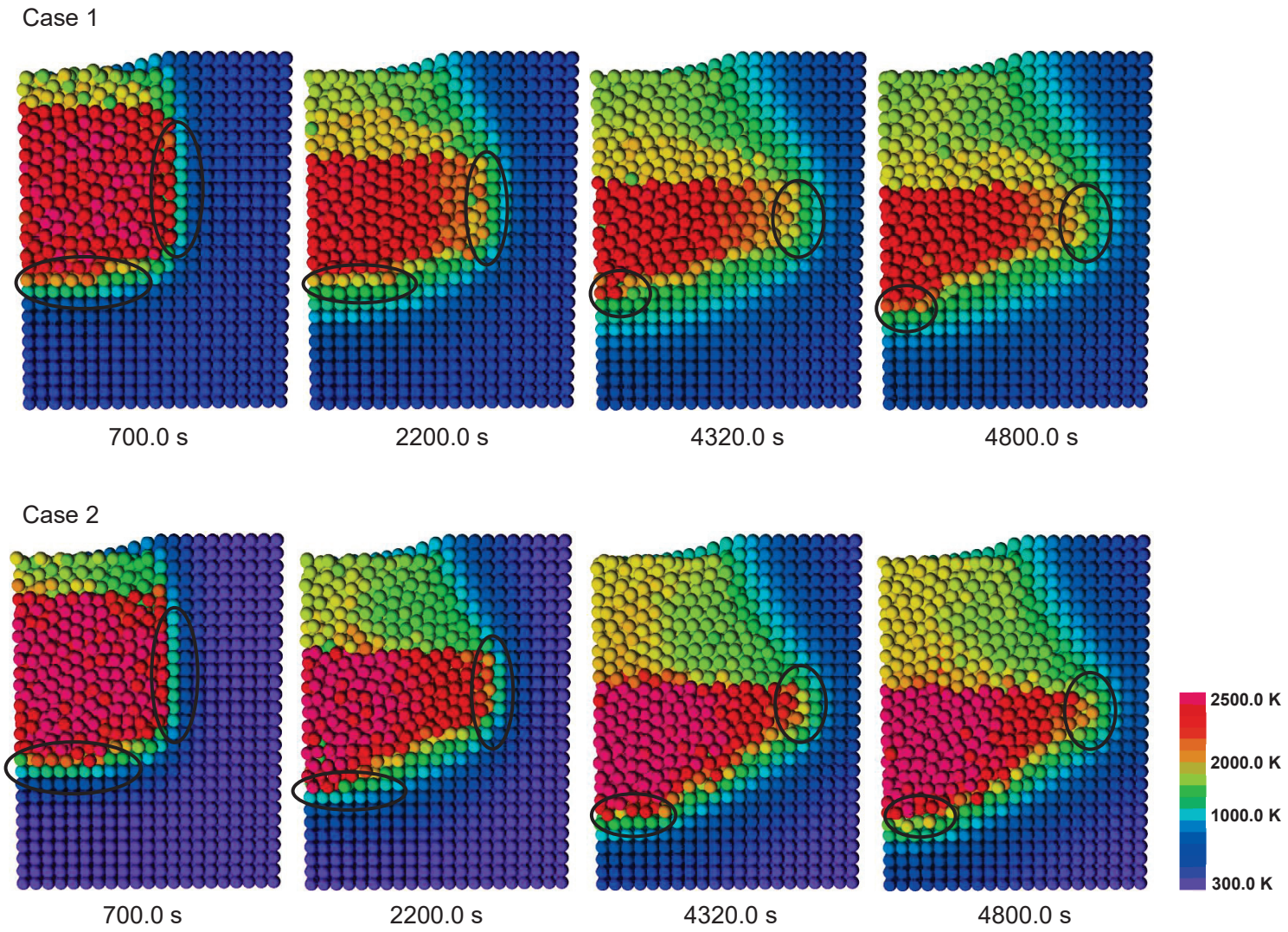

Fig. 5-5 Temperature distribution of representative moments in Case 1 and Case 2 (side view)

The ablation fronts in Case 1 and Case 2 for VULCANO-VB U7 simulation were shown in Fig. 5-6. As can be seen from the figure, the sidewall ablation fronts for Case 1 and Case 2 were rather similar, while the basemat ablation fronts progressed differently for both cases. The basemat ablation in Case 2 without aggregates progressed much faster than that in Case 1. As previously discussed, this is due to the thermally stable aggregates which influence the heat dissipation from the melt pool to bulk concrete and temperature distribution in the melt pool. Thermally stable aggregates which floated in the middle part of the melt pool can consume more energy from the

corium, thus leading to less energy dissipating to the basemat and sidewall. On the other hand, the aggregates distributed on the basemat part can facilitate more stable crust formation. Under the influence of aggregates on these two aspects, the basemat ablation fronts in Case 2 advanced more quickly than that in Case 1. The sidewall ablation rates in Case 1 and 2 both tended to decrease after 2200.0 s when basemat crust stared to remelt causing basemat ablation rate to increase. The remelting of basemat crust made it easier for corium to come into contact with concrete on the basemat, thus slightly promoting basemat ablation afterwards. In Fig. 5-6, a comparison with the ablation fronts calculated by Sevón who proposed a simple correlation in his paper (Sevon, 2008) was presented. The correlation was deduced from a heat transfer study of CCI 1-3 tests. The linear correlations were found to be related between the overall heat transfer coefficient h (W/m^2 K) and the superficial gas velocity j_g (m/s), which were as follows:

For basemat calculation:

$$h = 2987 \cdot j_g + 55 \tag{5-1}$$

For siliceous sidewall calculation

$$h = 5541 \cdot j_g + 15 \tag{5-2}$$

The prediction by the correlation slightly overestimated the basemat ablation while underestimated the sidewall ablation. This indicated that to simply consider superficial gas velocity on the basemat and sidewall surfaces might not be reasonable and complete enough to account for all the influential factors in MCCI simulation.

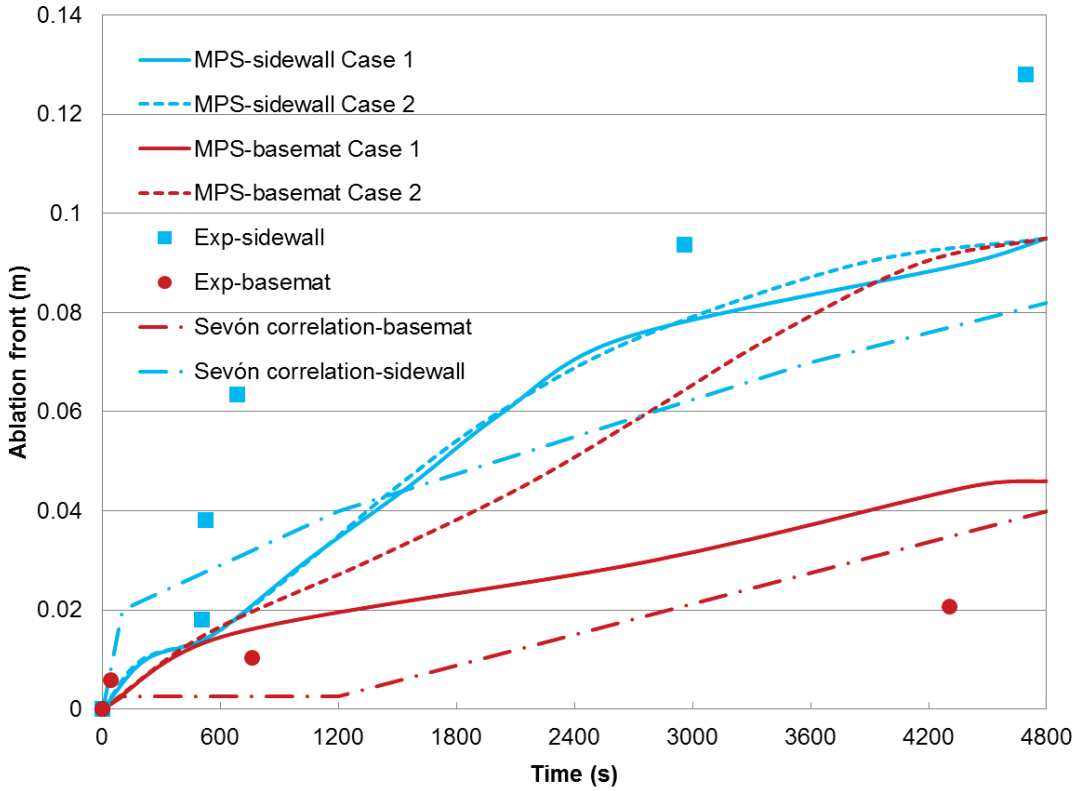

Fig. 5-6 Ablation fronts in Case 1 and Case 2 for VULCANO-VB U7 simulation

The finally cavity shapes in Case 1 and Case 2 were compared with the final cavity shape from experimental measurement. Both cases slightly underestimated sidewall ablation. Case 1 slightly overestimated basemat ablation, while Case 2 overestimated basemat ablation to a greater extent. Generally both Case 1 and Case 2 reproduced anisotropic ablation pattern as observed from the experiment and Case 1 agreed better with the cavity shape from the experimental measurement. The more significant sidewall ablation and less basemat ablation from the experimental cavity shape might suggest that more stable basemat crust was expected during MCCI in the experiment. Moreover, the continuous release of thermally silica aggregates from sidewall can accelerate the sidewall ablation by causing more intense convection near sidewall, whereas the pile-up of aggregates beneath the bottom basemat crust can further increase the thermal resistance and thus slow down the basemat ablation (Cranga et al., 2013). Under these combined influences, the cavity shape tended to be anisotropic instead of

isotropic.

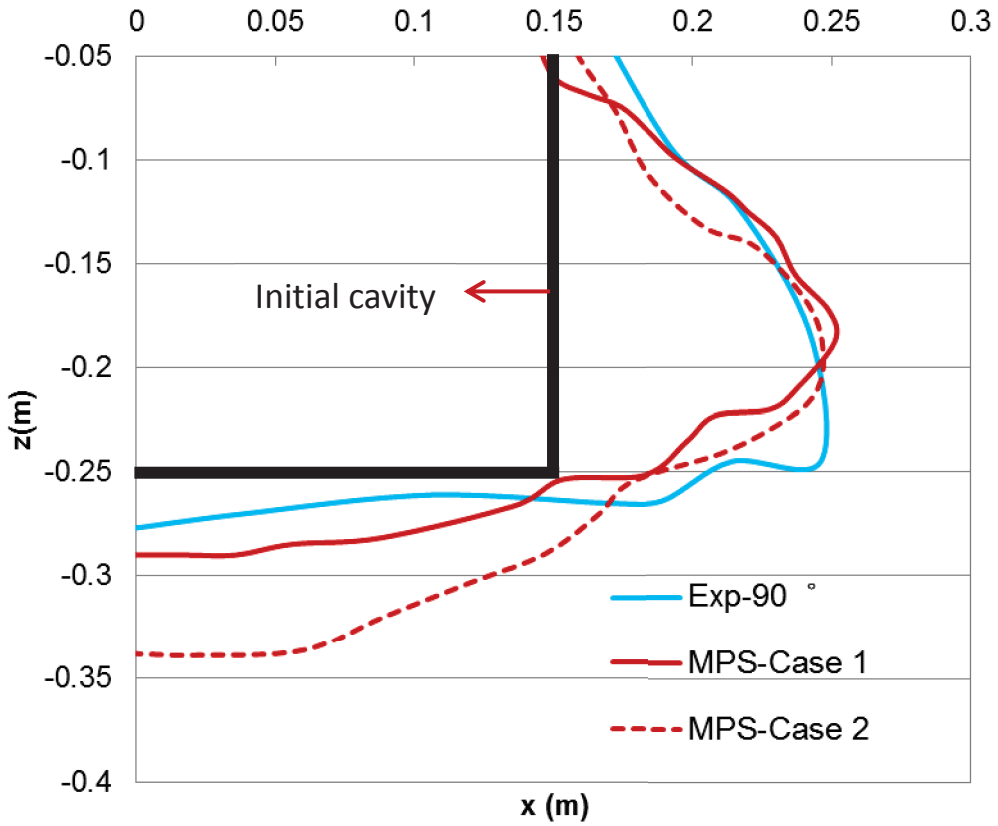

Fig. 5-7 Final cavity shapes in Case 1 and Case 2 for VULCANO-VB U7 simulation

5.2 3-D Simulations of MCCI experiment with stratified pool configuration: COMET-L3

5.2.1 Test descriptions of COMET-L3

COMET experiment series was carried out by KIT to investigate MCCI and the role of cooling processes (Doubleva et al., 2006). The research focus of COMET-L3 experiment was to investigate MCCI with a stratified melt pool configuration, which might occur in the late phase of MCCI after the metal corium is layered beneath the oxide corium due to the density decrease of oxide corium by concrete mixing.

COMET-L3 experiment investigates 2-D concrete erosion in a cylindrical crucible fabricated from siliceous concrete. The metal and oxide melt were generated with thermite reaction in a separate reaction vessel located above the test facility (Alsmeyer et al., 2006). The main composition of the siliceous concrete, metal melt and oxide melt

used in COMET-L3 experiment is listed in Tables 5-6 and 5-7. The Decay heat is simulated by sustained induction heating of the metal phase that is overlaid by the oxide melt. The concrete crucible was 1.0 m high with an inner diameter of 60 cm. The melt was comprised of 425 kg steel and 211 kg oxide at 1665°C (Alsmeyer et al., 2006). The overall melt pool height is about 45 cm, with the metal pool height being 25 cm and the oxide pool height being 20 cm. The COMET-L3 test facility and main test section are shown in Figs. 5-8 and 5-9.

Table 5-6 Melt composition in COMET-L3 (Alsmeyer et al., 2006)

Melt pool	Metal (425 kg)		Oxide (211 kg)	
Composition	Fe	Ni	Al_2O_3	CaO
Weight percent (%)	90.0	10.0	56.0	44.0

Table 5-7 Main composition of siliceous concrete used in COMET-L3 (Alsmeyer et al., 2006)

Composition	SiO_2	$Ca(OH)_2$	Al_2O_3	$CaCO_3$	H_2O
Weight percent (%)	70.30	13.55	6.58	5.46	4.11

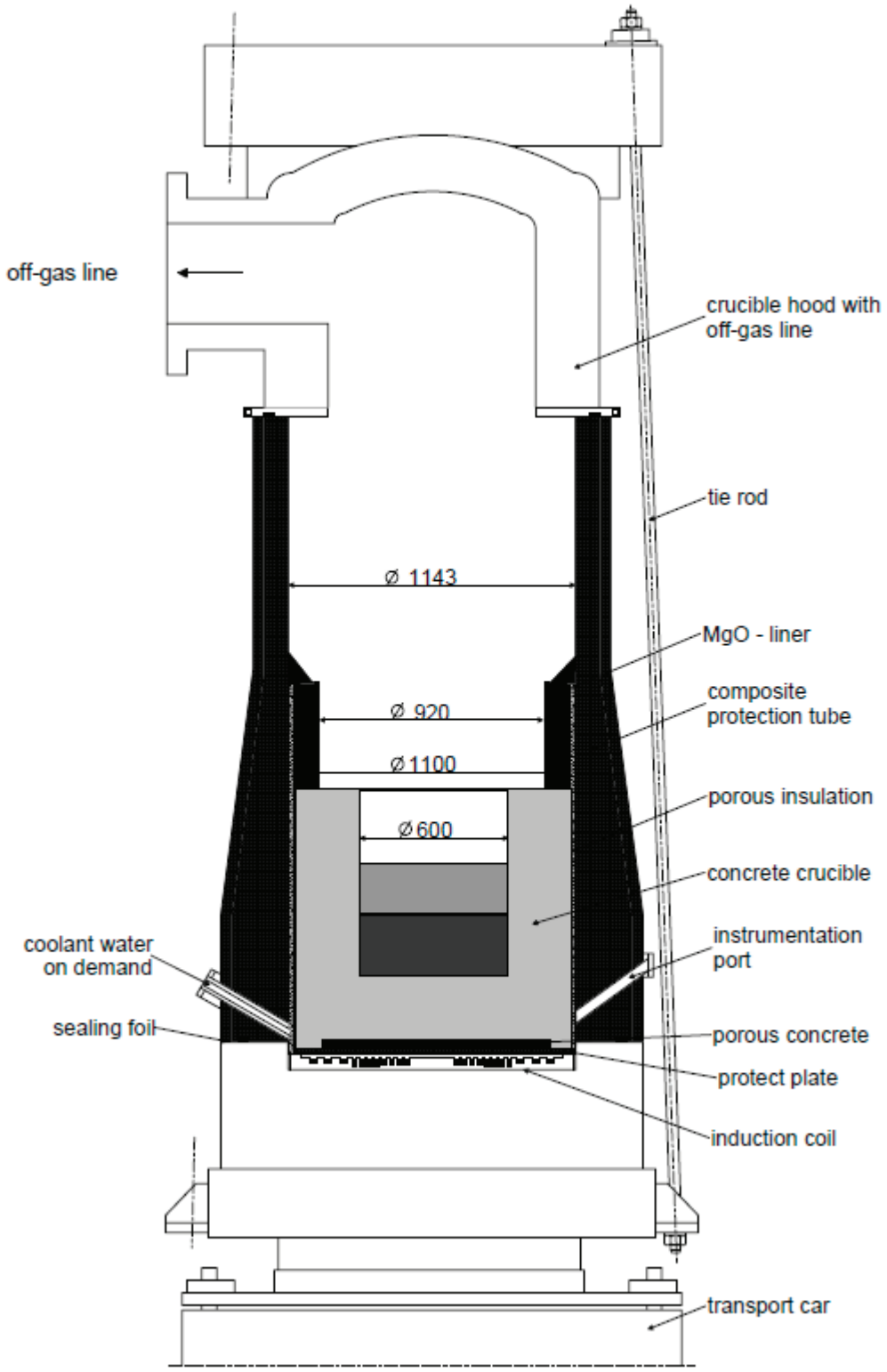

Fig. 5-8 COMET test facility with its main components (Alsmeyer et al., 2006)

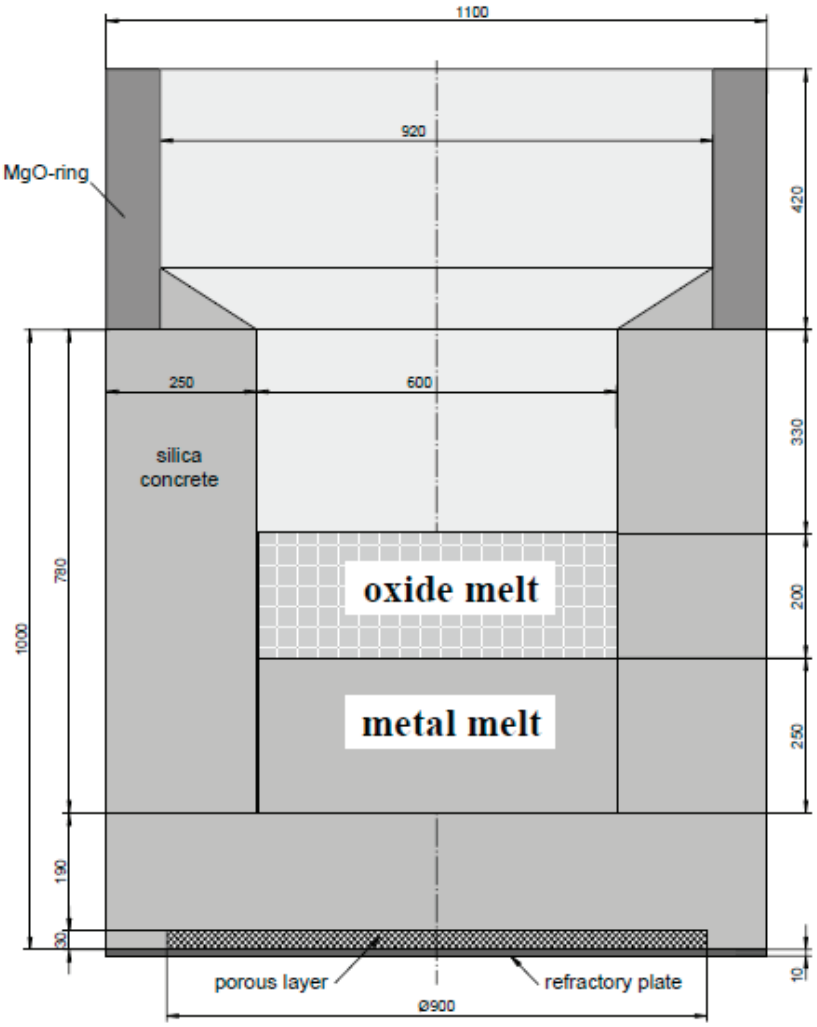

Fig. 5-9 Main test section of COMET-L3 test (Alsmeyer et al., 2006)

5.2.2 Simulation conditions of COMET-L3

COMET-L3 experiment was simulated with two slightly different initial particle configurations as shown in Fig. 5-10. As in previous simulations for VULCANO-VB U7 test, Configuration 1 was configured with no aggregates in the geometry, while Configuration 2 was configured with aggregates evenly distributed in the geometry. Both configurations were identical in size and represented only half of the real size of the test section used in COMET-L3 experiment in order to save computational cost. Six types of particles were used to represent different materials in the geometry. Besides the concrete, the aggregate and two types of wall particles as used in previous simulations,

there are two types of particles to represent the oxide melt and metal melt respectively. As in previous simulations, two types of wall particles were used. Still, the pressure was set to be zero and not calculated for dummy wall particles, while the pressure of wall particles was calculated in each time step. Meanwhile, nonslip boundary condition was applied on this layer of wall particles. Additionally, another two types of particles were set to represent the solidified melt (crust) and the molten concrete during phase change simulation, which are not shown in current geometry but will be shown in simulation results in later section.

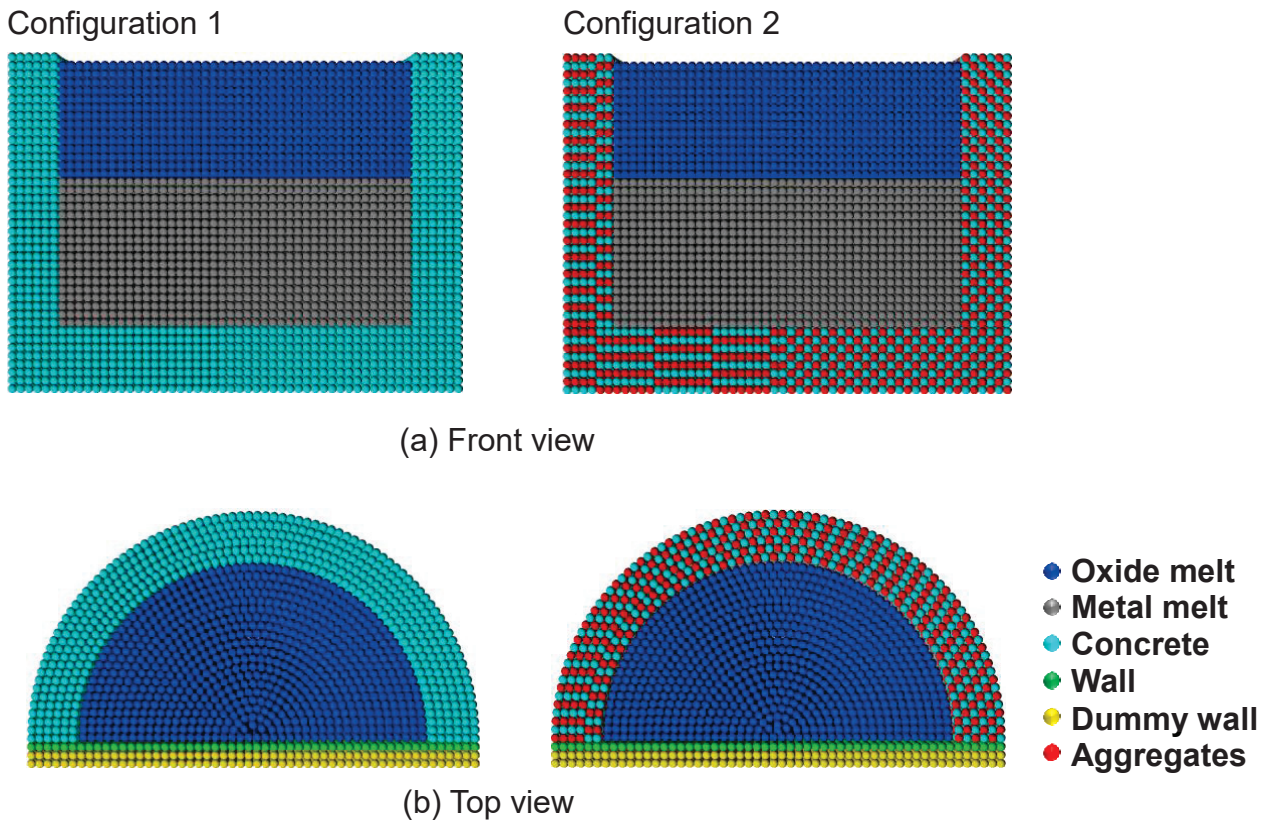

Fig. 5-10 Two particle configurations used for MPS simulation of COMET-L3

The physical properties of melt, siliceous concrete and silica aggregates that are used in COMET-L3 simulation are listed in Table 5-8 (Alsmeyer et al., 2006; Jerebtsov et al., 2001; Nishi et al., 2003). A brief summary of the initial conditions for COMET-L3

simulation are listed in Table 5-9 (Alsmeyer et al., 2006). The simulation time is 800.0 s when the dry cavity ablation ended in the test.

The models and assumptions that applied in two different cases for simulation of COMET-L3 are listed in Table 5-10. The two cases were designed the same as in VULCANO-VB U7 simulation. The main difference is the assumption about aggregates. Case 1 used Configuration 1 for aggregate assumption, and Case 2 used Configuration 2 to neglect the influence of aggregates. As in previous simulation of VULCANO-VB U7 experiment, slag film model and crust dissolution model were not applied to simulate siliceous concrete. This is because siliceous concrete generates much less gas (CO_2) when it decomposes and its diffusivity is much less than that of limestone concrete. One assumption that was different from that in VULCANO-VB U7 simulation was that stable sidewall crust formation was considered for both cases. Previous material strength measurements from MCCI experiments with oxidic corium indicated that the mechanical strength of oxidic corium crust ranges from 1 to 4 MPa (Lomperski et al., 2009), while the mechanical strength of steel generally ranges from 400 to 500 MPa. Thus, it is necessary to consider stable sidewall crust formation for metal melt.

Table 5-8 Physical property of the materials used for COMET-L3 simulation (Alsmeyer et al., 2006; Jerebtsov et al., 2001; Nishi et al., 2003)

Property	Metal melt (Fe+Ni)	Oxide melt (Al_2O_3+CaO)	Concrete (300 K)	Aggregate (silica, 300 K)
Density (kg/m^3)	6500.0	2810.0	2220.0	2650.0
Specific heat (J/kg·℃)	445.0	1190.0	1300.0	782.6
Heat conduction coefficient (W/m·K)	36.8	1.1	1.2	2.5
Solidus temperature (K)	-	1644.0	1403.0	
Liquidus temperature (K)	1723.0	1813.0	1523.0	
Latent fusion heat or decomposition heat (kJ/kg)	252.4	832.7	2075.0	

Table 5-9 Initial conditions for COMET-L3 simulation (Alsmeyer et al., 2006)

Parameters	COMET-L3
Particle size (Initial average distance between particles) (m)	0.015
Simulation time (s)	800.0
Total particle number	53739
Initial melt temperature (K)	1938.0
Initial concrete temperature (K)	300.0
Input power (kW)	200.0

Table 5-10 Main models and assumptions in cases for COMET-L3 simulation (Alsmeyer et al., 2006)

Models and assumptions	Case 1	Case 2
Aggregates	Yes	No
Sidewall crust formation	Yes	Yes
Crust dissolution model	No	No
Slag film model	No	No

5.2.3 Results and discussion

The representative moments of Case 1 and Case 2 to simulate COMET-L3 were shown in Fig.5-11. As can be seen, both cases showed isotropic ablation pattern in the final cavity. Concrete ablation mainly concentrated on the lower part of the melt pool and achieved by metal melt. This is due to the much higher thermal conductivity of metal, which is about thirty times of oxidic corium. This phenomenon is different from the anisotropic ablation pattern that has been observed in MCCI with oxidic corium and siliceous concrete. In fact, in other 2-D MCCI experiments in which metal melt and siliceous concrete were used, such as BETA (Alsmeyer, 1987) and MOCKA (Foit et al., 2012; Foit et al., 2014), isotropic ablation pattern or a different anisotropic ablation

pattern in which axial ablation is more pronounced than lateral ablation have been observed. This indicated that metal melt as corium in MCCI can have completely different characteristics regarding concrete ablation pattern.

As shown in Fig. 5-11, the time when basemat ablation and sidewall ablation occurred in Case 1 was delayed than that in Case 2. Moreover, the final cavity in Case 2 showed more basemat ablation and sidewall ablation compared to Case 1. This indicated that thermally stable aggregates could reduce overall concrete ablation by consuming more power from the melt pool. Additionally, a small amount of oxide crust was observed to form in the final cavity in Case 1, while no oxide crust formation was observed to form in the final cavity in Case 2. This again suggested that the power consumption capability of thermally stable aggregates. Since aggregates tended to relocate to the upper part of the melt pool and mix into the oxidic melt pool due to density-driven force, either floating aggregates or aggregates still embedded in the upper part of concrete cavity would mainly consume power from oxidic melt pool and contribute to lower temperature of oxidic melt pool in Case 1, thus leading to oxide crust formation in Case 1. The temperature distributions of final cavity in Case 1 and Case 2 were presented in Fig. 5-12. Obviously, Case 1 has a lower oxidic pool temperature compared to that in Case 2. This can be regarded as another piece of evidence to support the power consumption capability of thermally stable aggregates.

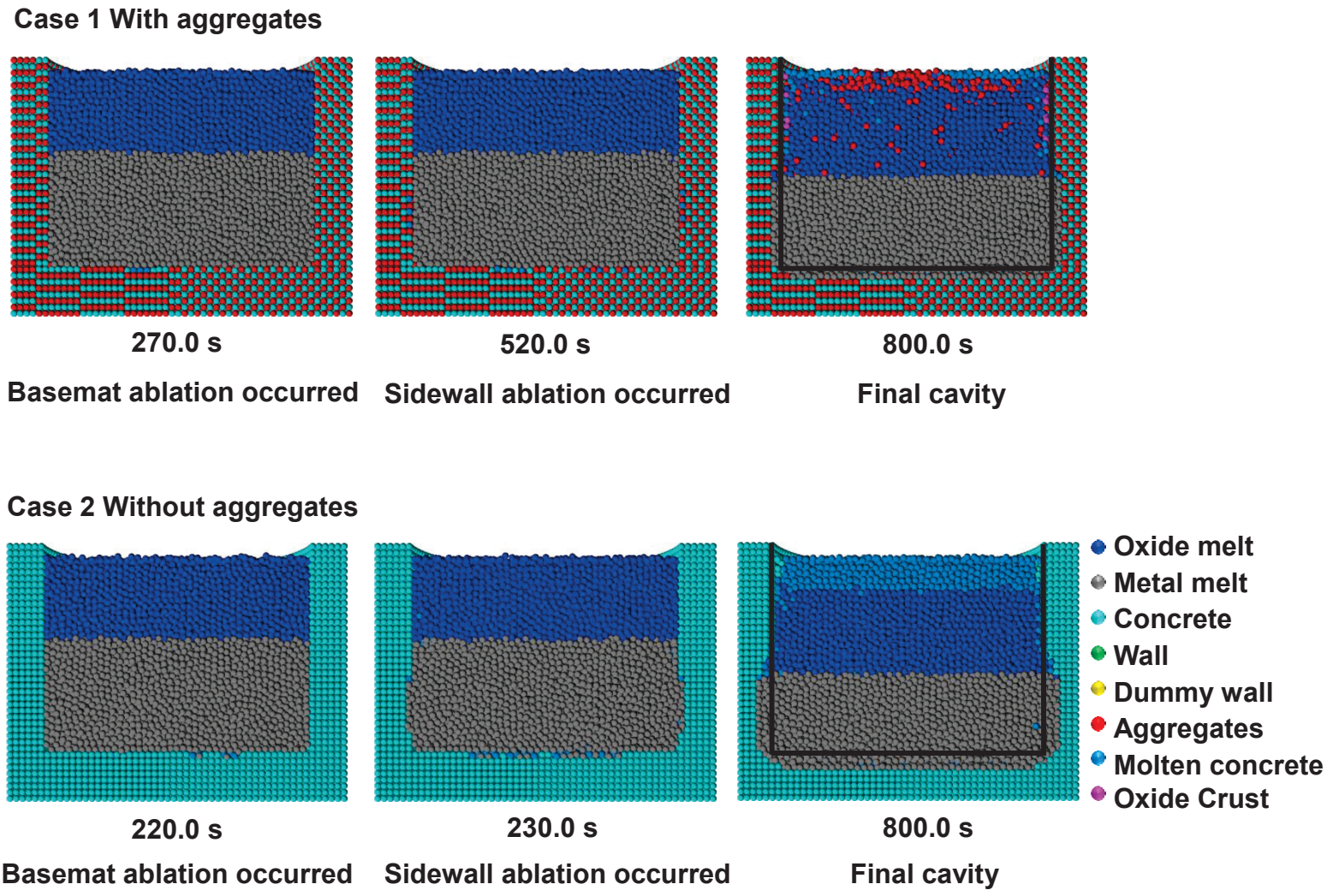

Fig. 5-11 Representative moments in Case 1 and Case 2 (Initial cavity shape was marked out by black solid lines in the last figure of Case 1 and Case 2)

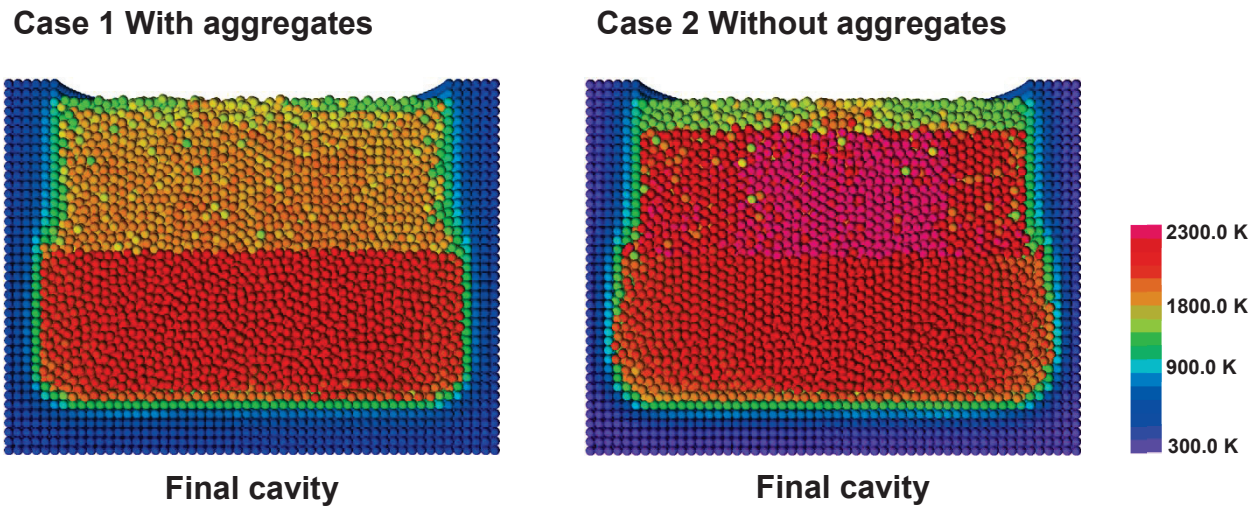

Fig. 5-12 Temperature of final cavity in Case 1 and Case 2

The ablation fronts in Case 1 and Case 2 for COMET-L3 simulation were shown in Fig. 5-13. The simulation results only showed dry cavity ablation before top flooding was initiated in the test. As can be seen from the figure, Case 1 and Case 2 both showed isotropic ablation pattern, namely, the final ablation depths of basemat and sidewall were similar. On the other hand, both sidewall and basemat ablation rates were quite similar in either case. On a whole, Case 1 showed a smaller basemat and sidewall ablation rate compared to those of Case 2. As previously discussed, this is due to the thermally stable aggregates which influence the power distribution and temperature distribution in the melt pool. For the average ablation rate, the experimental report gave an estimation of the average stationary erosion rate into axial direction until 800 s is 0.07 mm/s ±0.03 mm/s. The average axial (basemat) ablation rates predicted by Case 1 and Case 2 are 0.00375 mm/s and 0.05625 mm/s, which fell into the range of experimental measurements.

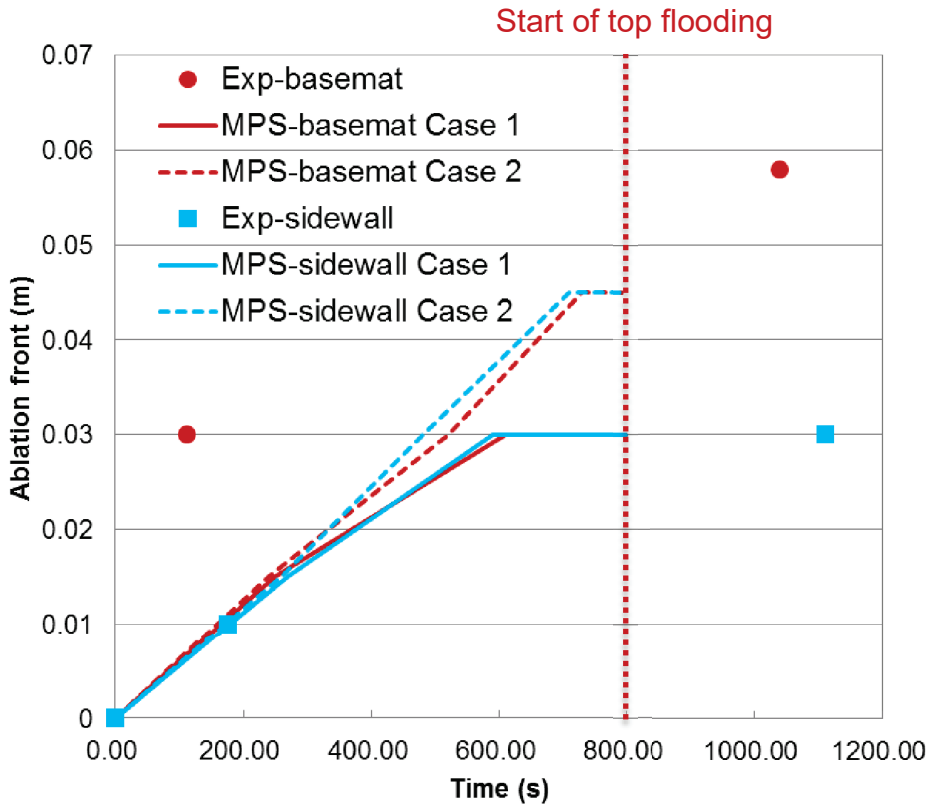

Fig. 5-13 Ablation fronts in Case 1 and Case 2 for COMET-L3 simulation

The final cavity shapes at 800.0 s in Case 1 and Case 2 for COMET-L3 simulation were compared with the final cavity shape at 800.0 s from experimental measurement. Both cases slightly underestimated sidewall ablation. Case 1 showed less sidewall and basemat ablation compared to Case 2. Both cases slightly overestimated sidewall ablation and underestimated basemat ablation to a greater extent. One thing that needs to be paid attention to from the experimental measurement is that the basemat ablation was not homogenous, with less ablation around r=0.0 m while significant ablation near r=±0.15 m. According to the experimental report (Alsmeyer et al., 2006), this inhomogeneous basemat ablation was caused by the inherent deficiency of induction heating. The magnetic field tends to be zero in the center of the induction coil, namely, the induction field is zero at the axis, which leads to the lower heating power near axis. Thus, if an "average" erosion process were to be taken consideration of, there should be a tendency that less basemat ablation was obtained while more sidewall ablation was

expected.

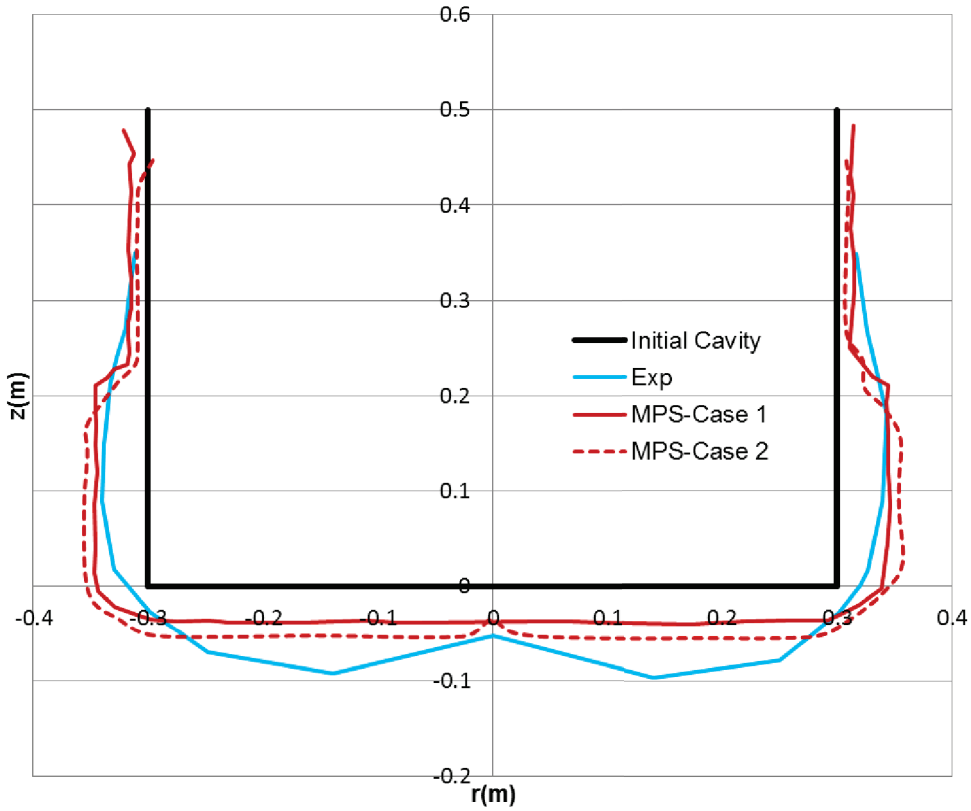

Fig. 5-14 Final cavity shapes at 800.0 s in Case 1 and Case 2 for COMET-L3 simulation

5.3 Conclusions

In this chapter, the improved MPS code was successfully applied to 3-D numerical simulation of VULCANO-VB U7 and COMET-L3 experiments. VULCANO-VB U7 was analyzed to investigate the ablation by prototypic oxidic corium and a special sacrificial concrete rich in Fe2O3 used for the EPR reactor pit. COMET-L3 experiment was analyzed to investigate the late-phase MCCI, in which certain time has elapsed after formation of the melt pool, using a stratified melt pool with metal beneath oxides. The following conclusions can be drawn from the present study:

1) Best estimation of VULCANO-VB U7 and COMET-L3 tests has been achieved by appropriate assumptions and models. The assumptions and models for best estimation of VULCANO-VB U7 and COMET-L3 tests are listed in Table 5-11. The assumptions and models for best estimation of siliceous concrete in 3-D MCCI simulation are consistent

with those best estimation assumptions and models in 2-D simulation. The only difference is the different consideration for sidewall crust formation when dealing with oxidic corium and metal corium. For metal corium, it is necessary to always consider stable sidewall crust formation, since metal crust (400-500 MPa) can have higher mechanical strength than oxidic corium crust (1– 4 MPa).

Table 5-11 Assumptions and models for best estimation of CCI-2 and CCI-3 tests

Models and assumptions	VULCANO-VB U7	COMET-L3
Aggregates	Yes	Yes
Sidewall crust formation	No	Yes
Crust dissolution model	No	No
Slag film model	No	No

2) From the simulations carried out by MPS method for 1-D, 2-D and 3-D MCCI experiments, the following isotropic/anisotropic ablation mechanisms have been shown:

- Isotropic ablation mechanism of limestone concrete: The sidewall and basemat crusts lead to isotropy in the boundary heat resistance. Formation of the slag-film at the crust-concrete boundary due to rich gas content of the concrete promotes the boundary heat transfer at the basemat while reduces it at the sidewall. The resultant anisotropy acts in the opposite direction to the anisotropy developed by the temperature stratification of the melt pool, caused by natural convection. As the result, the overall concrete ablation proceeds more or less isotropic
- Anisotropic ablation mechanism of siliceous concrete: Sidewall crust may not be formed due to continuous release of aggregates by concrete ablation. On the other hand, thermally stable aggregates near the corium-basemat boundary act as heat sink and stabilize the basemat crust, leading to substantial anisotropy in the boundary heat resistance, which is the main cause of the anisotropic ablation. The corium pool temperature stratification,

developed by natural convection also contributes to the anisotropy.

3) Crust on the corium-concrete interface plays an important part in axial concrete ablation process. In 3-D geometry, the evolution of crust can be more complicated than in 2-D geometry, which can add complexity to the boundary condition on the corium-concrete interface and influence the final concrete cavity profile.

4) Thermally stable aggregates have a slight influence on anisotropic ablation pattern in MCCI with oxidic corium and siliceous concrete. Aggregates can facilitate more stable basemat crust formation promoting anisotropic ablation pattern. Due to the higher thermal conductivity and density, aggregates can also count for more power consumption than concrete and contribute to lower melt pool temperature, leading to less concrete ablation.

Chapter 6 Conclusions and future work

6.1 Conclusions

In this thesis, an improved multi-dimensional MPS code with original models has been developed for MCCI analysis. The improved MPS code has been validated against and applied to 2-D and 3-D simulation of 1-D and 2-D MCCI experiments. Good agreement with experiments has been obtained through MPS simulation with proper assumptions and models. The capability of improved multi-dimensional MPS code with additional and originally developed models for MCCI analysis was further validated. Compared to previous MCCI study with MPS method, the accuracy of prediction of important parameters in MCCI has been improved. Especially, this approach has succeeded in attaining the following achievements:

- Agreement or disagreement with experiments has been successfully discussed with respect to identifications of influential factors rather than tuning with parameters through mechanistic MPS simulations in current study. The complex interactions of influential factors, namely crust formation, crust dissolution, slag film, and aggregates in MCCI have been understood through mechanistic modeling of fundamental physical phenomena in MCCI by MPS method.
- The mechanism that distinguishes isotropic ablation of limestone concrete and anisotropic ablation of siliceous concrete with oxidic corium has been revealed for the first time by limiting use of empirical models to some of the influential factors and modeling interactions of these influential factors mechanistically by MPS method.

Additionally, the following important conclusions can be drawn and summarized from current study:

1. The best estimation of 2-D and 3-D MPS simulation of 1-D and 2-D MCCI experiments suggests that:

1) From simulation of 1-D MCCI experiments, it can be concluded that best estimation can be achieved without applying complicated models. Only chemical reaction heat needs to be taken into consideration. Chemical reaction heat from metal oxidation or condense phase reaction can accelerate MCCI progression.

2) From 2-D and 3-D simulation of 2-D MCCI experiments with prototypic oxidic corium, best estimation can be achieved by applying different models and assumptions for limestone concrete and siliceous concrete as shown in Table 6-1. For limestone concrete, best estimation can be achieved by assuming no aggregates and considering sidewall crust formation, slag film (gas generation) and crust dissolution. For siliceous concrete, best estimation can be achieved by considering the effect of aggregates, assuming no sidewall crust formation, and neglecting slag film (gas generation) and crust dissolution.

Table 6-1 Models and assumptions for best estimation of limestone and siliceous concrete with prototypic oxidic corium

Models and assumptions	Limestone concrete	Siliceous concrete
Aggregates	No	Yes
Sidewall crust formation	Yes	No
Crust dissolution model	Yes	No
Slag film model	Yes	No

2) From 3-D simulation of 2-D MCCI experiment with a stratified pool configuration (metal beneath oxides) with siliceous concrete, best estimation is achieved in consistency with that for 2-D simulation of MCCI with siliceous concrete, namely considering aggregates and neglecting slag film (gas generation) and crust dissolution. The only difference is that it is necessary to

consider always consider stable sidewall crust formation, since metal crust can have higher mechanical strength than oxidic corium crust.

2. Crust formation can hinder MCCI progression since it can serve as thermal insulation between corium pool and concrete. The timing of crust formation and break can significant influence the progress of MCCI.

3. Anisotropic ablation of siliceous concrete by oxidic corium is mainly caused by more stable basemat crust in siliceous concrete due to less crust dissolution and the inherent anisotropic characteristic of natural convection in an internally heated pool. Thermally stable silica aggregates can slightly promote anisotropy by influencing power distribution in the melt pool and favoring more stable basemat crust formation. In general, the thermally stable aggregates near the corium-basemat boundary act as heat sink and stabilize the crust, leading to substantial anisotropy in the boundary heat resistance, which is the main cause of the anisotropic ablation. The corium pool temperature stratification, developed by the natural convection also contributes to the anisotropy.

4. Isotropic ablation of limestone concrete by oxidic corium is mainly caused by the equivalent basemat and sidewall crust boundary and the effect of gas generation by slag film. Limestone concrete may be modeled homogeneously, because carbonate aggregates melt and do not remain as solid in the corium melt pool once released from the concrete by ablation. Hence, crust can be formed and be equally stable at both the sidewall and basemat boundary, which leads to isotropy at the boundary heat resistance. The diffusivity and gas content of limestone concrete is high, thus crust dissolution and the boundary heat transfer changes due to formation of slag film needs to be considered. On the other hand, formation of the slag film promotes the boundary heat transfer at the basemat while reduces it at the sidewall. The resultant anisotropy acts in the opposite direction to the anisotropy developed by the temperature stratification of the melt pool, caused by natural convection. As the result, the overall concrete ablation proceeds more or less isotropic.

5. In MCCI with a metal melt pool, anisotropic ablation in which lateral ablation is higher than axial ablation tends not to occur when there is no stable crust formation. However, long time behavior of MCCI with a metal melt pool still needs to be further investigated.

6.2 Future work

Despite the study on MCCI presented in this thesis, there are still some improvements and issues which should be addressed in future work on MCCI.

1. The study in this thesis mainly investigates dry cavity ablation of MCCI. The influence and effectiveness of top water flooding needs to be further evaluated in the future simulation work of MCCI.

2. The influence of gas generation was only considered on the corium-concrete interface by slag film in current study. The influence of gas generation or bubbling on the entire corium pool should be investigated.

3. Due to the limitation of current computing power, it is difficult to perform MPS simulation of MCCI in a real plant-scale reactor cavity. Thus, further study should be focused on advanced techniques of parallel computing or appropriate scaling study to extrapolate current small-scale simulation results to large plant-scale MCCI.

Reference

Alsmeyer, H., 1987. BETA experiments in verification of the WECHSL code: experimental results on the Melt-Concrete Interaction", Nucl. Engrg. Des. 103, 115-125.

Alsmeyer, H., Cenerino, G., and Cordfunke, E.H. P., et al., 1995. Molten corium/concrete interaction and corium coolability - A state of the art report. EUR 16649 EN, Office for Official Publications of the European Communities, ISBN 92-827-5228-3, Brussels, Luxembourg.

Alsmeyer, H., Cron, T., Fluhrer, B., et al., 2007. The COMET-L3 experiment on long-term melt–concrete interaction and cooling by surface flooding, Forschungszentrum Karlsruhe in der Helmholtz-Gemeinschaft, FZKA 7244.

Amano, Y., 2015. The Fukushima Daiichi accident – report by the Director General. ISBN 978-92-0-107015-9 (set).Vienna: International Atomic Energy Agency.

Bažant, Z.P. and Kaplan, M.F. 1996. Concrete at High Temperatures: Material Properties and Mathematical Models. Essex: Longman Group. pp. 412 . ISBN 0-582-08626-4.

Blose, R.E., Gronager, J. E., Suo-Anttila A. J. et al., 1987. SWISS: Sustained Heated Metallic Melt/Concrete Interaction with Overlying Water Pools, NUREG/CR-4727, SAND85-1546.

Bradley, D. R., 1988. Modeling of Heat Transfer Between Core Debris and Concrete, ANS Proc. 1988 National Heat Transfer Conf., Houston, Texas USA, July 24-28.

Carenini L., Haquet, J.F., Journeau, C., 2007. Crust formation and dissolution during corium concrete interaction. Proceedings of ICAPP 2007, Nice, France, May 13-18.

Chai, P.H., Kondo, M., Erkan, N., Okamoto, K., 2015. Numerical simulation of 2D ablation profile in CCI-2 experiment bymoving particle semi-implicit method. Nucl. Eng. Des. 301, 15–23.

Chase, M.W. 1998. NIST-JANAF Thermochemical Tables. 4th edition. Journal of Physical and Chemical Reference Data, Monograph No. 9, Parts I and II, pp.1952 . ISBN 1-56396-831-2.

Chen, R.H., Tian, W.X., Su, G.H. et al., 2011. Numerical investigation on bubble condensation and coalescence of bubble pairs using moving particle semi-implicit

method. Chem. Eng. Sci. 66(21), 5055-5063.

Chen, R.H., Tian, W.X., Su, G.H. et al., 2010. Numerical investigation on bubble dynamics during flow boiling using moving particle semi-implicit method. Nucl. Sci. Eng., 240(11), 3830–3840.

Chen, R.H., Oka, Y., 2014a. Numerical analysis of freezing controlled penetration behavior of the molten core debris in an instrument tube with MPS. Ann. Nucl. Energy 71, 322–332.

Chen, R.H., Oka, Y., 2014b. Numerical investigation on melt freezing behavior in a tube by MPS method. Nucl. Eng. Des. 273, 440–448.

Copus, E.R., et.al., 1989. Core-Concrete Interactions Using Molten Steel with Zirconium on a Basaltic Basemat: The SURC-4 Experiment, NUREG/CR-4994, Sandia National Laboratories, Albuquerque, NM.

Copus, E.R., Blose, R.E., Brockmann, J.E. et al., 1992. Core-Concrete Interactions Using Molten UO2 with Zirconium on a Basaltic Basemat, The SURC-2 Experiment. Sandia Nat. Lab. Report NUREG/CR-5564, SAND90-1022.

Cranga, M., Mun, C., Michel, B. et al., 2007. Status of the interpretation of real material 2D MCCI experiments with the ASTEC/MEDICIS code. MCCI-OECD seminar, Cadarache, St-Paul lez Durance, France, October 10-11, 2007.

Cranga, M., Ferry, L., Haquet, J.F. et al., 2010a. MCCI in an oxide/metal pool: lessons learnt from VULCANO, Greene, ABI and BALISE experiments and remaining uncertainties, ERMSAR-10, May 11-12, Bologna, Italy.

Cranga, M., Spindler, B., Dufour, E., et al., 2010b. Simulation of corium concrete interaction in 2D geometry. Prog. in Nucl. Energy 52, 76-83.

Cranga, M., Spencer, C., Atkhen, K., et al., 2013. Towards an European consensus on possible causes of MCCI ablation anisotropy in an oxidic pool. 6th European Review meeting on Severe Accident Research (ERMSAR-2013), October 2-4, Avignon, France.

Day, M.A., 1990. The no-slip condition of fluid dynamics. Erkenntnis 33(3), 285-296.

Dinh, T.N., Konovalikhin, M.J., and Sehgal, B.R., 2000. Core melt spreading on a reactor containment floor. Prog. in Nucl. Energy 36 (4), 405-468.

Doremus, R.H., 2002. Viscosity of silica. J. Appl. Phys. 92 (12), 7619-7629.

Dyer, H., and Trombetta, M.J., 2013. International Handbook of Energy Security. UK: Edward Elgar Publishing. pp. 576.
Epstein, M. 1998. Thermal hydraulics of molten core concrete interactions: a review and comparison of heat transfer models with data, interpretation of rheological data, and a theory for the onset of concrete spallation. Palo Alto: Electric Power Research Institute. (ACEX-TR-21.)

Eriksson, G. and Pelton, A.D., 1993. Critical Evaluation and Optimization of the Thermodynamic Properties and Phase Diagrams of the CaO- Al_2O_3, Al_2O_3-SiO_2, and CaO- Al_2O_3-SiO_2 Systems. Metall. Trans. B 24B, 807-816.

Farmer, M. T., Spencer, B. W., Kilsdonk, D. J., and R. W. Aeschlimann, 2000. Results of MACE corium coolability experiments M0 and M1b. Proceedings 8th Int. Conf. on Nucl. Eng., Baltimore, MD USA, April 2-6.

Farmer, M.T., 2001. Modeling of ex-vessel corium coolability with the CORQUENCH code. In: Proc. of 9 th Int. Conf. on Nucl. Eng. April 8-12, Nice, France.

Farmer, M.T., Lomperski, S., Kilsdonk, D.J., et al., 2006. OECD MCCI Project 2-D Core Concrete Interaction (CCI) Tests: Final Report. OECD/MCCI-2005-TR05, Argonne National Laboratory, Argonne, USA.

Farmer, M.T., 2011. The CORQUENCH Code for Modeling of Ex-Vessel Corium Coolability under Top Flooding Conditions Code Manual – Version3.03. OECD/MCCI-2010-TR03, Argonne National Laboratory, Argonne, USA.

Ferry, L., Breton, M., Monerris, J., et al., 2010. Corium-concrete interactions in an oxide pool in the VULCANO facility: VB-U7 test – FeSiCo (EPR) concrete. DEN Technical Document, DEN/DTN/STRI/LMA/NT/2010/002/0, CEA Cadarache, France.

Foit, J.J., Reimann, B., Adroguer, G. et al., 1995. The WECHSL-Mod3 Code: A Computer Program for the Interaction of a Core Melt with Concrete Including the Long Term Behavior—Model Description and User's Manual, FZKA 5522.

Foit, J.J., Cron, T., Fluhrer, B., et al., 2012. MOCKA experiments on concrete erosion by a metal and oxide melt. 5th European Review Meeting on Severe Accident Research (ERMSAR-2012) Cologne (Germany), March 21-23.

Foit, J.J., Fischer, M., Journeau, C., Langrock, G., 2014. Experiments on MCCI with oxide and steel. Ann. Nucl. Energy 74, 100–109.

Gauntt, R.O., Cash, J.E., Cole, R.K. et al., 2005. MELCOR Computer Code Manuals. Sandia National Laboratories. NUREG/CR 6119, SAND2005-5713.

Gauntt, R., Kalinich, D., Cardoni, J., et al., 2012. Fukushima Daiichi accident study (status as of April 2012). Sandia National Laboratories. SAND2012-6173.

Gronager, J. E., Suo-Anttila, A. J., Bradley, D. R., and Brockmmn, J. E., 1986. TURCl: Large Scal Metallic Melt-Concrete Interaction Experiments and Analysis, NUREG/CR-4420 (SAND85-0707), Sandia National Laboratories, USA.

Gronager, J. E., Suo-Anttila, A. J., and Brockmmn, J. E., 1986. TURC2 and 3: Large Scale UO2/ZrO2/Zr Melt-Concrete Interaction Experiments and Analysis, NUREGKR-4521 (SAND8603 18), Sandia National Laboratories, USA.

Haste, T., 2015. Severe accident phenomena part 2: Ex-vessel. IAEA Workshop on Severe Accident Management Guidelines 19–23 October, Vienna, Austria.

Hirschberg, S., Spiekerman, G., and Dones, R., 1998. Severe Accidents in the Energy Sector, 1st ed., PSI Report No. 98-16, ISSN 1019-0643, Paul Scherrer Institute, Villigen, Switzerland.
IEAE (International Atomic Energy Agency), 1996. Defence in depth in nuclear safety INSAG-10/a report by the International Nuclear Safety Advisory Group. ISBN 92-0-103295-1.Vienna: International Atomic Energy Agency, 1996.

IEAE (International Atomic Energy Agency), 1997. Nuclear power and sustainable development.
https://www.iaea.org/OurWork/ST/NE/Pess/assets/06-13891_NP&SDbrochure.pdf

Jerebtsov, D.A., and Mikhailov, G.G., 2001. Phase diagram of CaO-Al2O3 system. Ceram. Int. 27, 25-28.

Journeau, C., Haquet, J.F., Spindler, B., et al., 2006. The VULCANO VE-U7 corium spreading benchmark, Prog. in Nucl. Energy, 48(3), 215-234.

Journeau, C., and Haquet, J.F., 2009. Convection heat transfer anisotropy in a bubbling viscous pool—application to molten core–concrete interaction. Nucl. Eng. Des. 239, 389–394.

Journeau, C., and Piluso, P., 2012a. Core Concrete Interaction. In: Konings R.J.M., (ed.) Comprehensive Nuclear Materials, volume 2, pp. 635-654 Amsterdam: Elsevier.

Journeau, C., Piluso, P., Correggio, P., et al., 2012b. Contributions of the VULCANO

experimental programme to the understanding of MCCI phenomena. Nucl. Eng. Technol. 44(3), 261-272.

Kerr, R.C., 1995. Melting and dissolving driven by vigorous compositional convection. 12th Australian Fluid Mechanics Conference. The University of Sydney, Australia.

Koshizuka, S., Oka, Y., 1996. Moving-particle semi-implicit method for fragmentation of incompressible fluid. Nucl. Sci. Eng.123, 421-434.

Koshizuka, S. and Shibata, K. "MPS-SW-MAIN-Ver2.0" Copyright registration P8827-1, February 23, 2006 (in Japanese).

Koshizuka, S., Sekine, M., Oka, Y., and Obata, H., 1999. Numerical Analysis of Molten Core-Concrete Interaction Using MPS Method. Proc. of Workshop on Severe Accident Research, Japan (SARJ-99), JAERI-Conf 2000-015, Tokyo, Japan, Nov. 8-10.

Kutateladze, S. S. and Malenkov, I. G., 1978. Boiling and bubbling heat transfer under the conditions of free and forced convection. 6th Int. Heat Transfer Conf., Toronto, Canada, August 7-11.

Kulacki, F.A., Emara, A.A., 1975. High Rayleigh number convection in enclosed fluid layers with internal heat sources. US Nucl. Regulatory Comm. Report NUREG-75/065.

Li, G., Oka, Y., Furuya, M., Kondo, M., 2013a. Experiments and MPS analysis of stratification behavior of two immiscible fluids. Nucl. Eng. Des. 265, 210-221.

Li, X., Tian W.X., Chen R.H. et al., 2013b. Numerical simulation on single Taylor bubble rising in LBE using moving particle method. Nucl. Eng. Des. 265, 227-234.

Li, X., Oka Y., 2014. Numerical simulation of the SURC-2 and SURC-4 MCCI experiments by MPS method. Ann. Nucl. Energy 73, 46–52.

Lee, S.D., Lee, J.K., Suh, K.Y., 2007. Natural convection thermo fluid dynamics in a volumetrically heated rectangular pool. Nucl. Eng. Des. 237, 473–483.

Lomperski, S. and Farmer, M. T., 2009. Corium Crust Strength Measurements, Nucl. Eng. Design, 238, 2551-2561.

Mehta, P.K., and Monteiro P.J.M., 2006. *Concrete: microstructure, properties, and materials.* USA: The McGraw-Hill Companies, Inc. 659pp.

Maruyama, Y., Kojima, Y., Tahara, M., et al., 2006. A study on concrete degradation

during molten core/concrete interactions. Nucl. Eng. Des., 236, 2237-2244.

Matsuura, T., Oka, Y., 2013. MPS simulation of spreading behavior of molten materials. In: Proc. of III International Conference on Particle-based Methods-Fundamentals and Applications Particles 2013.

Naus, D. J., 2005. The Effect of Elevated Temperature on Concrete Materials and Structures - A Literature Review. Oak Ridge Laboratoy, NUREG-XXXX ORNL/TM-2005/553.

Nie, M., Fischer, M., and Lohnert, G., 2002. Advanced MCCI modeling based on stringent coupling of thermal hydraulics and real solution thermochemistry in COSACO. In: Proceedings of 10th Int. Conf. on Nucl. Eng., April 11-12, Arlington, Virginia, USA.

Nishi, T., Shibata, H., Ohta, H. et al., 2003. Thermal conductivities of molten iron, cobalt, and nickel by laser flash method. Metall. Mater. Trans. A. 34A, 2801-2807.

Penttilä, K., 2012. Molten corium and concrete thermodynamics and viscosity. Research report. VTT-R-01441-12, VTT, Finland.
http://www.vtt.fi/inf/julkaisut/muut/2012/VTT-R-01441-12.pdf

Rohde, J., and Cenerino, G., 1992. Ex-vessel melt behavior and its role in safety assessment of LWR. In: Proceedings of Second OECD (NEA) CSNI Specialist Meeting on Molten Core Debris-Concrete Interactions, Karlsruhe, Germany, 1-3 April.

Sehgal, B.R., 2011. Nuclear Safety in Light Water Reactors. UK: Academic Press. pp.391.

Sevón, T., 2005. Molten Core Concrete Interactions in nuclear accidents - theory and design of an experimental facility. VTT Tiedotteita . Research Notes 2311.

Sevón, T., 2008. A heat transfer analysis of the CCI experiments 1-3. Nucl. Eng. Des. 238, 2377-2386.

Sevón, T., Journeau, C., and Ferry, L., 2013. VULCANO VB-U7 experiment on interaction between oxidic corium and hematite-containing concrete. Ann. Nucl. Energy 59, 224-229.

Spencer, B.R. et al., 1992. Results of MACE Tests M0 and M1, Second OECD-CSNI Specialist Meeting on Molten Core Debris-Concrete Interactions. In: Proceedings of Second OECD (NEA) CSNI Specialist Meeting on Molten Core Debris-Concrete Interactions, April 1-3, Karlsruhe, Germany.

Spindler, B., Atkhen, K., Cranga, M., et al., 2007. Simulation of molten corium concrete interaction in a stratified configuration: the COMET-L3-L3 Benchmark, European Review Meeting on Severe Accident Research (ERMSAR07), Paper S2-5, Karlsruhe.

Strizhov, V., Kanukova, V., Vinogradova, T. et al., 1996. An Assessment of the CORCON-MOD3 Code Part I: Thermal-Hydraulic Calculations, NUREG/IA-0129, Office of Nuclear Regulatory Research U.S. Nuclear Regulatory Commission Washington, DC 20555-0001.

Suzuki, H., et al., 1993. Fundamental Experiment and Analysis for Melt Spreading on Concrete Floor, Proceedings of 2nd ASME/JSME Nuclear Engineering Conference, 1, 403-407.

TEPCO, 2013. 福島第一原子力発電所 1～3 号機の炉心・格納容器の状態の推定と未解明問題に関する検討第 1 回進捗報告. http://www.tepco.co.jp/cc/press/betu14_j/images/140806j0102.pdf

TEPCO, 2015. 福島第一原子力発電所 1～3 号機の炉心・格納容器の状態の推定と未解明問題に関する検討第 3 回進捗報告. http://www.tepco.co.jp/cc/press/betu15_j/images/150520j0102.pdf

Thompson, D.H. et al., 1992. Thermal Hydraulic Aspects of the Large-scale Integral MCCI Test in
the ACE Program, Second OECD (NEA) CSNI Specialist Meeting on Molten Core Debris-Concrete Interactions, April 1-3, Karlsruhe, Germany.

Tian, W.X., Ishiwatari, Y., Ikejiri, S., et al., 2010. Numerical computation of thermally controlled steam bubble condensation using Moving Particle Semi-implicit (MPS) method. Ann. Nucl. Energy 37, 5-15.

Nomenclature

C_p	specific heat, J/(kg·K)
C_{slag}	coefficient in slag film model
d	dimension number
F	external force, N
g	gravity acceleration, m/s^2
h_b	heat transfer coefficient in slag film model
H	enthalpy, *J/ kg*
H_{s0}	enthalpy when melting begins
H_{s1}	enthalpy when melting completely ends
H	enthalpy, *J/ m3*
k	thermal conductivity, W/(m·℃)
L_λ	Laplacian constant, which is defined as $L_\lambda = \sqrt{\frac{\sigma_m}{g(\rho_m - \rho_g)}}$
m	mass, kg
n	particle number density
P	pressure, Pa
Q	heat source, W/m^3
r	particle location vector
r	particle distance, m
T	temperature, K
t	time, s
u	particle velocity vector
w	weight function

Greek letters

φ	scalar variable
λ	coefficient
ρ	density, kg/m^3
μ	viscosity, Pa·s

Superscript/subscript

b	bottom
dc	decomposition
e	effective
g	gas
i,j	particle number
l	liquidus
m	melt
n, n-1	designation of time step
0	initial condition
s	solidus
tr	transition
*	temporal

研究業績書
List of research achievements

類 別(By Type)	題名、 発表・発行掲載誌名、 発表・発行年月、 連名者(申請者含む)(theme, journal name, date & year of publication, name of authors inc. yourself)
(1)Paper	
o	1. **X. Li** and Y. Oka. Numerical simulation of the SURC-2 and SURC-4 MCCI experiments by MPS method, Ann. Nucl. Energy 73, 46–52 (2014).
o	2. **X. Li** and A. Yamaji. A Numerical Study of Isotropic and Anisotropic Ablation in MCCI by MPS Method. Prog. Nucl. Energy 90, 46–57 (2016).
(2)Presentations	
	1. **X. Li**, Y. Oka, R.H. Chen, T. Matsuura, and T. Watanabe. Mechanistic study of melt behavior by MPS method-spreading, melt penetration and MCCI, Int. Workshop on Nuclear Safety and Severe Accident (NUSSA-2014), Sept. 3-5, Chiba, Japan (2014).
	2. **X. Li** and Y. Oka. Mechanistic study of melt behavior by Moving Particle Semi-implicit (MPS) method, 2014 Fall Meeting of the Atomic Energy Society of Japan Sept. 8-10, Kyoto, Japan (2014).
	3. **X. Li**, A. Yamaji, R.H. Chen, T. Matsuura, and T. Watanabe. Mechanistic study of melt behavior in nuclear severe accident by MPS method,「粒子法コードユーザーグループ」第 30 回会合, 平成 26 年 11 月 26 日, 海上技術安全研究所, 三鷹市, 東京 (2014).
o	4. **X. Li** and Y. Oka. Numerical simulation of MCCI experiments by MPS method – Validation against SURC-2 and 4 experiments, 10th International Topical Meeting on Nuclear Thermal Hydraulics, Operation and Safety (Nuthos-10) Dec. 14-18th, Okinawa, Japan (2014).
o	5. **X. Li** and A. Yamaji. Numerical simulation of anisotropic ablation of siliceous concrete – analysis of CCI-3 MCCI experiment by MPS method, 16th International Topical Meeting on Nuclear Reactor Thermalhydraulics (NURETH-16), August 30-September 4, Hyatt Regency Chicago, USA (2015).